

Dissertation

submitted to the Combined Faculties
for the Natural Sciences and for Mathematics
of the Ruperto–Carola University of Heidelberg, Germany

for the degree of Doctor of Natural Sciences

Put forward by
Diplom–Physiker Peter C. Seitz
Born in Heidenheim an der Brenz
Oral examination: 9. 12. 2009

The Physical Role of Lipopolymers in the Modulation of Interfacial Forces and Dissipative Pattern Formation in Biomembrane Models

Peter C. Seitz

Referees:
Prof. Dr. Annemarie Pucci
Prof. Dr. Motomu Tanaka

Zusammenfassung

Es wurde eine neue Klasse von Zellmembranmodellen eingeführt, die von einer festen Unterlage durch lineare polymer Abstandshalter mit definierter Länge getrennt sind. Das Ziel war die physikalische Rolle von weichen Polymeren die an eine Membranoberfläche gebunden sind (z.B. Glycocalix) bei der Regulierung von Zell-Zell Wechselwirkungen zu enträtseln. Mit spekulärer Neutronen- und Röntgenstreuung sowie Ellipsometrie wurde der Einfluss der lateralen Dichte und der Länge der Polymerketten auf die Wechselwirkungen zwischen Membran und Unterlage systematisch untersucht. Die Kombination unterschiedlicher Reflektivitätstechniken unter verschiedenen osmotischen Drücken und unter Wasser ermöglichte die Berechnung quantitativer Kraft-Abstands Beziehungen. Diese machen das Zusammenspiel der wichtigsten Oberflächenkräfte deutlich, wodurch der Gleichgewichtsabstand bestimmt ist. Bei dem Übertrag der Lipid-Lipopolymer Monolagen von der Wasser-Luft Grenzfläche auf feste Unterlagen durch vertikales Ziehen entstehen Streifenmuster parallel zur Übertragsrichtung. Durch zwei speziell dafür konstruierte experimentelle Aufbauten, welche die Beobachtung der Phasentrennung *in situ* ermöglichen, konnte ein tieferer Einblick in den Prozess der Strukturbildung gewonnen werden. Die quantitative Abhängigkeit der charakteristischen Länge von den Präparationsbedingungen wurde systematisch im Rahmen der Theorie der Phasentrennung diskutiert: Tatsächlich konnten die experimentellen Ergebnisse bei kleinen Übertragungsgeschwindigkeiten gut mit der Cahn-Hilliard Gleichung erklärt werden.



Abstract

A new class of model cell membranes which is separated from the solid substrate via linear polymer spacers of defined length was established in order to unravel the physical role of soft polymers attached to the membrane surface (e.g. glycocalyx) in modulating cell-cell interactions. Using specular neutron and X-ray reflectometry as well as ellipsometry the influence of the lateral density and length of the polymer chains on the membrane-substrate interactions was systematically investigated. The combination of different reflectivity techniques at various osmotic pressures and in bulk water enabled the calculation of quantitative force-distance relationships which reveal the interplay of the major interfacial forces determining the equilibrium distance. During the transfer of lipid-lipopolymer monolayers from the air-water interface to solid substrates by vertical lifting, stripe patterns parallel to the transfer direction appear. A deeper insight into the pattern formation process is taken by two uniquely designed experimental setups that allow for the *in situ* observation of phase separation during film transfer. The dependence of the characteristic length on the preparation parameters was systematically discussed in the theoretical framework of phase separation: In fact, the experimental results at low transfer speeds could be well explained with the Cahn-Hilliard equation.

This work owes its existence to many helpful and supportive people:

First and foremost my thank goes to Prof. M. Tanaka who paved the way scientifically and financially which allowed me to conduct this work.

I am grateful that Prof. A. Pucci acted repeatedly as my official supervisor.

This study could not have been conducted without the chemical expertise of Prof. R. Jordan and M. Reif who supplied the many lipopolymers used.

My thank goes to the masters of the mechanical workshops, R. Lehrhuber and K. Schmitt. It was their craftsmanship that realized the experiments conceived.

I want to thank Prof. T. Salditt for the use of experimental equipment and scientific knowledge of his laboratory and to K. Giewekemeyer for support during the measurements in Göttingen.

I am indebted to Prof. K. Yoshikawa for his hospitality and the many scientific discussions he catalyzed as well as Prof. H. Wada for his great interest and discourses on this work.

The everyday lab life—scientifically and otherwise—was immensely enriched by T. Schubert, E. Schneck, T. Kaindl, M. Tutus, H. Rieger, W. Abuillan and S. Kaufmann. Finally, I would like to thank my family.

*Von der Wirklichkeit können wir wissenschaftlich
gar nichts aussagen, ausser, dass sie in einem Raum
enthalten ist, und dass Bewegung in ihr stattfindet.*

∞ Paul Du Bois-Reymond ∞

CONTENTS

Introduction	1
1 Experimental Techniques & Material	7
1.1 Material	7
1.1.1 Lipopolymers	8
1.1.2 Solid Substrates	8
1.2 Preparative Techniques	9
1.2.1 Langmuir–Blodgett Transfer	9
1.2.2 Langmuir–Schaefer Transfer	10
1.2.3 Vesicle Fusion	11
1.3 Reflection Based Techniques	11
1.3.1 X–Ray Reflectivity	15
1.3.2 Ellipsometry	17
1.4 Fluorescence Microscopy	20
2 Transversal Structure of Lipopolymer Layers	23
2.1 Monolayers at the Liquid–Gas Interface	24
2.2 Monolayers at the Solid–Gas Interface	26
2.2.1 Ellipsometry	26
2.2.2 X–Ray Reflectivity	31
2.3 Bilayers at the Solid–Liquid Interface	34
2.3.1 X–Ray Reflectivity	34
2.3.2 Ellipsometry	38
2.4 Discussion	42
2.4.1 Interfacial Forces	43
2.4.2 Polymer Volume	47
2.5 <i>In Situ</i> Control Using Switchable Polymers	48
2.6 Conclusion	52

3	Lateral Structure of Lipopolymer Layers	53
3.1	Quantitative Dependence on Preparation Parameters	54
3.1.1	Transfer Speed	56
3.1.2	Subphase Viscosity	56
3.1.3	Dipping Angle	58
3.2	Observation of the Three-Phase Contact Line	59
3.2.1	Langmuir Trough Combined with Ellipsometer	59
3.2.2	Langmuir Trough Combined with Fluorescence Microscope	64
3.3	Theoretical Modeling of Stripe Pattern Formation	67
3.3.1	General Considerations	67
3.3.2	Relationships Between Experiment and Theory	68
3.3.3	Comparison to Experiments	71
3.4	Discussion	79
3.5	Conclusion	82
4	Outlook	83
A	Ell Software	89
	What Ell Can Be Used For, 92 ♦ Installation, 92 ♦ Loading Data, 92 ♦ Layer Models, 94 ♦ Fitting Data, 94 ♦ Simulation, 94 ♦ Calculating Chi Square Maps, 95 ♦ Ellipsometric Period, 95.	
B	Neutron Reflectivity at the Gas-Solid Interface	97
C	Cahn-Hilliard Equation	101
	Derivation, 101 ♦ Linear Stability Analysis, 103.	
	References	107

INTRODUCTION

What is life?—This still open question has troubled generations of researchers by trying to grasp and answer it using physical concepts¹. On the way to an answer, a detailed understanding of the mechanisms taking place on the molecular level has been obtained by intensive study over several decades. Cells, the fundamental units of life consist of four major families of molecules apart from the overall abundant water^{2,3}. These four families are carbohydrates, amino acids, nucleotides and lipids. The first three are sets of monomers that combine to macromolecules which, assembled to structures, exhibit a great diversity. Carbohydrates (oligo- and polysaccharides) are used for energy storage (dextran), structural stability (chitin, cellulose) and for specific recognition between cells. Amino acids are the building blocks for peptides and proteins which in turn provide versatile functionality (enzymes, ion channels, cell adhesion receptors, molecular motors). DNA (Deoxyribonucleic acid) and RNA (Ribonucleic acid) are composed of a linear sequence of nucleotides and mainly responsible for information storage.

Unlike the other three families, lipids self-assemble into structures by physical (non-covalent) interactions which is in contrast to the chemical (covalent) bonds in the macromolecules. Lipids consist of two parts, a hydrophobic alkyl chain and a hydrophilic head group of various phosphate derivatives. The amphiphilic character of lipid molecules leads to the formation of self-assembled structures, in order to minimize the contact between hydrophobic (non-polar) chains and polar solvents (water). This entropic effect, called hydrophobic effect⁴, and the lipid molecular structure (cylindrical, conical) determines the arrangement of the resulting aggregates, like spherical micelles, planar bilayers, inverted micelles, etc. Bilayer membranes are the common border of cells and organelles to separate their interior from the exterior.

To gain deeper insight into the physical principles that determine structure and function of cell membranes in a quantitative manner, the design of well-defined biomembrane models with a reduced number of molecular components is very helpful. One such model is established and characterized in this thesis, in order to unravel how soft, hydrophilic oligomers and polymers adjacent to the lipid head groups modulate the interfacial forces acting at biological interfaces, such as the glycocalyx coating the

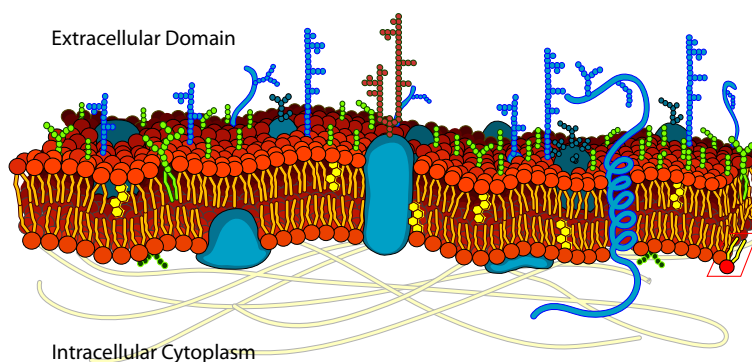


Figure 1 – A simplified diagram of a cell plasma membrane (modified from ⁵ according to ⁶). The lipid bilayer is densely packed with proteins. On the intracellular side the lipid bilayer is attached via protein assemblies to the cytoskeleton. The extracellular side exhibits different sugar residues which form the glycocalyx.

cell surface (see Figure 1).

Artificial biomembrane models have to fulfill some or all of the basic requirements of lipid membranes in cells, as suggested by the fluid mosaic model⁷ and the later refinements^{8,9}. There, fluidity refers to the lateral mobility of the membrane constituents and the mosaicity describes the arrangement of a lipid bilayer densely packed with proteins and attached carbohydrates. In addition, heterogeneity of the membrane seems important for specific biological interactions such as lipid rafts¹⁰.

Among the model membranes are free-standing black lipid membranes¹¹, spherical lipid vesicles¹² and Langmuir monolayers at the air-water interface¹³. Vesicles have been widely used to study the phase behavior of lipid mixtures and to determine the borders of fluidity and heterogeneity induced by demixing. Black lipid membranes are ideally suited for monitoring the selective and non-selective transport of charged species (e.g. ions) across the membrane¹⁴. But these model systems lack mechanical stability. This stability is found in solid-supported membranes either on planar supports^{15,16} or on spherical beads¹⁷⁻¹⁹. For the structural analysis the planar geometry is advantageous and has been used successfully for decades to study many of the key biological processes (e.g. cell adhesion)²⁰. A diagram is shown in the left panel in Figure 2 on the next page. The deposition on a solid support, though, introduces a problem not encountered in free-standing membranes: the close contact to the substrate. The distance between solid support and lipid bilayer is on the order of several Ångstrom²¹. Such a small gap is sufficient as a lubricating layer for a simple model membrane comprised only of lipids or molecules coupled to the distal membrane surface²². However,

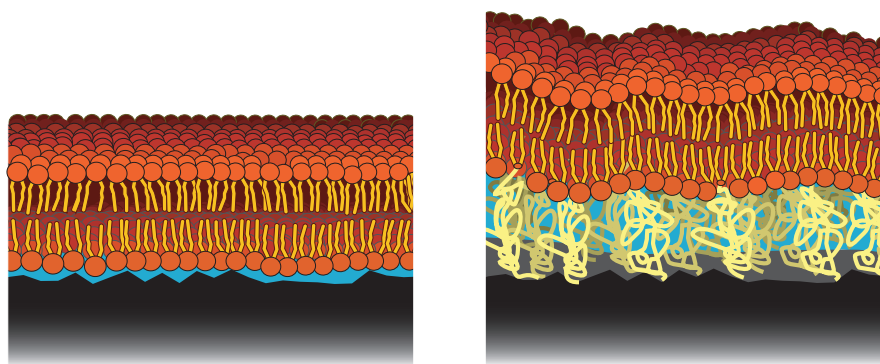


Figure 2 – Diagram of supported membranes. **Left:** solid-supported membrane, only a thin lubricating layer between the solid substrate and the membrane is present. **Right:** polymer-tethered membrane, the spacing can be adjusted by varying polymer length and lateral density resulting in a more fluid membrane capable of incorporating transmembrane proteins with large protrusions.

the addition of integral transmembrane proteins with protrusions from the membrane, with the protrusions reaching up to 10 nm, lead to a contact with the substrate. The strong interaction with the solid substrate can easily lead to denaturation of the protein and loss of functionality^{23,24}. Additionally, the mobility of the proteins, one of the fundamental requirements in nature, is hampered²⁵.

As a remedy, a spacing between the solid support and the bilayer which provides a non-denaturing environment for proteins needs to be introduced by a soft and hydrophilic interlayer²⁶. This can be realized by the addition of either polymeric *cushions* deposited underneath the membrane or *tethers* keeping the membrane at a certain distance from the solid support.

Cushions are deposited separately from the membrane. This requires that the polymer forms a stable film on the solid support and that the membrane wets the polymer. As reported by Wong *et al.*²⁷ in the case of polyethyleneimine the required change in properties to support formation of a membrane can be achieved by a simple preparational step of letting the polymer film dry before depositing the membrane, but in general demands a well considered choice of polymer. Cushions underneath membranes have been prepared from various hydrated polymer films: polyethyleneimine²⁷, dextran²⁸, polyacrylamide²⁹, agarose³⁰ and cellulose^{25,26,31–33}. Especially cellulose has proven to be a very useful material for polymer cushions supporting artificial and native membranes^{33–35}. The observation of homogeneously distributed, highly mobile, transmembrane proteins integrin $\alpha_{\text{IIb}}\beta_3$ retaining their natural function on a cellulose cushion can be taken as a proof of sufficient spacing. The deposition of cellulose using

Langmuir–Blodgett transfers gives good control over the thickness of the cellulose film by the number of successive transfers. However, a systematic variation of the density and lubricating properties is impossible since the density and viscosity of the polymer cushions cannot be adjusted flexibly.

A more tunable soft interlayer can be introduced by tethering the membrane to the solid support via linear polymer chains coupled to the lipid alkyl chains, as displayed in the right panel of Figure 2 on the preceding page. The membrane model established in this thesis can offer a unique advantage over polymer cushioned membranes to control the density of the polymer interlayer via the density of the polymer tethers. For the preparation of a well ordered structure of a membrane on top of a polymer layer, the polymer tether needs to be hydrophilic to undergo a clear phase separation from the hydrophobic alkyl chains. As tethers, lipids with a polymeric head group are used. The hydrophobic part of these lipopolymers anchors the molecule in the membrane and the polymer acts as a spacer between the solid support and the membrane. Additionally a surface coupling group on the polymer provides firm attachment to the support. Tethers that have previously been used by other groups consist of oligopeptides³⁶, oligo(ethylene oxide)^{37–39} and poly(ethylene oxide)^{40,41}, glycoacrylates⁴² as well as poly(alkyl oxazolines)^{43–46}. The separations attainable with oligomers are short compared to the protrusions of transmembrane proteins and are therefore not the material of choice for supported membranes with incorporated proteins. Poly(ethylene oxide) based lipopolymers with a silane surface coupling group have successfully been used for the preparation of mixed monolayers of lipids and lipopolymers on the air–water interface and were transferred by a Langmuir–Blodgett transfer to a solid support with completion to a bilayer by vesicle fusion⁴¹. The Langmuir–Blodgett transfer allows a fine control over the composition of the monolayer and the two step process of completing the bilayer the preparation of asymmetric membrane leaflets. The application of these membranes was shown by the incorporation of protein cytochrome b_5 and the binding of annexin A5⁴¹ as well as VAMP binding reversibly to incorporated syntaxin 1A/SNAP-25⁴⁰. However, the use of poly(ethylene oxide) is problematic since the adsorption of poly(ethylene oxide) chains at the air–water interface can lead to defects in the membrane⁴¹. The same holds true for poly(2-ethyl-2-oxazolines) used by Naumann *et al.*⁴⁴ which forms aggregates in water⁴⁷. Naumann *et al.*⁴⁴ used even a coupling to the surface at a random position on the polymer resulting in an undefined spacing under various conditions. A combination of hydrophilic polymers with precisely controlled length and surface coupling groups based on poly(2-methyl-2-oxazoline) was first presented by Purrucker *et al.*⁴⁶. Although its applicability was shown by incorporating integrin $\alpha_{IIb}\beta_3$ receptors, a quantitative measurement of the membrane–support distance and the physical role of polymer spacers in the modulation of interfacial interactions still remain as an open question.

This foremost question of thickness and composition of the spacing layer has been rather neglected. Atomic force microscopy has been used to scrape an area free of mem-

brane and measure the height difference⁴² but giving no information about the composition. The separation has also been tried to be measured by fluorescence interference contrast microscopy, but this technique strongly depends upon the location and orientation of the transitional dipole moments of the fluorescent probes in the membrane⁴⁸. Alternative ways to evaluate structures of supported membranes are techniques based on reflectivity, such as ellipsometry^{49–51}, specular X-ray^{21,52–55} and neutron reflectometry^{27,39,56}. With these techniques not only the thickness is measured but also the refractive index, the volume fraction of water in the interlayer and the roughness of the layers can be obtained.

In this thesis, a thorough investigation on the separation of a membrane from a solid support by lipopolymer tethers and the composition of this interlayer is presented. To this end poly(2-methyl-2-oxazoline) lipopolymers were used⁵⁷. The lipopolymers were synthesized by the group of Prof. R. Jordan at the TU Munich (now Professur für Makromolekulare Chemie, TU Dresden). Their synthesis via living cationic ring-opening polymerization results in a precisely controlled length and allows a flexible end functionalization^{45,58–60}. The methyl side group was chosen as it renders the polymer hydrophilic and thus separates well from the alkyl chains. The polymer-tethered membranes were prepared by Langmuir-Blodgett transfer of lipid-lipopolymer mixtures from the air-water interface. Completion to a bilayer proceeded either by vesicle fusion or Langmuir-Schaefer transfer.

After an introduction to the experimental techniques in Chapter 1, in Chapter 2 the focus is on the transversal structure of the polymer-tethered membranes (normal to the membrane plane). In this part, the influence of the degree of polymerization ($n = 14 \dots 104$), surface coupling group (covalent: silane, adsorption: piperidine) and composition of lipid-lipopolymer mixtures on the membrane-substrate distance and the resulting net forces acting at the interface were investigated systematically. The characterization starts with the intermediate stages in preparation of a monolayer at the liquid-gas interface and at the solid-gas interface. Combined with the measurements of the polymer-tethered membrane at the solid-liquid interface a more complete picture of the structure and interfacial interactions is obtained. Experiments using neutron reflectometry are presented in Appendix B supporting the findings of X-ray and ellipsometry measurements.

Chapter 3 deals with a very unique phenomenon observed during Langmuir-Blodgett transfer of the lipid-lipopolymer mixtures as depicted in Figure 3 on the next page. Parallel stripe patterns exhibiting long-range ordering emerge, reminiscent of many phase separating phenomena in multi-cellular organisms like the stripes of zebras⁶¹ or, in condensed matter, like domains in ferromagnetic garnet films⁶². Indeed the stripes were previously found to consist of one phase enriched in lipid and the other enriched in lipopolymer⁶³. To gain a deeper insight into the pattern forming process, two unique experimental setups were constructed for this thesis by the combination of observational techniques with a Langmuir trough. The first setup uses imaging ellipsometry

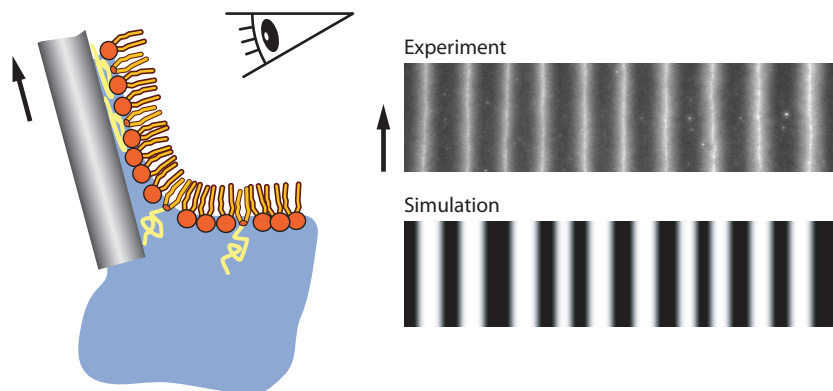


Figure 3 – Langmuir–Blodgett transfer of a lipid–lipopolymer mixture (**left**) results in a stripe pattern due to demixing of lipids and lipopolymer along the transfer direction (**right**). Shown below is the result of a 1D simulation of the Cahn–Hilliard equation.

which is a very powerful tool to reconstruct the local height profiles of the wetting films on the substrate with a vertical resolution of several Ångstrom and a lateral resolution in the μm range. It is demonstrated that this custom–made instrument can measure extremely small contact angles well below one degree near the three–phase contact line. Complementary to the height information, the lateral reorganization process is revealed by the combination of a fluorescence microscope with a Langmuir trough. The experimental findings were systematically compared with a theoretical framework of phase separation based on the Cahn–Hilliard equation. This phenomenological approach is employed to establish a theoretical explanation of the observed stripe patterns in dependence on the preparation conditions.

CHAPTER 1

EXPERIMENTAL TECHNIQUES & MATERIAL

In this chapter the utilized material and experimental techniques are presented along with procedures used for data analysis.

1.1 MATERIAL

The most abundant substance used for the experiments in this thesis is purified water. Purified water is drawn from a water purification system either produced by Millipore (Schwalbach/Ts., Germany) or by TKA (TKA GenPure, Niederelbert, Germany). The specific electrical resistance upon drawing exceeded $18\text{ M}\Omega\text{ cm}$. Lipids other than lipopolymers were ordered through Avanti Polar Lipids (Alabaster, AL, USA). 1-stearoyl-2-oleoyl-*sn*-glycero-3-phosphocholine (SOPC) and 1,2-diphytanoyl-*sn*-glycero-3-phosphate (DPhPC) are in the L_α liquid crystalline phase⁶⁴ at all conditions prevalent in the experiments. The transition temperature of SOPC is 7°C ⁶⁵ while the methyl side groups of DPhPC decrease its transition temperature to below -120°C ⁶⁶. For the preparation of working solutions the lipid concentration of all mixtures was diluted to 1 mg ml^{-1} . Fluorescence markers Texas Red[®] 1,2-dihexadecanoyl-*sn*-glycero-3-phosphoethanolamine (Texas Red[®]-DHPE) and N-(6-tetramethylrhodaminethiocarbonyl)-1,2-dihexadecanoyl-*sn*-glycero-3-phosphoethanolamine (TRITC-DHPE) were purchased from Invitrogen (Karlsruhe, Germany). The excitation (ex) and emission (em) maxima are for Texas Red[®]-DHPE ex: 595 nm, em: 615 nm and for TRITC-DHPE ex: 555 nm, em: 580 nm. All other chemicals were purchased in bulk quantities and were of analyt-

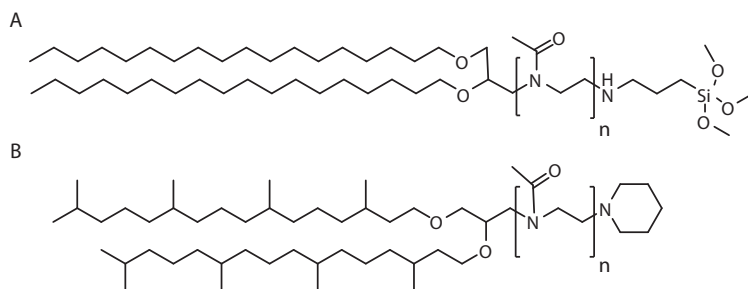


Figure 1.1 – Chemical structures of the lipopolymers used with monomer number n . **A)** Distearyl-poly(2-methyl-2-oxazoline)-trimethoxysilane, $n = 14, 33, 104$. **B)** Diphytanyl-poly(2-methyl-2-oxazoline)-piperidine, $n = 60$.

ical grade.

1.1.1 Lipopolymers

Lipopolymers were synthesized at the WACKER–Chair of Macromolecular Chemistry at the Technical University Munich, Germany. Details about the synthesis can be found elsewhere^{45,46,59}. PMOX₁₄, PMOX₃₃ and PMOX₁₀₄ with a trimethylsiloxane surface coupling group were synthesized by Anton Förtig while all other lipopolymers used in this study were prepared and characterized by Michael Reif, both under supervision of Rainer Jordan. The synthesis is done using the living cationic ring–opening polymerization⁶⁷. Starting with a lipid moiety as initiator the monomers are formed by breaking the ring structure of 2-substituted 2-oxazoline. This method results in a very low polydispersity index close to 1 and allows termination by a functional group. For the current study distearyl ($2 \times C_{18:0}$) and diphytanyl ($2 \times 4ME C_{16:0}$) were used as lipid anchors. As monomer 2-methyl-2-oxazoline was incorporated into the lipopolymers unless denoted otherwise. As a termination on the other side either trimethoxysilane or a piperidine group were attached. While trimethoxysilane binds covalently to the silicon dioxide surface of the solid substrate, piperidine offers only a nonspecific adsorption onto the substrate but has the advantage of a longer shelf life since no polycondensation of the lipopolymers can occur. The chemical structures are shown in Figure 1.1.

1.1.2 Solid Substrates

As solid substrates, glass cover slips and polished silicon wafers were used. Glass cover slips made from borosilicate glass were obtained from Marienfeld (Lauda–Königshof-

en, Germany) with a thickness of 0.16 mm–0.19 mm, suitable for fluorescence microscopy. Silicon wafers were supplied by Si-Mat (Landsberg am Lech, Germany) with a native oxide layer of $\approx 15 \text{ \AA}$ thickness. The wafers were broken into rectangular pieces of 24 mm \times 20 mm. Before use, solid substrates were cleaned to remove any contaminants still present from the production and to create a homogeneously hydrophilic surface. A modified protocol based on the RCA Standard Clean 1 bath has been adopted⁶⁸. The cleaning procedure consists of successive ultrasonication for five minutes in acetone, ethanol, methanol and purified water, followed by half an hour in a (1:1:5 v/v) mixture of (30 % ammonia : 30 % hydrogen peroxide : purified water) at 60 °C. Intensive rinsing with purified water and storage in vacuum completes the cleaning procedure. The substrates were used within several days after being cleaned.

1.2 PREPARATIVE TECHNIQUES

1.2.1 Langmuir–Blodgett Transfer

As the first step in sample preparation the solid substrate was coated by an amphiphilic monolayer by a Langmuir–Blodgett (LB) transfer^{69,70}. With the LB transfer technique the composition of the monolayer can be controlled with high precision. By adjusting the surface pressure of the monolayer in the Langmuir trough the density can be set, which is retained in the transferred monolayer. The Langmuir trough consists of a Teflon (polytetrafluoroethylene) basin with a movable barrier also made out of Teflon as shown schematically in Figure 1.2 on the next page. When filled with an aqueous medium, amphiphilic molecules can be spread on the fluid. Due to their amphiphilic nature the molecules orient themselves to face their hydrophobic part away from the aqueous subphase. The hydrophobicity of Teflon prevents the adsorption of the spread molecules onto the walls of the basin. Dependent on the amount of spread molecules per trough area, the surface tension of the subphase γ_0 is decreased to γ . This decrease is denoted as surface pressure $\Pi = \gamma_0 - \gamma$. The surface pressure is measured by the immersed Wilhelmy plate. The force acting on this completely wetted plate are gravity and the surface tension trying to minimize the surface area. With an increase of the surface pressure, the surface tension of the subphase is reduced and with it the force pulling the Wilhelmy plate downward. The surface tension is given by $\gamma = \text{Force}/\text{Perimeter}$ where the force acting on the Wilhelmy plate is measured *in situ* and divided by the perimeter of the plate.

To coat a substrate with a monomolecular film, the trough (Model 311D, Nima, Coventry, UK) was cleaned by repetitive aspiration and refilling of the subphase. The subphase was equilibrated to the desired temperature. To ensure the cleanness of the trough the barrier was moved from the maximum area to the minimum area with only the subphase present. If this compression resulted in an increase of surface pressure

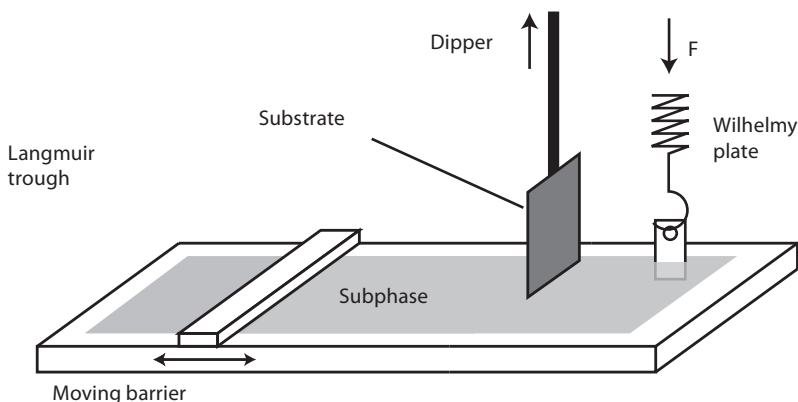


Figure 1.2 – Schematic illustration of the Langmuir trough with dipper. By moving the barrier the surface pressure Π is adjusted which is measured by the Wilhelmy plate. The dipper with attached substrate is moved upwards for LB deposition on hydrophilic substrates. For Langmuir–Schaefer transfers the substrate is manually placed slightly oblique over the subphase and dropped gently.

below 0.2 mN m^{-1} the subphase was considered clean. The surface pressure at this condition was set to $\Pi = 0 \text{ mN m}^{-1}$. A substrate was attached to the dipper and immersed into the subphase. Lipid solution was spread on the subphase without increasing the surface pressure significantly. After evaporation of the solvent the compression was started with a compression rate of $10 \text{ cm}^2 \text{ min}^{-1}$. After reaching the preset pressure of 30 mN m^{-1} the barrier stopped. The pressure versus area data was saved and is referred to as isotherm. The substrate was withdrawn at the specified transfer speed with the barrier moving to keep the surface pressure constant. The coated substrate was allowed to dry for a short time before being further processed. To assess the quality of the transferred film a transfer ratio was calculated. This is defined as the area reduction by the transfer on the Langmuir trough divided by the surface area of the immersed substrate. While the first is given by the barrier position before and after the transfer, the surface area of the substrate has to be calculated taking into account the thickness of the substrate and the immersion depth (wetted length). The transfer ratio has been unity for all transfers within the experimental error of 2 %.

1.2.2 Langmuir–Schaefer Transfer

Similar to the LB transfer, the Langmuir–Schaefer (LS) transfer transplants an amphiphilic monolayer from the air–water interface onto a solid substrate. For the LS transfer a hydrophobic substrate is required. Here, previously LB coated substrates are

used. The monolayer on the subphase is prepared as outlined in the previous section but without immersing the substrate into the subphase before. After reaching the desired surface pressure, the substrate is placed with the surface to be coated facing downward, slightly oblique above the subphase and dropped gently. The substrate is allowed to float on the subphase for several seconds before being pressed into the subphase. The substrate is moved in the subphase to the other side of the barrier and transferred to the corresponding observation chamber without exposing the coated surface to air.

1.2.3 Vesicle Fusion

Beside the methods discussed in the previous sections for preparation of supported membranes, vesicle fusion is an alternative method which can be used for the completion of an already present monolayer to a bilayer or for the full deposition of a bilayer on a substrate^{71,72}. Vesicle fusion allows fast and parallel preparation of samples with the drawback of only minor control over the film properties. It is not possible to control nor measure the lateral pressure in the resulting bilayer. Furthermore, no quality control comparable to the transfer ratio of a LB transfer is available.

First, the desired mixture of lipid molecules is prepared in chloroform. The chloroform is slowly evaporated using dried nitrogen or by applying vacuum while rotating the flask. For complete removal of the solvent the mixture is stored in vacuum overnight. To prepare vesicles the dry lipids are resuspended in water or aqueous buffer to a concentration of 1 mg ml^{-1} . A turbid suspension is formed which contains multilamellar lipid vesicles with a broad size distribution. In order to reduce the size and make the vesicles unilamellar the suspension is sonicated using a titanium tip sonifier until it becomes clear. Titanium fragments of the sonicator tip present in the suspension can be separated by short centrifugation with several thousand g. The suspension is added to a substrate with a lipid monolayer transferred by LB transfer. The surface is incubated for one hour at 40°C . To avoid deposition of more than one bilayer the suspension is then exchanged by water or aqueous buffer.

1.3 REFLECTION BASED TECHNIQUES

Many of the observational techniques used in this work measure a property of a reflected electromagnetic wave or the analogous description of neutrons. The analysis of this data relies on the theory of Fresnel reflectivity irrespective of the used property⁷³. The basic geometry is an incident beam being reflected from the sample as in Figure 1.3 on the following page. The detector is placed at an angle equal to the incident angle to measure the specularly reflected beam. Depending on the method, different properties of the reflected beam are measured. In the case of ellipsometry the polarization state is measured while for X-ray and neutron reflectivity the intensity is of interest. As all

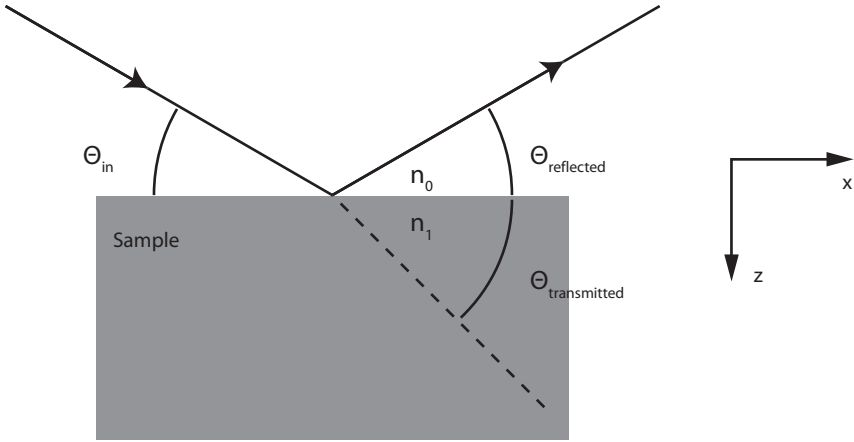


Figure 1.3 – Schematic illustration of the reflectivity geometry. An electromagnetic wave in ambient medium with refractive index n_0 is incident on a sample at an angle Θ_{in} . The wave is reflected at an angle $\Theta_{reflected} = \Theta_{in}$ and refracted at an angle $\Theta_{transmitted}$.

these methods share the same theoretical foundation, first an introduction will be given to the Fresnel reflectivity followed by an elegant treatment of multilayer systems based on the Abelès matrix method⁷⁴. After this the experimental methods are discussed in detail in the following sections.

Fresnel Reflectivity

We consider the geometry shown in Figure 1.3. The angle of incidence Θ_{in} and angle of reflection $\Theta_{reflected}$ are equal in magnitude while the relation to the angle of refraction $\Theta_{transmitted}$ is given by Snell's law

$$n_0 \cos \Theta_{in} = n_1 \cos \Theta_{transmitted}. \quad (1.1)$$

Starting from the Maxwell equations boundary conditions that must be met can be derived⁷⁵. Notably this is the continuity of the electric field component parallel to the interface across the interface and that the normal component of the electric field times the electric permittivity ϵE is the same on both sides of the interface. The resulting ratios of reflected to incident and transmitted to incident amplitude of the electric field depend on the orientation with respect to the plane of incidence. Therefore we get four Fresnel equations. For the electric field components parallel to the plane of incidence

this results in

$$r_{\parallel} = \frac{n_1 \sin \Theta_{\text{in}} - n_o \sin \Theta_{\text{transmitted}}}{n_o \sin \Theta_{\text{transmitted}} + n_1 \sin \Theta_{\text{in}}} \quad \text{and} \quad (1.2)$$

$$t_{\parallel} = \frac{2n_o \sin \Theta_{\text{in}}}{n_o \sin \Theta_{\text{transmitted}} + n_1 \sin \Theta_{\text{in}}} \quad (1.3)$$

with the amplitude reflection coefficient r_{\parallel} and the amplitude transmission coefficient t_{\parallel} . Similar for the electric field normal to the plane of incidence the amplitude coefficients are given by

$$r_{\perp} = \frac{n_o \sin \Theta_{\text{in}} - n_1 \sin \Theta_{\text{transmitted}}}{n_o \sin \Theta_{\text{in}} + n_1 \sin \Theta_{\text{transmitted}}} \quad \text{and} \quad (1.4)$$

$$t_{\perp} = \frac{2n_o \sin \Theta_{\text{in}}}{n_o \sin \Theta_{\text{in}} + n_1 \sin \Theta_{\text{transmitted}}}. \quad (1.5)$$

The intensity of the reflected wave R is given by the square of the amplitude coefficients. The intensity of the transmitted wave T has to be corrected for the change in propagation direction

$$R_{\parallel,\perp} = r_{\parallel,\perp}^2, \quad T_{\parallel,\perp} = \frac{n_1 \cos \Theta_{\text{transmitted}}}{n_o \cos \Theta_{\text{in}}} t_{\parallel,\perp}^2. \quad (1.6)$$

Fresnel Reflectivity with Abelès Matrix Method

To account for a more complex sample with several changes in refractive index normal to the interface the formulas derived for Fresnel reflectivity must be applied to each interface. To avoid the tedious explicit consideration of back reflections an elegant framework dealing intrinsically with multiple reflections is presented⁷⁶. This framework has been first introduced by Abelès⁷⁴. Consider a planar structure of layers on a substrate in an environment as shown in Figure 1.4 on the following page. The layers and bordering media are homogeneous, linear and isotropic with complex refractive indices n_j and the layers have thicknesses d_j . The distinction into the two polarizations is not explicitly denoted in the remainder of this paragraph. Each of the following equations relates therefore to two equations, one for each polarization. A two component vector represents the electric field E in a plane with constant z . Forward traveling waves which are directed towards the substrate constitute the first component denoted by (+) whereas waves traveling backwards form the second component and are denoted by (-)

$$\mathbf{E} = \begin{pmatrix} E^+(z) \\ E^-(z) \end{pmatrix}. \quad (1.7)$$

The change in electric field across an interface and through media with a certain thickness can now be written as a matrix multiplication. The characteristic matrix for an

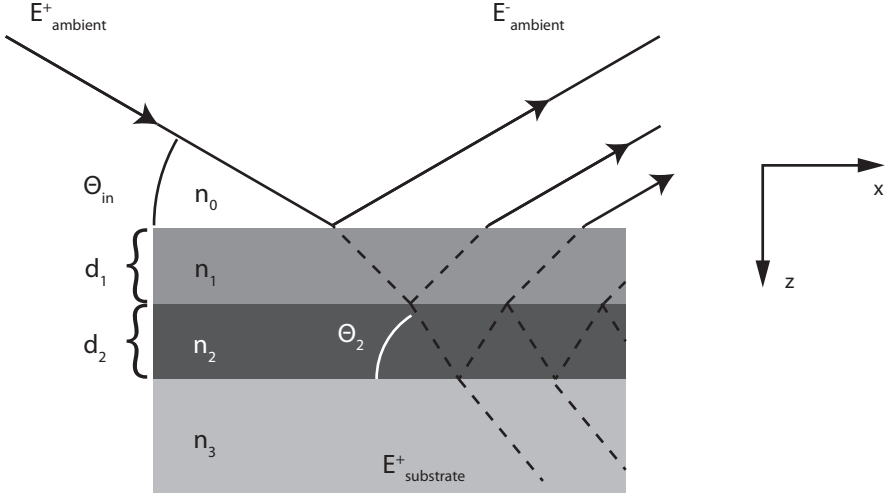


Figure 1.4 – Schematic illustration of the reflectivity geometry considered for the Abeles matrix method. An electromagnetic wave is incident on a sample with several layers at an angle Θ_{in} . The wave is reflected and refracted at each interface.

interface between layer $(j - 1)$ and j , $I_{(j-1)j}$ reads

$$I_{(j-1)j} = \begin{pmatrix} 1/t_{(j-1)j} & r_{(j-1)j}/t_{(j-1)j} \\ r_{(j-1)j}/t_{(j-1)j} & 1/t_{(j-1)j} \end{pmatrix} \quad (1.8)$$

with the amplitude coefficients r and t defined in the previous paragraph. In a similar fashion the characteristic matrix for the change due to a layer with thickness d_j and refractive index n_j can be written as

$$L_j = \begin{pmatrix} e^{i\beta} & 0 \\ 0 & e^{-i\beta} \end{pmatrix} \quad (1.9)$$

with $\beta = \frac{2\pi d_j n_j}{\lambda} \sin \Theta_j$ where λ is the wavelength of the electromagnetic wave and Θ_j is the angle between the direction of propagation and the interface in layer j . By multiplying the characteristic matrices of the components, the characteristic matrix for the complete layer system is obtained:

$$S = I_{01} L_1 I_{12} \dots L_{n-1} I_{(n-1)n} I_n. \quad (1.10)$$

As in the substrate no reflected wave is traveling backward we can write the change in electric field over the system as

$$\begin{pmatrix} E_{\text{Ambient}}^+ \\ E_{\text{Ambient}}^- \end{pmatrix} = \begin{pmatrix} S_{11} & S_{12} \\ S_{21} & S_{22} \end{pmatrix} \begin{pmatrix} E_{\text{Substrate}}^+ \\ 0 \end{pmatrix}. \quad (1.11)$$

Analogous to the Fresnel reflectivity for one interface we can now write the amplitude coefficients of the layer system for either state of polarization as

$$r = \frac{E_{\text{Ambient}}^-}{E_{\text{Ambient}}^+} = \frac{S_{21}}{S_{11}}, \quad (1.12)$$

$$t = \frac{E_{\text{Substrate}}^+}{E_{\text{Ambient}}^+} = \frac{1}{S_{11}}. \quad (1.13)$$

1.3.1 X-Ray Reflectivity

For X-rays the refractive index n can be written as $n = 1 - \delta + i\beta$ where δ is positive and on the order of 10^{-5} and β , the absorption coefficient, is in many cases even smaller. Instead of the geometric angle Θ we consider in X-ray reflectivity the wave vector and especially its component normal to the interface k_z which are related by

$$k_j = n_j \sin \Theta_j k_o. \quad (1.14)$$

Taking the Fresnel equation for normally polarized reflected light, Equation (1.4), we can write

$$r_{\perp} = \frac{k_o - k_1}{k_o + k_1}. \quad (1.15)$$

In the case of parallel polarized reflected light, Equation (1.2), we get

$$r_{\parallel} = \frac{k_o \frac{n_1}{n_o} - k_1 \frac{n_o}{n_1}}{k_o \frac{n_1}{n_o} + k_1 \frac{n_o}{n_1}}. \quad (1.16)$$

Multiplying denominator and nominator with $\frac{n_1}{n_o}$ results in

$$r_{\parallel} = \frac{k_o \left(\frac{n_1}{n_o} \right)^2 - k_1}{k_o \left(\frac{n_1}{n_o} \right)^2 + k_1}. \quad (1.17)$$

The term $\left(\frac{n_1}{n_o} \right)^2$ can be approximated by 1 since refractive indices for X-rays are small deviations from 1. As first derived by Parratt⁷⁷, we find that the polarization state needs not to be considered for X-ray reflectivity since $r = r_{\parallel} = r_{\perp}$ in good approximation.

The small wavelength of X-rays make the technique sensitive to interface roughness on an atomic level and require the roughness to be considered. This can be done by modifying the reflection amplitude coefficient according to Croce & Névoit⁷⁸

$$r_{j(j+1)} = \frac{k_j - k_{(j+1)}}{k_j + k_{(j+1)}} \exp\left(-2k_j k_{j+1} \sigma_{j(j+1)}^2\right). \quad (1.18)$$

In the picture of the interface this models a gaussian roughness by modifying the abrupt and stepwise change from one index of refraction to another into a smooth transition with width σ . Mathematically an error function is multiplied with the refractive index profile. From the reflection amplitude coefficient r of the complete system, the intensity of the reflected wave is given by $R(q_z) = |r|^2$ with $q_z = 2k_o \sin \Theta_o$.

Experimental Setup

X-ray reflectivity measurements were carried out at the ID10b beamline of the European Synchrotron Radiation Facility (ESRF, Grenoble, France) and at the Institut für Röntgenphysik (Georg-August-Universität Göttingen, Göttingen, Germany) in the group of Prof. Tim Salditt using a Bruker AXS D8 Advance X-ray reflectometer equipped with a Molybdenum anode and Göbel mirrors (Bruker AXS, Karlsruhe, Germany). The energy of the synchrotron beamline was set to 20 keV while the in-house reflectometer uses the Mo K_α line with an energy of 17.48 keV⁷⁹. These high energies were used in favor to the commonly used 8 keV of the Cu K_α line as the absorption in water is significantly reduced⁸⁰. For the measurement the sample was placed on the stage in a cell bounded by Kapton (Kapton® polyimide film, DuPont, Luxembourg) in beam direction analogous to the design presented by Miller *et al.*^{53, 54}. The length in beam direction was 10 mm for measurements in Göttingen, and 20 mm for measurements in Grenoble, taking advantage of the higher flux. The measurement commenced after placing the samples at their designated place and having been aligned with respect to the X-ray beam in all three degrees of freedom using the control software of the instrument. Starting from an incident angle $\Theta_{in} = 0$ corresponding to $q_z = 0$, the incident angle was increased stepwise and the reflected intensity was recorded. For larger angles the counting times were increased to counter the decrease in reflected intensity. The measured reflectivity intensity was divided by the intensity of the incoming beam and the ratio plotted versus q_z as reflectivity curve. The analysis is model based, requiring knowledge of the measured sample in terms of refractive index and layer structure. Recently model-free approaches have become popular allowing a less biased analysis⁸¹. Starting from a model based on rough estimates the reflectivity curve of the model can be calculated and compared to the measured data. Variation of the model parameters can then be used to increase the match between model and experiment. These steps were performed using MOTOFIT⁸² running on Igor Pro (Wavemetrics, Lake Oswego, Oregon, USA).

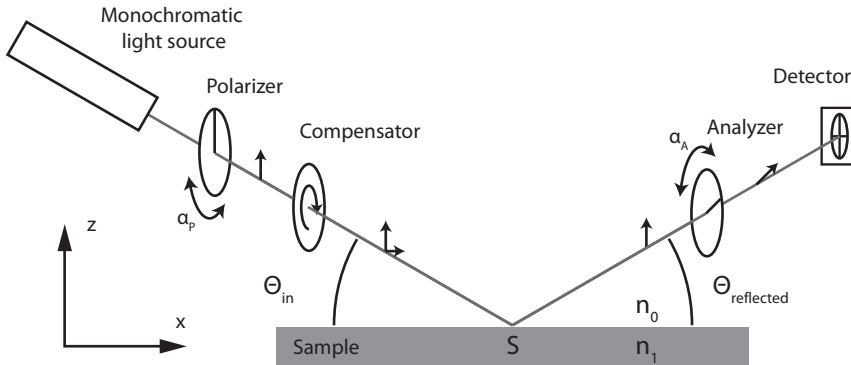


Figure 1.5 – Schematic illustration of an ellipsometer in the PCSA configuration. Monochromatic light at arbitrary polarization passes through a polarizer and a $\lambda/4$ wave plate denoted compensator. This results in an elliptic polarization between linear polarized and circular polarized depending on the orientation of the polarizer to the compensator. The light is reflected at a sample S at an angle $\Theta_{in} = \Theta_{reflected}$ before passing through a second polarizer denoted analyzer and the intensity of the light being measured by a detector.

1.3.2 Ellipsometry

As a further reflection based technique, ellipsometry relies on the change in polarization by the sample. As such, its resolution is not limited by the wavelength of the electromagnetic wave but by the ability to discriminate between different polarization states and the strength with which the polarization is affected by the sample. In practical instruments the resolution can reach down to several Ångstrom. Long before being used to measure layer thicknesses, this method has been useful for the determination of refractive indices⁸³. In this section we discuss first the experimental arrangement before proceeding to the theoretical description of the measurement process. Furthermore extensions to the technique are introduced to achieve lateral resolution and to measure thicknesses on the order of the wavelength of the used light.

Experimental Setup

In this study the ellipsometer used is a Multiskop from Optrel (Kleinmachnow, Germany)⁸⁴. The setup is equipped with a Helium–Neon–laser operating at a wavelength of 6328 Å. Light is emitted with random polarization as shown schematically in Figure 1.5. This light passes through a polarizer from which linear polarized light emerges. The polarizer can be rotated to select any plane for the polarized light by a computer controlled rotary stage. Depending on the plane of polarization with which the wave enters the $\lambda/4$ wave plate denoted as compensator, any state of elliptical polarization

from linear polarized to circular polarized light can be emitted. This light is directed onto the sample at an angle Θ_{in} . The reflected wave is modified by the sample according to the Fresnel equations as discussed in Section 1.3 on page 12. The reflected light passes through a rotatable polarizer (analyzer) before being detected by a photodiode. Precise sample alignment is facilitated by a quadrant photo diode used as detector. This configuration is called PCSA configuration derived from the arrangement of the optically active elements. The principle of a null-ellipsometric measurement is to set the polarization of the incident light such that the reflected light is linear polarized. Setting the analyzer normal to the plane of polarization of the reflected light leads to an extinction and thus a minimum in intensity at the detector.

Samples were either placed directly on the specimen holder, or for under water measurements, inside a prismatic quartz cuvette (Hellma, Müllheim, Germany) with a 70° angle between the base and the two observation windows. The front of the cuvette was sealed with a piece of glass spread with silicon grease (Baysilone silicone paste, low viscosity, Bayer, Leverkusen, Germany). The back reflection of the laser from the cuvette was directed as close as possible to but not into the laser exit aperture.

The first step for an ellipsometry measurement is the alignment of the sample with respect to the incident beam analogous to the X-ray measurement. The position in z -direction is adjusted by setting $\Theta_{\text{in}} = \Theta_{\text{reflected}} = 0$ and positioning the sample in z -direction such that it reduces the detected intensity to half compared to an unobstructed beam path. Then by setting $\Theta_{\text{in}} = \Theta_{\text{reflected}}$ to the desired value the sample is adjusted to be normal to the z -axis. This ensures that the reflected light is detected in the center of the detector. The analyzer and polarizer are rotated to minimize the intensity at the detector. In the vicinity of the minima for polarizer and analyzer a parabolic dependency of the intensity on the angular position can be used to determine the position of the minima at α_A and α_P with high precision.

Ellipsometric Angles

The change of polarization state by the sample is parametrized by the ellipsometric angles Ψ and Δ . They are related to the reflection amplitude coefficients discussed in previous sections via

$$\tan \Psi e^{i\Delta} = \frac{r_{\parallel}}{r_{\perp}} = \frac{|r_{\parallel}|}{|r_{\perp}|} e^{i(\phi_{\parallel} - \phi_{\perp})}. \quad (1.19)$$

The change in polarization of the electromagnetic wave on the way through the experimental setup is followed using Jones calculus^{73,85}. This results in a relation between the orientation of the optical components and the ellipsometric angles. For null-ellipsometry with the compensator oriented at -45° with respect to the plane of incidence the relation is

$$\tan \Psi e^{i\Delta} = \tan \alpha_A \exp\left(i\left(2\alpha_P + \frac{\pi}{2}\right)\right) \quad (1.20)$$

with the orientation of the analyzer α_A and the orientation of the polarizer α_P with respect to the plane of incidence.

Determination of n and d from the ellipsometric angles

Since it is only possible to invert the Fresnel equations and the extension of the Abelès matrix method in few special cases, the analysis has to be model based as in the case of X-ray reflectivity. First, a suitable layer system according to the Abelès matrix method with refractive indices n and thicknesses d is set up. From this the amplitude coefficients are calculated and, using Equation (1.19), converted to the ellipsometric angles. The deviation from the measured ellipsometric angles is weighted by

$$\chi^2 = \frac{(\Psi_{\text{Measured}} - \Psi_{\text{Model}(n,d)})^2}{\Psi_{\text{Model}(n,d)}} + \frac{(\Delta_{\text{Measured}} - \Delta_{\text{Model}(n,d)})^2}{\Delta_{\text{Model}(n,d)}}. \quad (1.21)$$

The model parameters n and d are then varied in order to minimize χ^2 . This analysis relies on a good previous knowledge of the sample structure and certain ambiguities cannot be resolved using this technique. As discussed in the following section, the periodicity of the ellipsometric angles with film thickness allows an identification of film thickness only up to a repetition length. Model based fitting was done using the self-written software Ell which is attached to this thesis in Appendix A.

Ellipsometric Period

When the nulling condition is fulfilled for a layer with thickness d a change of the layer thickness by a repeat length given by

$$D = \frac{1}{2} \frac{\lambda}{\sqrt{n_j^2 - n_o^2 \cos^2 \Theta}} \quad (1.22)$$

results in repeated fulfillment. The repeat length D is called the ellipsometric period and depends on the angle of incidence Θ and the wavelength λ , as well as the refractive index n_o of the ambient medium and the refractive index n_j of the layer whose thickness is considered.

Imaging Ellipsometry

The diameter of the laser beam of the Multiskop is 1300 μm . Lateral features below this size are averaged within the measurement. A higher lateral resolution can be achieved with little trade-off in resolution normal to the interface by replacing the point detector by a 2D position sensitive detector (EHD[®]kamPro02, EHD imaging, Damme,

Germany) and adding an image forming optic (M-Plan APO 10 \times , Mitutoyo, Neuss, Germany) in the beam path after the sample. In this case the incident angles accessible are restricted by the extent of the image forming objective. For smaller angles Θ_{in} a large working distance in comparison to the physical diameter of the objective has to be chosen. This limits the available numerical aperture by which the maximum lateral resolution is defined. In the current setup the nominal numerical aperture is $\text{NA} = 0.28$ but the objective-sample distance is much larger than the indicated working distance resulting in a significant reduction of achievable lateral resolution. A second drawback is the tilt between objective and sample. The depth of focus limits the area in the plane of incidence on the sample which can be observed sharply. Other ways to achieve microscopic resolution parallel to the interface have been suggested by Neumaier *et al.*⁸⁶, Linke & Merkel⁸⁷ without the drawbacks of the simple extension mentioned above.

While for single spot ellipsometry each measurement can be analyzed as outlined before, the simple extension to imaging ellipsometry used in this study results in an intensity image for a given pair of ellipsometric angles. If the lateral gradient in thickness change is smaller than half of the ellipsometric period over the lateral distance of the microscopic resolution, a height profile can be extracted from the positions where the nulling condition is met and which are therefore minimal in intensity. For a water film ($n_{\text{H}_2\text{O}} = 1.333$) in air ($n_{\text{Air}} = 1.000$) the ellipsometric period becomes $D = 2900 \text{ \AA}$ with the used setup. A finer resolution can be obtained by off-null ellipsometry⁸⁸ where the parabolic relationship of the intensity minimum around the nulling condition is used. For a quantitative analysis a set of two ellipsometric images is necessary which were taken when the nulling condition was met at two distinct positions.

Ellipsometry of the Three-Phase Contact Line

The description of the combination of the preparational Langmuir trough used for LB transfers with the observation using imaging ellipsometry is postponed to Section 3.2.1 on page 59. There, a motivation for this design is given followed by a detailed characterization of the setup.

1.4 FLUORESCENCE MICROSCOPY

To assess the distribution of lipids and the homogeneity of membranes, fluorescent markers were incorporated into the samples and observed with microscopy. A Zeiss Axiovert 200 (Göttingen, Germany) with a mercury lamp (HBO 100, Osram, Munich, Germany) for illumination and suitable filter sets was used. Details of the filter sets are shown in Table 1.1 on the facing page. Images were recorded with a CCD-camera

Table 1.1 – Filter sets used for fluorescence microscopy. The wavelength for excitation filter and emission filter denote the center wavelength and the width of the bandpass.

Fluorescent marker	Excitation / nm	Dichroic mirror / nm	Emission / nm	Producer
Texas Red*	560/40	585	630/75	Carl Zeiss
TRITC	525/45	560	595/60	Omega Optical

(Orca ER, Hamamatsu Photonics, Herrsching, Germany) and transferred via a frame grabber card (Coreco Imaging, Gröbenzell, Germany) to digital storage.

Fluorescence Microscopy of the Three-Phase Contact Line

Similar to the combination of ellipsometer and Langmuir trough, this setup was specifically designed for the observation of stripe pattern formation discussed in Section 3.2.2 on page 64. There, a detailed description of this setup is given.

CHAPTER 2

TRANSVERSAL STRUCTURE OF LIPOPOLYMER LAYERS

To overcome the implications accompanying the close membrane substrate contact in supported membranes, polymer-supported membranes were used. The foremost question is regarding the distance between membrane and substrate upon addition of the polymer support. To this end, two reflection based experimental methods which complement each other were utilized. The variation in membrane to substrate distance with polymer length and polymer content in the membrane was studied.

The stepwise preparation of the membrane via Langmuir-Blodgett transfer + vesicle fusion or Langmuir-Blodgett (LB) transfer + Langmuir-Schaefer (LS) transfer allows the characterization of the intermediate preparation state of a polymer supported monolayer. Furthermore, composition in the leaflets can be varied separately allowing a more realistic replica of membranes found in living organisms. The variation of ambient conditions allows the extraction of the behavior of the polymer support and can be used to gain a deeper insight into the membrane substrate interactions.

Samples were prepared as outlined in Chapter 1 by coating cleaned substrates with a LB transfer. To avoid demixing of lipid and lipopolymer the substrates were withdrawn swiftly with 30 mm min^{-1} from the subphase while keeping the surface pressure constant at 30 mN m^{-1} . The samples were allowed to dry for at least several minutes before being measured. In the case of X-ray reflectivity the monolayer was transferred several days before the measurement. From ellipsometry no degradation of the samples could be observed over several months when stored at normal lab conditions of $20 \text{ }^\circ\text{C}$ and 30 \%RH - 70 \%RH . Completion to a bilayer proceeded either by vesicle fusion or by a LS transfer.

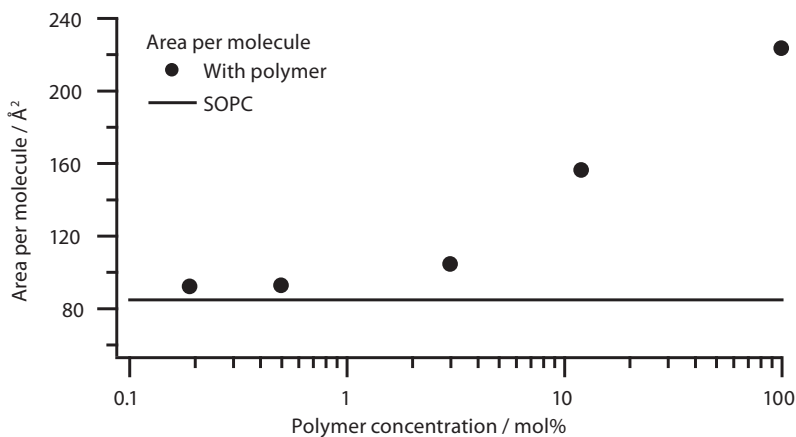


Figure 2.1 – Area per molecule as a function of lipopolymer concentration at a surface pressure of $\Pi = 25 \text{ mN m}^{-1}$. At low lipopolymer concentrations almost no change in area per molecule is observed. For higher concentrations ($c \gtrsim 1 \text{ mol } \%$) the area per molecule increases strongly. The black solid line indicates the area per molecule for pure SOPC, i.e., 0 mol %.

2.1 MONOLAYERS AT THE LIQUID–GAS INTERFACE

The isotherms of the mixtures including lipopolymers show two distinct differences to the isotherm of SOPC. First, depending on the concentration of lipopolymer, the area per molecule at a given surface pressure increases. Second, a plateau may be observed reminiscent of a phase transition of either component. The second observation has been shown by Wurlitzer *et al.*⁸⁹ to be due to a reorganization of the alkyl chains as a result of the decreased conformational freedom of the polymer chains, excluding a phase transition. This is closely related to the increased area per molecule in the presence of lipopolymers where the polymer chains constitute a significant contribution near the interface. A similar area per molecule for lipopolymers has also been reported by Lüdtkke *et al.*⁹⁰.

The variation of the area per molecule with lipopolymer concentration is shown in Figure 2.1. The resulting area per molecule can be understood as a balance between entropic desire of the polymer chain to take a globular shape and the steric interaction in the alkyl chain region. For low concentrations of lipopolymers almost no change in area per molecule is found⁴⁶. There, the reduction in entropy due to the confinement of the polymers is small and the area per molecule is defined by the alkyl chain interactions. Even in the absence of polymer–polymer interactions, because of the direct coupling of the polymer chain to the alkyl chain, the head groups of the surrounding lipids reduce

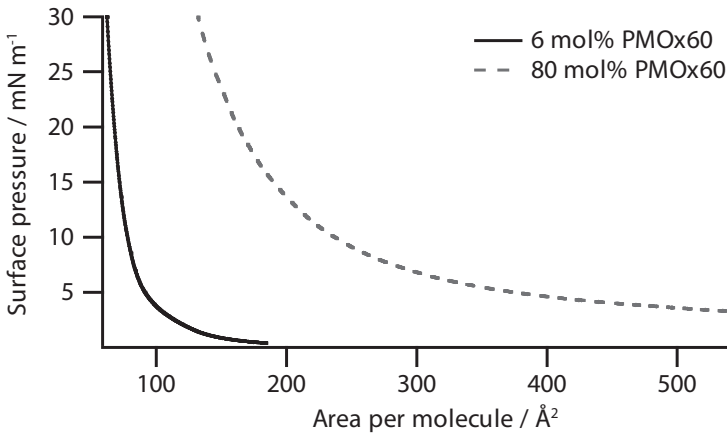


Figure 2.2 – Isotherms of lipid-lipopolymer mixtures at 20 °C. **Solid line:** SOPC with 6 mol % PMOx60. **Dashed line:** SOPC with 80 mol % PMOx60. The films used for recording these isotherms were transferred and measured using X-ray reflectivity.

the possible polymer conformations. The same holds for higher lipopolymer concentrations of short polymer chains⁴⁶. In this case, the reduction in entropy to accommodate the polymer chain in the remaining volume is smaller than the steric interaction of the lipids. With increasing concentration of long lipopolymer the area per molecule at a constant surface pressure increases as the reduction of available conformations for the polymer chain becomes a significant contribution. In Figure 2.1 on the preceding page this transition is seen below 3 mol % which corresponds to an average distance d_{lat} between the lipopolymers of one Flory radius R_f . The polymers are in contact when $d_{\text{lat}} < 2R_f$. The deformation of the polymer from its unperturbed globular shape to the confined volume available at high concentrations becomes increasingly more energetically costly and results in a higher area per molecule. The overestimation of the area per molecule for a pure SOPC monolayer by a factor of 1.3 compared to Smaby *et al.*⁹¹ and Marsh⁹² is most likely due to an increased concentration of lipids in the stock solution used to prepare the mixtures. Especially for the calculation of the volume of a single polymer chain at high polymer concentrations the change in area per molecule becomes significant. This is discussed in detail in Section 2.4.1 on page 43. In Figure 2.2 isotherms of PMOx60 for two concentrations are shown. The isotherm for the lower concentration of 6 mol % shows only marginal differences to the isotherm of the lipid matrix whereas the onset of the surface pressure for the high concentration is at large areas per molecule. The higher compressibility can be interpreted to be caused by the decrease in conformational freedom of the polymer chain. The aforementioned plateau is not observed here for the polymer chain with 60 monomer units, as the surface pres-

sure required to induce this change in conformation in the alkyl chain arrangement is more than required for a film breakdown at $\approx 40 \text{ mN m}^{-1}$. This is also consistent with the observations of Lüdtke *et al.*⁹⁰ and Wurlitzer *et al.*⁸⁹.

2.2 MONOLAYERS AT THE SOLID–GAS INTERFACE

2.2.1 Ellipsometry

Prior to the LB transfer of the proximal monolayer the substrates were measured using ellipsometry to gain the thickness and refractive index of the oxide layer. This information is required for the subsequent analysis of the measured data based on a layer model using the formalism outlined in Section 1.3 on page 13. The refractive index of the crystalline silicon was set to $n_{\text{Si}} = 3.882 - i0.019$ ⁹³. The thickness of the oxide layer of the cleaned substrate was found to be $d_{\text{SiO}_2} = 13.8 \text{ \AA} \pm 1.1 \text{ \AA}$ for a refractive index $n_{\text{SiO}_2} = 1.457$ averaged over several samples⁹³. This is about 2 \AA less than the oxide layer thickness before the cleaning procedure. As a reference for a minimal membrane–substrate separation a transferred monolayer of pure SOPC was measured. The parameters from this measurement for the lipid layer were used in all analyses of monolayers with polymer present. Since the lipid anchors of the lipopolymers used, distearyl ($2 \times \text{C18:o}$) and dipythanyl ($2 \times 4\text{Me C16:o}$), are different from the alkyl chains present in SOPC (C18:o , C18:1), DPhPC with a diphytanoyl lipid moiety which is fluid at the experimental conditions was measured for comparison. The difference in ellipsometric angles shown in Figure 2.3 is small and results in a thickness difference well below 1 \AA for the two lipids. The use of SOPC as a reference instead of the alkyl chain analogue DSPC is therefore justified. For SOPC the thickness resulting from a three layer model with a refractive index $n_{\text{SOPC}} = 1.44$ ⁹⁴ for the lipid layer is $d_{\text{SOPC}} = 18.1 \text{ \AA} \pm 1.3 \text{ \AA}$. To account for the presence of lipopolymer an additional layer between the silicon dioxide and the lipid layer is introduced into the model used for analysis. The parameters of the model are presented in Table 2.1 on the facing page summarizing the above men-

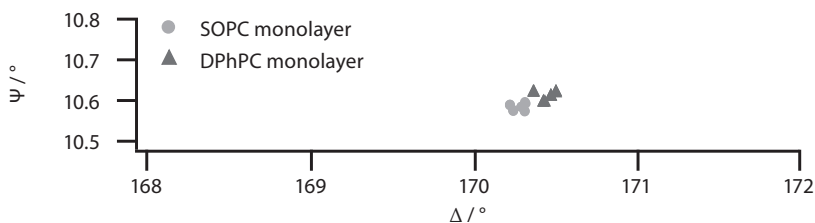


Figure 2.3 – Ψ vs. Δ plot measured from monolayers of SOPC and DPhPC on silicon substrate. Only a slight difference can be seen between the two lipid anchors.

Table 2.1 – Layer model used for ellipsometric measurements on dry monolayers showing the layer thickness d , the real part of the refractive index n and the imaginary part k . The parameters for the lipid layer were obtained from a reference measurement on a pure SOPC monolayer prepared under the same conditions. The illumination wavelength is $\lambda = 6328 \text{ \AA}$ and the incident angle on the substrate $\Theta = 20^\circ$. The parameters for the polymer layer n_{Polymer} and d_{Polymer} were used as fitting parameters.

Layer	$d / \text{\AA}$	n	k
Air	∞	1.000	0
Lipid	18.1	1.440	0
Polymer	d_{Polymer}	n_{Polymer}	0
SiO ₂	13.8	1.457	0
Si	∞	3.882	-0.019

tioned reference measurements. To assess the effect of concentration and number of monomer units, a concentration series was measured for each lipopolymer at ambient humidity conditions. The Ψ and Δ values for the four series are displayed in Figure 2.4 on the next page. Already from these raw data a clear trend can be observed. Starting from a fixed (Ψ, Δ) pair for 0 mol % lipopolymer (black diamonds), Δ is shifted to lower and Ψ to higher values with increasing polymer concentration. Comparing the data between different number of monomer units, a larger shift for a higher number of monomer units is found. The concentration series for the four lipopolymers were analyzed using the parameters for a three layer model presented in Table 2.1. As the resulting thicknesses for the polymer layer n_{Polymer} are well below 100 \AA an independent determination of thickness and refractive index is not possible from these monochromatic measurements at one angle of incidence⁹⁵. The refractive index was therefore fixed to $n_{\text{Polymer}} = 1.50$ as the measurements were performed in an ambient humidity of $\approx 60 \text{ \%RH}$ ⁹⁶. The resulting thicknesses for the polymer layer d_{Polymer} are presented in Figure 2.5 on page 29. A linear dependence of the thickness on the lipopolymer concentration is expected for low concentrations where the average distance is larger than the extent of the lipopolymers given by their Flory radius R_f and where the area per molecule is virtually unchanged by the presence of the lipopolymers. Based on the present data an analytical relationship for the thickness at higher concentrations cannot be given. But the qualitative effect of the increase in area per molecule is a decline in growth of polymer thickness with concentration.

For one lipopolymer (PMOx60) the influence of ambient humidity was studied. The ambient humidity has the effect of an osmotic pressure onto the sample counteracting the interactions of the sample components⁹⁷. Control of the ambient humidity was provided by saturated salt solutions as listed in Table 2.2 on page 30. The sample was placed inside a prismatic cuvette together with the salt solution and the cuvette

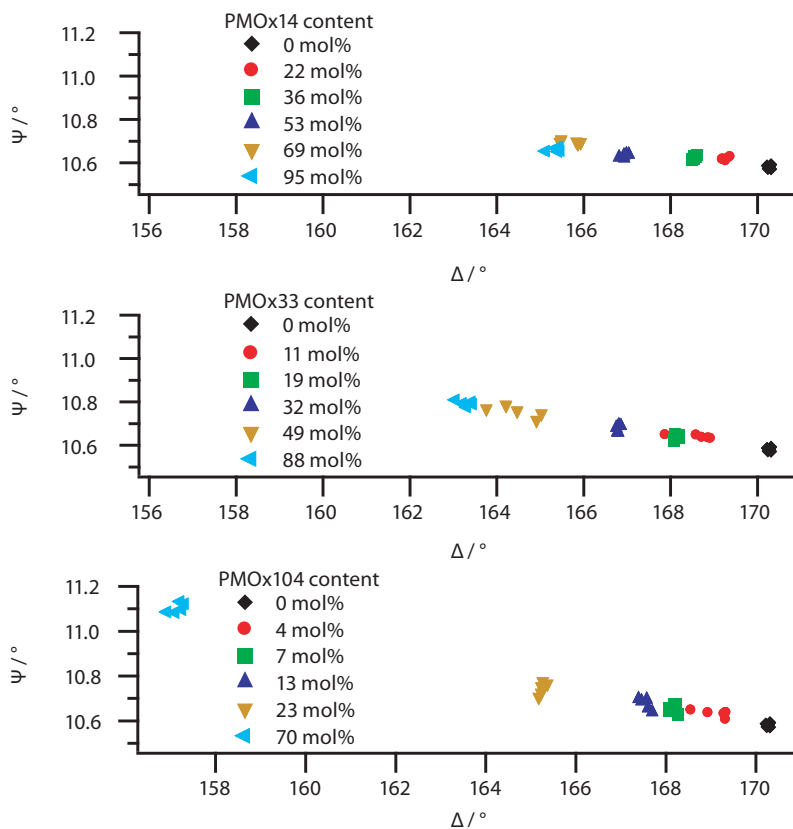


Figure 2.4 – Ψ vs. Δ plots for number of monomer units $n = 14, 33, 104$ from top to bottom and different concentrations for each polymer length as indicated in the graph. Measurements were done under ambient conditions with a relative humidity around 60 % at 20 °C.

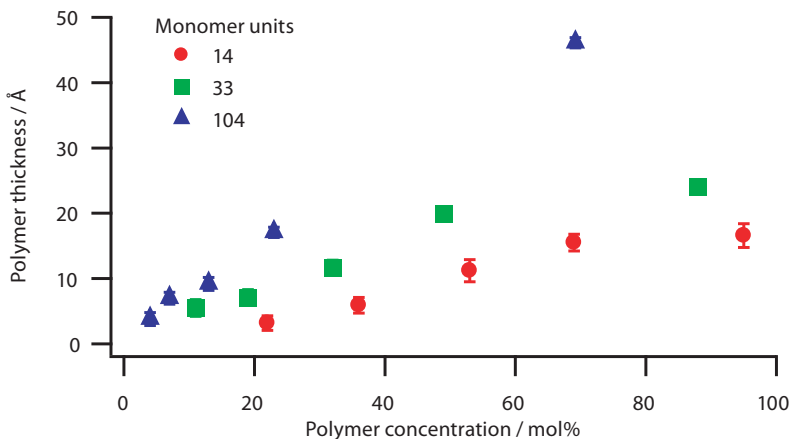


Figure 2.5 – Polymer layer thickness for $n_{\text{polymer}} = 1.50$ and number of monomer units $n = 14, 33$ and 104 . The increase with polymer concentration is not linear due to the simultaneous expansion of the area per molecule. A clear ordering can be observed with a stronger build up of the polymer layer for longer polymers.

was sealed using low viscosity silicon grease. The equilibration of the sample was monitored by repeated ellipsometric measurements. Especially for low relative humidities long equilibration times were required to ensure the homogeneous prevalence of the desired humidity. The ellipsometric angles were analyzed with the model defined by the parameters shown in Table 2.1 on page 27. The fit quality as assessed from the function of merit χ^2 (Equation (1.21)) is shown in Figure 2.6 on the following page for a range of refractive indices n_{polymer} and thicknesses d_{polymer} . Going from low humidity in the upper left panel to high humidity in the lower right panel, an increase in thickness can be observed due to hydration of the polymer layer. Along with the increase in water content the refractive index becomes restrained to values close to the refractive index of water ($n_{\text{H}_2\text{O}} = 1.333$). The indefiniteness of the refractive index at lower humidities is due to the loss of sensitivity for thin layers⁹⁵. Figure 2.7 on page 31 shows the thicknesses for 6 mol % and 80 mol % lipopolymer plotted against the relative humidity. Variation in thickness can be attributed to the presence of water in the polymer layer. Defining the thickness measured at the lowest relative humidity of 11.3 %RH as a reference, a swelling ratio can be calculated. For the low polymer concentration the uncertainty of the measurement is comparable to the absolute value resulting in high fluctuations. The swelling between 11.3 %RH and 97.6 %RH is by a factor of 3.1–4.7 for 80 mol % PMOx60 which is significantly higher compared to 1.6–1.8 of PMOx30 homopolymers covalently grafted onto the substrate⁹⁶. This difference can be due to different chain lengths and lower lateral density of polymer chains. A complete discussion of the results is post-

Table 2.2 – Relative humidities of saturated salt solutions and resulting osmotic pressures of water at 20 °C. Relative humidities are taken from Greenspan⁹⁸.

Salt	Relative humidity / %	Osmotic pressure / MPa
LiCl	11.31(31)	294
MgCl ₂	33.07(18)	149
NaCl	75.47(14)	38
KCl	85.11(29)	21
KNO ₃	94.62(66)	7.5
K ₂ SO ₄	97.59(53)	3.3

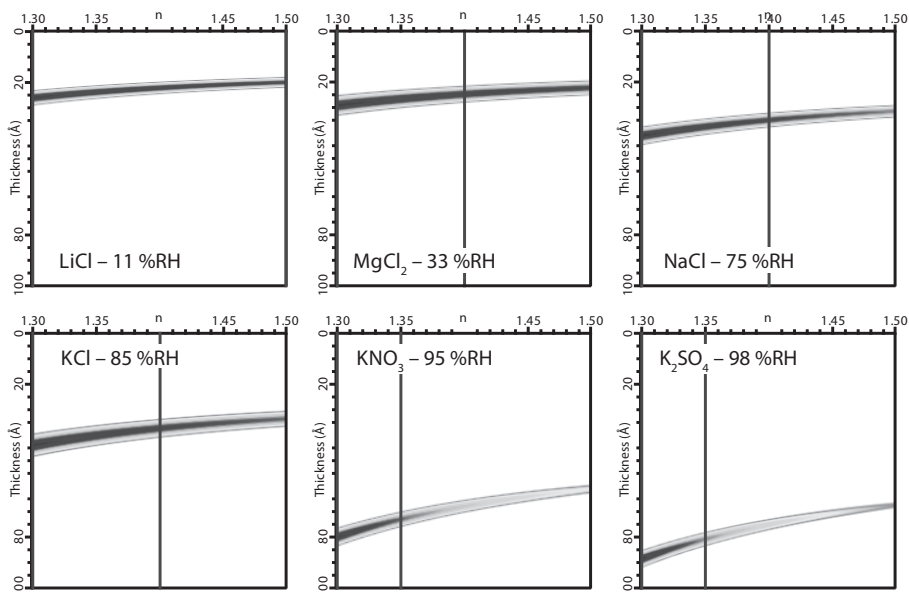


Figure 2.6 – Dependence of the function of merit χ^2 used for assessing the model quality on the refractive index n_{Polymer} and the thickness d_{Polymer} of the polymer interlayer. The sensitivity on the refractive index increases with increasing humidity and layer thickness. The vertical lines denote the area used for obtaining equilibrium distances. The brightness coding indicates the lowest value in black up to two times the minimum value of χ^2 in grey.

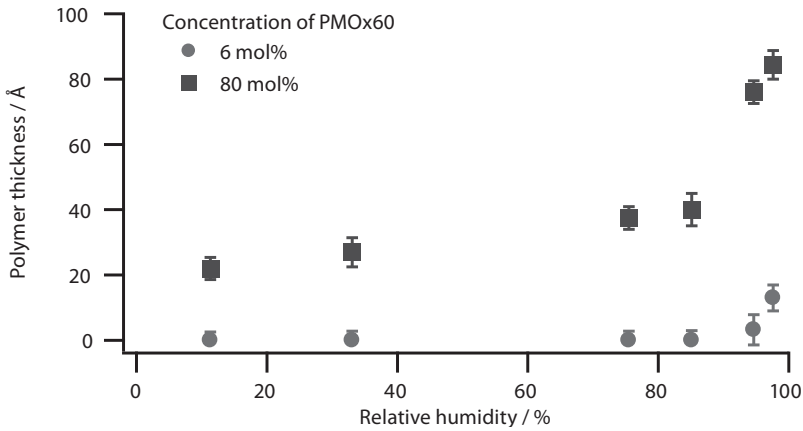


Figure 2.7 – Polymer layer thickness in dependence on the relative humidity measured at 20.0 °C. The thickness of the polymer layer increases by hydration at higher relative humidities.

poned to Section 2.4.1 on page 43 as the inclusion of the results for bilayers under water as a limiting case of vanishing osmotic pressure provide a valuable contribution.

2.2.2 X-Ray Reflectivity

Ellipsometry measurements were confirmed by X-ray reflectivity measurements. Two samples were measured at ambient conditions of about 70 %RH. Clearly visible Kiessig fringes substantiate the homogeneity of the stratified structure of the transferred monolayers. The higher vertical resolution compared to ellipsometry requires the separation of lipid head groups and alkyl chains into distinct layers. To model the data shown in Figure 2.8 on the next page and Figure 2.9 on page 33, a four layer model was used analogous to the model used for ellipsometry measurements but with the lipid layer split into two to account for head groups and alkyl chains separately. The position of the Kiessig fringes in each reflectivity curve defines the overall thickness. Assuming the lipid monolayer remains intact upon the addition of lipopolymer, the change in overall thickness can be attributed to the change in thickness of the polymer layer.

According to the model used for evaluating ellipsometry measurements summarized in Table 2.1 on page 27, first the electron density and thickness of the layer representing the head groups were assumed to be $\rho_{\text{head}} = 13.5 \times 10^{-6} \text{ \AA}^{-2}$ and $d_{\text{head}} = 10 \text{ \AA}$. The values for the layer representing the alkyl chains were $\rho_{\text{chain}} = 7 \times 10^{-6} \text{ \AA}^{-2}$ and $d_{\text{chain}} = 8 \text{ \AA}$. The silicon dioxide was modeled with the same thickness $d_{\text{SiO}_2} = 13.8 \text{ \AA}$ and electron density $\rho_{\text{SiO}_2} = 20 \times 10^{-6} \text{ \AA}^{-2}$ as used for ellipsometry. A lower limit for

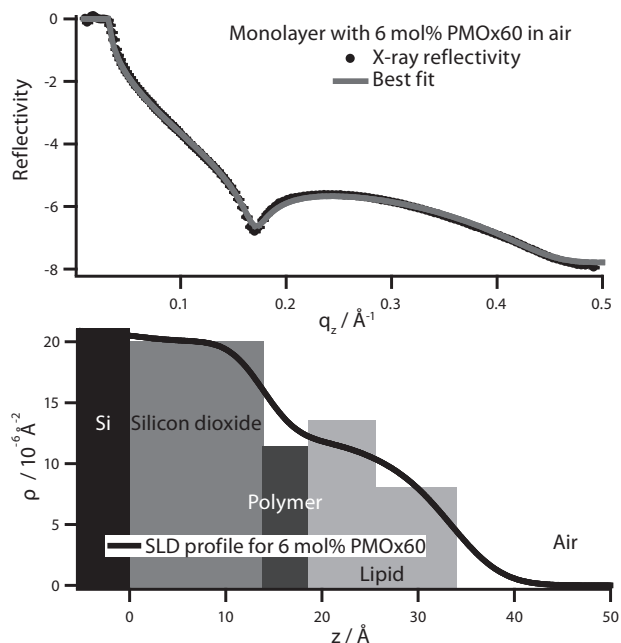


Figure 2.8 – X-ray reflectivity measurement of a monolayer doped with 6 mol % PMOx60 on silicon substrate. **Top:** X-ray reflectivity data and best fitting model. **Bottom:** Scattering length density (SLD) profile of the best fitting model. The bars in the background correspond to the underlying layers of the SLD model.

the roughness between two layers was set to 2\AA . Starting from these values, a reasonable agreement could be achieved with the measured reflectivity curves. The obtained parameters for the polymer layers are summarized in Table 2.3 on the facing page. The scattering length density profiles reconstructed from these parameters are presented in the lower panels in Figure 2.8 and Figure 2.9 on the facing page. At high polymer concentrations the thickness of lipid monolayers was slightly thinner ($\Delta d \approx 3 \text{\AA}$). This is due to the fact that the polymer head group is directly linked to the glycerol junction via a stable ether bond. However, the fit result shows no remarkable change in the scattering length density of the head group layer ($\Delta\rho/\rho < 5\%$) because the scattering length density contrast at the alkyl chain–polymer interface is poorer than that at the alkyl chain–head group interface. Thus, changes in the global shape of the reflectivity curves can mainly be attributed to the polymer layers.

The discussion of the data with varying osmotic pressure is picked up in Section 2.4.1 on page 43. Leaving the variation of osmotic pressure aside, a nontrivial change in lat-

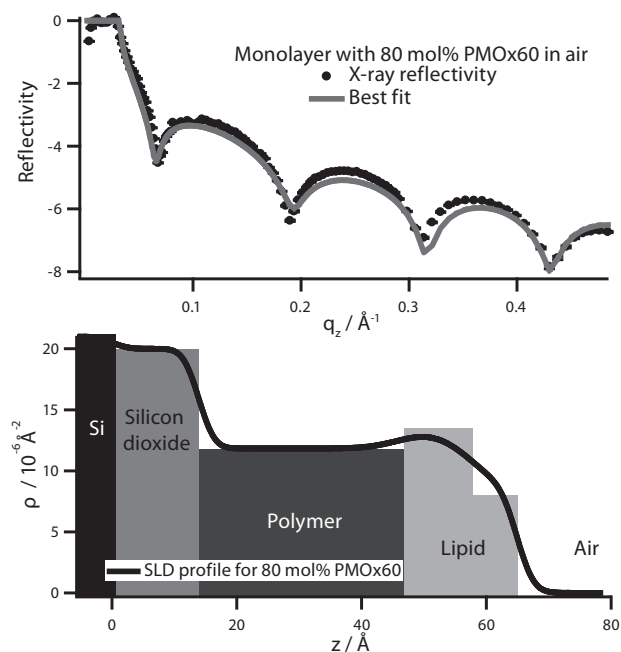


Figure 2.9 – X-ray reflectivity measurement of a monolayer doped with 80 mol % PMOx60 on silicon substrate. **Top:** X-ray reflectivity data and best fitting model. **Bottom:** Scattering length density (SLD) profile of the best fitting model. The bars in the background correspond to the underlying layers of the SLD model.

Table 2.3 – Layer thicknesses obtained from X-ray reflectivity measurements of dry monolayers.

Concentration	$d_{\text{Polymer}} / \text{\AA}$	$\rho_{\text{Polymer}} / 10^{-6} \text{\AA}^{-2}$	$\sigma / \text{\AA}$
6 mol %	4.7	11.5	6.0
80 mol %	32.9	11.8	5.1

eral density of lipopolymers has been found. As a result, the thickness of the polymer layer does not follow a simple linear dependence on the concentration. Based on the presented data the thickness to be expected can be estimated as a function of lipopolymer concentration, number of monomer units and surface pressure during LB transfer. In the following section this will be extended to the biologically more relevant case of lipid bilayers under water.

2.3 BILAYERS AT THE SOLID-LIQUID INTERFACE

2.3.1 X-Ray Reflectivity

Surface Coupling Group

Alternative to the trimethylsiloxane terminated lipopolymers, polymers with a passive end group functionalization were used. A piperidine termination shows no chemical interaction with the substrate and attachment is only via physisorption. The advantage is the stability in the presence of water which leads to polycondensation in the case of trimethylsiloxane. A series of samples was measured using X-ray reflectometry where the distal layer was formed by vesicle fusion on top of a LB transferred monolayer with varying content of a piperidine terminated lipopolymer. The resulting reflectivities are shown in Figure 2.10 on the facing page. With increase of lipopolymer content from bottom to top the features in the reflectivity curves fade away. A three layer model can account for the data where only minor variation in the thickness is necessary. The main change in appearance of the data is accounted for by a change in electron density towards the electron density of water for higher polymer concentrations. The underlying change in surface morphology is expected to be due to the harsh conditions of vesicle fusion. The lack of a chemical surface coupling allows the lipopolymers to rearrange laterally and lose their homogeneity adapted on the air-water interface. As a result the lipopolymers cluster and leave patches of bare substrate. The bare substrate is covered by a lipid bilayer whereas the lipopolymer is hydrated and extends far from the surface. The area fraction of bare substrate diminishes with increasing lipopolymer concentration. The hydrated lipopolymer without a clear boundary to the engulfing water is not distinguishable from water by X-ray reflectivity.

Monomer Length

To elucidate the effect of varying number of monomer units, three lipopolymers with surface coupling group were added at 0.5 mol % concentration to the proximal leaflet. The lipopolymers have 14, 33 or 104 monomer units. As a reference, a sample without lipopolymer consisting only of SOPC was measured. The reflectivity curves in Fig-

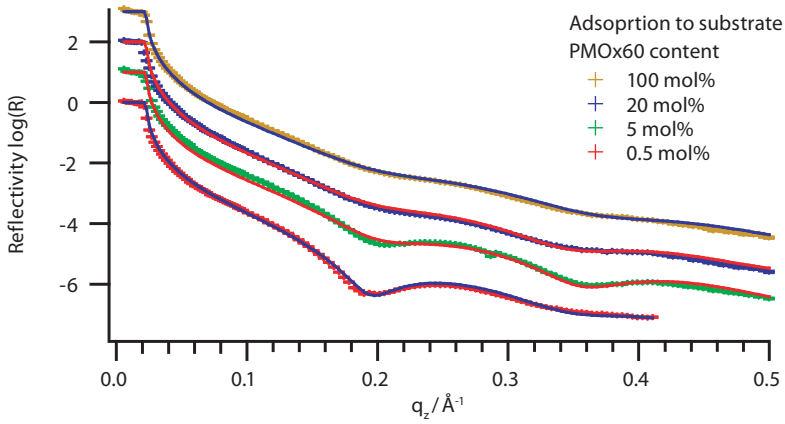


Figure 2.10 – X-ray reflectivity measurements on SOPC bilayers with varying concentration of PMOx60 in the proximal leaflet completed by vesicle fusion. The data is offset successively by one decade to avoid an overlap. Best fits are shown as solid lines.

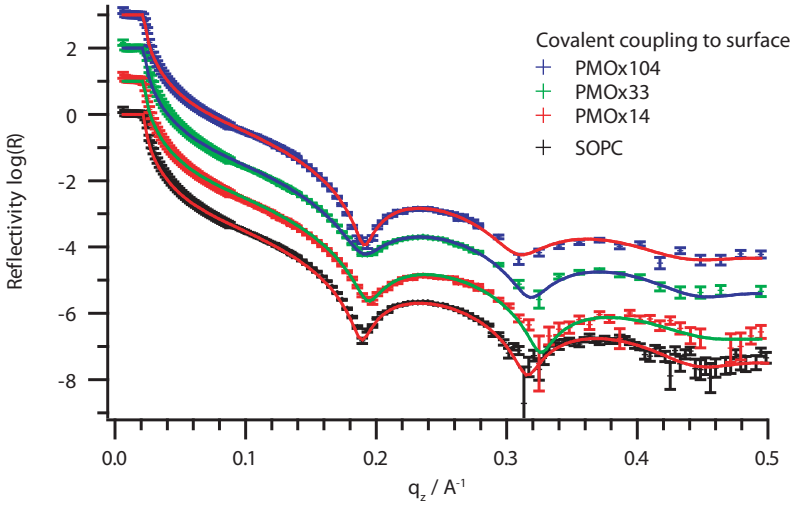


Figure 2.11 – X-ray reflectivity measurements on SOPC bilayers doped with 0.5 mol% lipopolymers of varying number of monomer units in the proximal leaflet. The data is offset successively by one decade to avoid an overlap. Best fits are shown as solid lines.

Table 2.4 – Layers of the model system used to fit the data shown in Figure 2.11 on the previous page. Background was set to 1×10^{-9} . Numbers without errors were fixed, numbers with errors were linked between all reflectivity curves and numbers where a range is given were fitted independently for each sample resulting in the given range.

Layer	$d / \text{Å}$	$\rho / 10^{-6} \text{Å}^{-2}$	$\sigma / \text{Å}$
Water	∞	9.40	
Distal Head group	11.49(105)	11.48(38)	3.01... 4.03
Alkyl Chains	27.85(308)	7.33(12)	4.16... 5.99
Proximal Head group	7.17(1458)	12.75(490)	2.55... 4.46
Polymer	2.00 ... 3.00	9.04 ... 11.00	3.74 ... 6.00
SiO ₂	18.7	8.00(367)	2.78(239)
Si	∞	19.81	2.89(266)

ure 2.11 on the previous page exhibit clear first minima at $q_z \approx 0.18 \text{Å}^{-1}$ and a second at $q_z \approx 0.32 \text{Å}^{-1}$. The position of the minima does not change with the number of monomer units indicating a fixed thickness for all samples. The variations in depth of the minima are not overly pronounced and can be ascribed to variations in sample preparation. The data presented in Figure 2.11 on the preceding page was fitted using a five layer model system and co-fitted with only the parameters related to the polymer layer and the roughnesses above being independent. Parameters of the best co-fitted result are arranged in Table 2.4. Numbers that were held constant during the fitting procedure are given without error, whereas numbers being linked between the datasets but allowed to change are given with an error. Values given as a range show the variation of the unlinked parameters over the four reflectivity curves to achieve best agreement. As can be seen from the ranges of the parameters describing the polymer layer, the variation is small and particularly the thickness shows no significant variation with the number of monomer units. The polymers which are all in the mushroom regime at 0.5 mol % seem to have no effect on the membrane, leaving it unaltered in roughness and separation from the solid substrate. This finding was confirmed by a second measurement series carried out at the ID10b beamline of the ESRF in September 2007.

Lipopolymer Concentration

To extend this picture and get an idea of the role of polymers in these low concentrations we look at a second series of experiments. Here, the concentration of lipopolymer with $n = 104$ was varied from the mushroom regime below approximately 1 mol % deep into the brush regime at 12.2 mol %. The reflectivity curves of these experiments are presented in Figure 2.12 on page 38. While for 0.2 mol % and 3.0 mol % the reflectivity curves take the same shape as seen for the reflectivities presented in Figure 2.11, a qual-

Table 2.5 – Layers of the model system used to fit the data shown in Figure 2.12 on the following page. Background was set to 1×10^{-9} . Numbers without errors were fixed, numbers with errors were linked between all reflectivity curves and numbers where a range is given were fitted independently for each sample resulting in the given range.

Layer	$d / \text{Å}$	$\rho / 10^{-6} \text{Å}^{-2}$	$\sigma / \text{Å}$
Water	∞	9.40	
Distal Head group	10.46(260)	11.70(91)	2.01...7.05
Alkyl Chains	26.93(388)	7.63(8)	3.86...7.21
Proximal Head group	8.71(1009)	11.00(241)	2.01...5.36
Polymer	d_{Polymer}	ρ_{Polymer}	σ_{Polymer}
SiO ₂	18.7	10.54(160)	3.43(86)
Si	∞	19.81	2.00(73)

Table 2.6 – Parameters found for the polymer layer by co-fitting all four reflectivity curves in Figure 2.12 on the next page. The complete model is shown in Table 2.5.

Concentration	$d_{\text{Polymer}} / \text{Å}$	$\rho_{\text{Polymer}} / 10^{-6} \text{Å}^{-2}$	$\sigma_{\text{Polymer}} / \text{Å}$
0.2 mol %	2.62	11.00	2.57
3.0 mol %	2.23	9.96	4.51
12.2 mol %	3.56	9.00	5.99

itative change can be seen at 12.2 mol %. The otherwise clear features are significantly suppressed and the position slightly shifted to lower q_z values. As before, the similarity of the samples enabled the convenient co-fitting with all parameters except for the polymer layer linked. While the change in distance is marginal, the electron density is considerably reduced. At the same time, the roughness of the polymer layer and all subsequent layers above increases. The slight increase in thickness can be taken as a sign of the onset of an increase in thickness with even higher lipopolymer concentrations. But more likely is the lateral rearrangement of the lipopolymers as it has been seen for lipopolymers without surface coupling group. This is supported by the increase in roughness. The surface coupling group can lead to a polycondensation of the lipopolymers in the presence of water. Even if stored appropriately and only for short times, the lipopolymer is eventually immersed into bulk water for compression and transfer on the Langmuir trough. There a higher concentration of lipopolymer enhances the formation of polycondensates. For those polycondensated lipopolymers attachment to the surface of the substrate is, like discussed before, only due to physisorption. As a result, their lateral mobility is kept and under the harsh conditions of vesicle fusion the lipopolymers can rearrange.

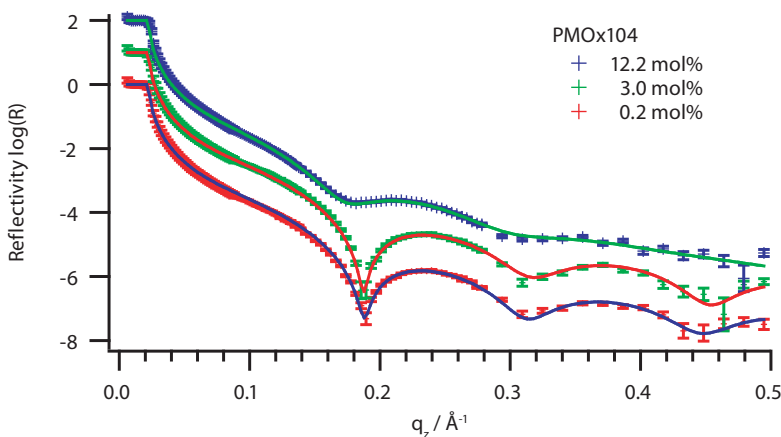


Figure 2.12 – X-ray reflectivity measurements on SOPC bilayers doped with PMOx104 of varying concentration in the proximal leaflet. The data is offset successively by one decade to avoid an overlap. Values of best fits are given in Tables 2.5 and 2.6 and are shown as solid lines.

To avoid the harsh conditions present during vesicle fusion, distal layers can be formed by LS transfer or a second Y-type LB transfer. The combination of this preparation method with X-ray reflectivity has so far not been feasible. A modification of the sample environment where an assembly under water is viable, is a prerequisite.

2.3.2 Ellipsometry

The limitations regarding the sample environment are not present in the case of ellipsometry. In this section a comparison will be made between bilayers formed by vesicle fusion and by LS transfer. As in the case of monolayers examined in Section 2.2.1 on page 26, the parameters for the layer model are obtained by reference measurements. The oxide layer is modeled as before using $n_{\text{SiO}_2} = 1.457$ and $d_{\text{SiO}_2} = 13.8 \text{ \AA}$. For the lipid bilayer a sample prepared only from SOPC was taken as reference. What could be seen already from a detailed analysis of the X-ray measurements on polymer-tethered bilayers in the previous section becomes here apparent in the raw data in yet another way. For a membrane consisting solely of SOPC only a small variation in Ψ and Δ is observed. SOPC is represented by black diamonds in Figure 2.13 on the facing page. With increasing polymer content and also increasing number of monomer units, the measurement results in (Ψ, Δ) pairs spread along a line extending mainly along Δ in the (Ψ, Δ) plane. The poor statistic in terms of spots measured on the samples makes a detailed analysis difficult. Instead the measured data is compared to a simulation of the

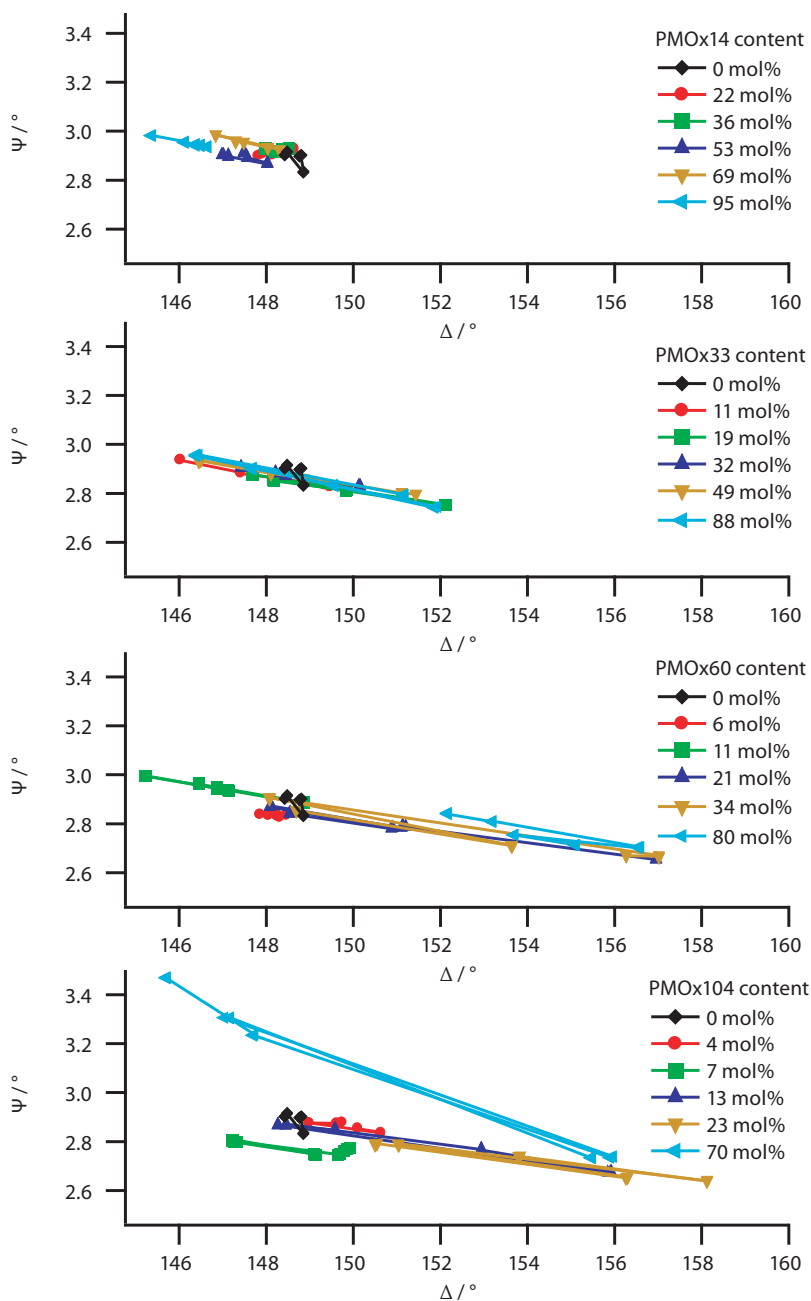


Figure 2.13 – Ψ vs. Δ plots for bilayers with increasing number of monomer units from top to bottom. The concentration of lipopolymer in the proximal leaflet is indicated in the graphs. The bilayer was completed by a LS transfer.

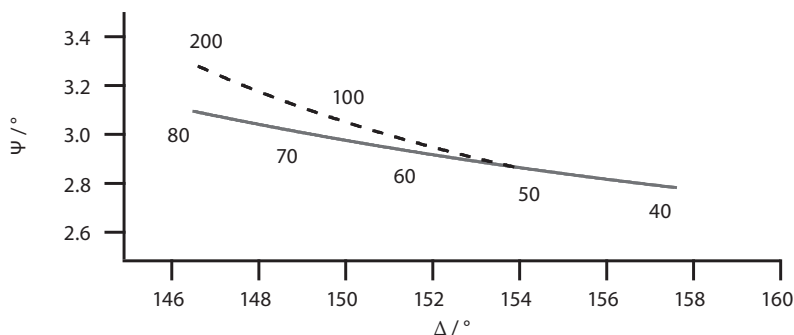


Figure 2.14 – Simulation of Ψ , Δ of a three layer system. Parameters are taken as reported in the previous sections. The solid line shows a variation in bilayer thickness from $d_{\text{Lipid}} = 40 \text{ \AA}$ to $d_{\text{Lipid}} = 80 \text{ \AA}$ with $n_{\text{Lipid}} = 1.44$ and no polymer layer present. The dashed line shows a variation in polymer layer thickness from $d_{\text{Polymer}} = 40 \text{ \AA}$ to $d_{\text{Polymer}} = 200 \text{ \AA}$ with a lipid layer thickness of $d_{\text{Lipid}} = 52.5 \text{ \AA}$.

expected model which allows a qualitative description of the data. Figure 2.14 shows Ψ vs. Δ for a three layer model. The solid line is a variation of the lipid layer thickness in the range $d_{\text{Lipid}} = 40 \text{ \AA}$ – 80 \AA . A second simulation takes a lipid layer thickness of $d_{\text{Lipid}} = 52.5 \text{ \AA}$ and varies the polymer layer thickness from $d_{\text{Polymer}} = 0 \text{ \AA}$ – 200 \AA , shown as dashed line. Comparison of the variation in lipid layer thickness with the experimental data in Figure 2.13 on the preceding page shows good agreement suggesting a lateral heterogeneity of the samples. The apparent thinning of the lipid layer is likely due to an averaging over areas with a complete bilayer and areas filled by hydrated polymer which show almost no contrast to water in terms of refractive index. The small number ≈ 5 of measurements at different spots on the sample does not allow a quantitative analysis in terms of surface coverage. The sample with 70 mol % PMOx104 shows a different behavior which agrees well with the simulation were the polymer layer thickness was varied. While still exhibiting a high heterogeneity, this sample appears to have a complete bilayer as well as the variation being due to undulations in the polymer layer. The width of the fluctuations reaches from a vanishing polymer layer to approximately 200 \AA which is below the length of a single stretched polymer chain of around 300 \AA .

Contrasting the samples where the distal layer was formed by vesicle fusion, Figure 2.15 on the next page shows Ψ vs. Δ measured from a bilayer completed via LS transfer. Three distinct clusters can be seen corresponding to three samples with different concentration of lipopolymer in the proximal leaflet. The small scatter of the data over many spots on the sample provides a good rationale for the lateral homogeneity of the samples. Due to the otherwise identical preparation of the samples this can be

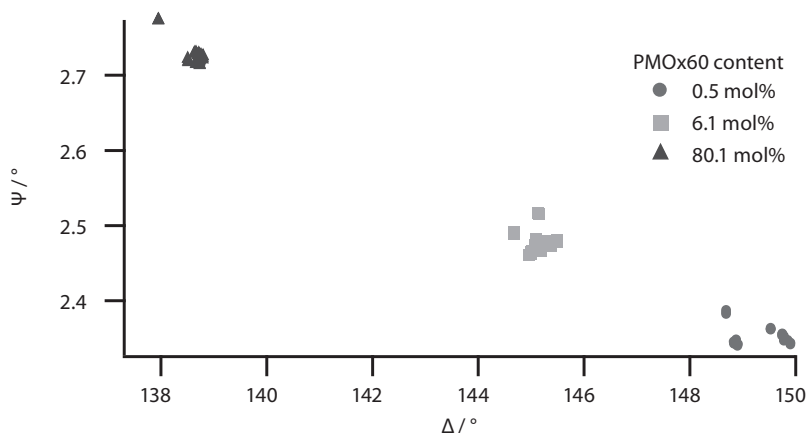


Figure 2.15 – Ψ vs. Δ plot of ellipsometric measurement on bilayer doped with PMOx60 in the proximal leaflet under water on silicon substrate. Completion to a bilayer was done via a LS transfer. Each sample was measured at least at ten different spots. The small scatter of data shows the lateral homogeneity of the bilayer.

accredited to the deposition of the distal leaflet by LS transfer instead of vesicle fusion. The result of an analysis with a three layer model for the polymer layer thickness is presented in Table 2.7. For 0.5 mol % no difference to the reference measurement on a bilayer of SOPC could be found, leading to an undetectable polymer layer thickness and an undefined refractive index. For the high lipopolymer fractions of 6 mol % and 80 mol %, an increase in polymer layer thickness was observed by a factor of 7–10 upon complete hydration. This swelling ratio is significantly higher compared to the ratio found for swelling of 80 mol % in an atmosphere with 98 %RH of about 3.1–4.7 as discussed in Section 2.2.1 on page 26.

A further proof of the homogeneity of the samples is given by fluorescence mi-

Table 2.7 – Layer thicknesses and refractive indices obtained from ellipsometry measurements for bilayers under water. For the lowest polymer concentration a two layer model is sufficient corresponding to a vanishing polymer layer thickness and a therefore undefined refractive index.

Concentration	$d_{\text{polymer}} / \text{\AA}$	n_{polymer}
0.5 mol %	0	-
6 mol %	69(13)	1.340(2)
80 mol %	176(18)	1.348(2)

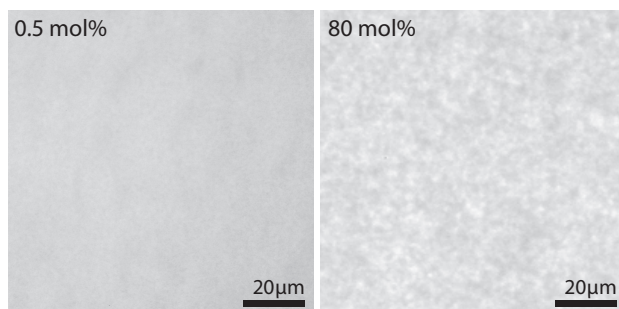


Figure 2.16 – Fluorescence micrograph of PMOx60 doped bilayer under water. TexasRed-DHPE was used as a fluorescent marker in the proximal layer with a concentration of 0.2 mol %. The distal layer was formed by LS transfer of SOPC. On the left side a detail is shown for 0.5 mol % doping ratio and on the right side for 80 mol % polymer content in the proximal layer.

scopy. This is also a validation for the applicability of the reflectivity based techniques which rely on stratified structures. LB films on glass cover slides were completed to bilayers by a LS transfer of SOPC with 0.2 mol % of fluorescently labeled lipids TexasRed-DHPE. Two representative micrographs are presented in Figure 2.16. The homogeneous distribution of fluorescent label purports the lateral homogeneity of the other membrane constituents.

2.4 DISCUSSION

Summarizing the experiments regarding the structure of polymer-tethered membranes normal to the membrane it can be concluded that the use of a LS transfer for the distal layer is necessary for lipopolymers without a surface coupling group as in the case of PMOx60 which possesses a piperidine termination. For these lipopolymers the completion via vesicle fusion results in a reorganization of the polymer and loss of lateral homogeneity. In the presence of a surface coupling group this lateral reorganization should be impossible. For low lipopolymer concentrations of 0.5 mol % the effect of a lateral reorganization is not visible and can therefore not be assessed from the experiments presented. At concentrations of lipopolymer in the brush regime a lateral reorganization is clearly seen in both, X-ray reflectivity and ellipsometry measurements. This is likely due to the loss of surface coupling groups which are engaged in the polycondensation. For polycondensation to occur water has to be present. To avoid this, strict storage and handling in water free solvents and atmospheres has to be ensured. Due to the ever present water in chloroform used as a solvent, an inevitable aging pro-

cess leading to a irreversible degradation of the lipopolymer occurs. Even if freshly synthesized lipopolymer is used and handled appropriately, the LB transfer makes the contact with bulk water unavoidable. Especially in high concentrations the possibility of polycondensation is high and may be sufficient to cause the observed deactivation of the surface coupling group.

These difficulties can be overcome by the use of a different surface coupling group. Including an activation barrier for the coupling ensures the non-reactivity before the transfer is completed. The activation energy can take the form of a photoactivation or the requirement of a certain chemical environment like a defined pH. The synthesis of the lipopolymer is specifically advantageous for such variations in the choice of termination^{59,99,100}.

2.4.1 Interfacial Forces

In the following section selected results from the previously discussed experiments are combined to gain a deeper insight into the interactions taking place on the solid support. The thicknesses of the polymer layer presented in Figure 2.7 on page 31 are shown again but this time on the ordinate axis versus the osmotic pressure corresponding to the relative humidity in Figure 2.17 on page 46. Under bulk water the osmotic pressure on the sample vanishes and the equilibrium thickness of the corresponding bilayer measurement is included at the lowest displayed pressure. The equilibrium distances have to be the result of a balance of all interfacial forces. We consider four important contributors

1. osmotic pressure,
2. van der Waals interaction,
3. hydration repulsion and
4. undulation repulsion.

An electrostatic contribution is not considered as the lipopolymers are neutral and the phospholipids are zwitterionic⁸⁹. The osmotic pressure is used as regulator and counterbalances the other three. At the equilibrium distance d_{equil} the following has to be satisfied

$$\Pi_{\text{Osmotic}}(rh) = \Pi_{\text{vdW}} + \Pi_{\text{Hydration}} + \Pi_{\text{Undulation}}. \quad (2.1)$$

Except for the osmotic pressure, which is a function of the relative humidity, the components are parametrized by the distance to the solid substrate.

Osmotic Pressure

The osmotic pressure is given by

$$\Pi_{\text{Osmotic}} = -\frac{k_b T}{V_{\text{H}_2\text{O}}} \ln \left(\frac{rh}{rh_{\text{H}_2\text{O}}} \right) \quad (2.2)$$

where k_b is the Boltzmann constant and T the temperature in Kelvin. $V_{\text{H}_2\text{O}} = 29.9 \text{ \AA}^3$ is the volume of one water molecule and rh the relative humidity with $rh_{\text{H}_2\text{O}} = 100 \%$ ⁹⁷.

van der Waals

The van der Waals pressure is calculated on the basis of a five layer model. Layer one and two are the bulk crystalline silicon and silicon dioxide (thickness T_1), respectively. Layer three consists of the polymer spacer, layer four is the lipid membrane with thickness T_2 and layer five is either air (monolayer) or water (bilayer). The van der Waals pressure for a five layer model is approximated by

$$\Pi_{\text{vdW}}(d) = \frac{1}{6\pi} \left(\frac{A_{234}}{d^3} - \frac{\sqrt{A_{121}A_{343}}}{(d+T_1)^3} - \frac{\sqrt{A_{545}A_{323}}}{(d+T_2)^3} - \frac{\sqrt{A_{545}A_{121}}}{(d+T_1+T_2)^3} \right) \quad (2.3)$$

given by Israelachvili¹⁰¹. The Hamaker constants A_{xyz} are listed in Table 2.8 on the next page. A_{xyz} denotes the Hamaker constant of medium x interacting with medium z through medium y . Except for A_{234} all Hamaker constants were calculated from material properties. A_{234} was calculated using the combining relation

$$A_{234} = \left(\sqrt{A_{2\nu 2}} - \sqrt{A_{3\nu 3}} \right) \left(\sqrt{A_{4\nu 4}} - \sqrt{A_{3\nu 3}} \right)$$

where ν denotes the interaction across vacuum¹⁰¹.

Hydration Repulsion

The hydration repulsion due to the swelling of polymer chains can be modeled by an exponential decay with the distance

$$\Pi_{\text{Hydration}}(d) = \Pi_o \exp \left(-\frac{d}{\lambda} \right) \quad (2.4)$$

parametrized by a pressure constant Π_o and a decay constant λ ¹⁰². The values for Π_o and λ are extracted from the force–distance relationships, which were obtained by measuring the equilibrium thicknesses of the polymer layer at different osmotic pressures.

Table 2.8 – Hamaker constants used in the asymmetric five layer model. A_{xyz} denotes the Hamaker constant of medium x interacting with medium z through medium y . For the bilayer covered polymer film under water the polymer layer ($3'$) was modeled as water, as the content of water is high.

Hamaker constant / J	Media ($x/y/z$)	Name
5.99×10^{-19}	Si/SiO ₂ /Si	A_{121}
2.79×10^{-21}	Polymer/Lipid/Polymer	A_{343}
1.40×10^{-19}	Air/Lipid/Air	A_{545}
1.87×10^{-21}	SiO ₂ /Polymer/Lipid	A_{234}
1.73×10^{-21}	Polymer/SiO ₂ /Polymer	A_{323}
5.93×10^{-21}	Polymer/Lipid/Polymer	$A_{3'43'}$
5.93×10^{-21}	Water/Lipid/Water	$A_{5'45'}$
6.21×10^{-21}	SiO ₂ /Water/Lipid	$A_{23'4}$
7.95×10^{-21}	Polymer/SiO ₂ /Polymer	$A_{3'23'}$

Undulation Repulsion

The undulation pressure according to Helfrich is calculated using

$$\Pi_{\text{Undulation}}(d) = \frac{2N}{N+1} \alpha_N \frac{(k_b T)^2}{\kappa d^3} \quad (2.5)$$

for $N = 1$ membrane and $\alpha_1 = \frac{\pi^2}{128}$ as predicted by Bachmann *et al.*¹⁰³. Where k_b is the Boltzmann constant, T the temperature and κ the bending rigidity of the membrane. The bending rigidity for SOPC is taken as $\kappa = 1.2 \times 10^{-19} \text{ J}^{104}$.

In Figure 2.17 on the following page, each of the three interfacial pressures and their sum are plotted versus the thickness of polymer interlayers d_{polymer} for polymer concentrations of 6 mol % and 80 mol %. In both panels, the data points from the experimentally determined force–distance relationships are plotted as green (respectively blue) symbols, which can be fitted with exponential functions in the hydration repulsion regime. Data points above $5 \times 10^7 \text{ Pa}$ were not included in the fit, since the force–distance relationship in such a high pressure regime is governed by steric repulsion due to the finite compressibility of the polymer chains. As indicated by the shaded areas, the exponential fits of the measured data points yielded the characteristic parameters for each polymer fraction; $\Pi_0 = 2.1 \times 10^7 \text{ Pa}$ – $2.2 \times 10^7 \text{ Pa}$ and $\lambda = 4.8 \text{ \AA}$ – 7.0 \AA for 6 mol % and $\Pi_0 = 32.5 \times 10^7 \text{ Pa}$ – $43.2 \times 10^7 \text{ Pa}$ and $\lambda = 15.2 \text{ \AA}$ – 17.2 \AA for 80 mol %. At the lipopolymer fraction of 6 mol %, the extrapolation of the sum of aforementioned three pressures to zero predicts the equilibrium distance of about 30 \AA – 100 \AA , which shows good agreement with the polymer layer thickness obtained by ellipsometry (Table 2.7

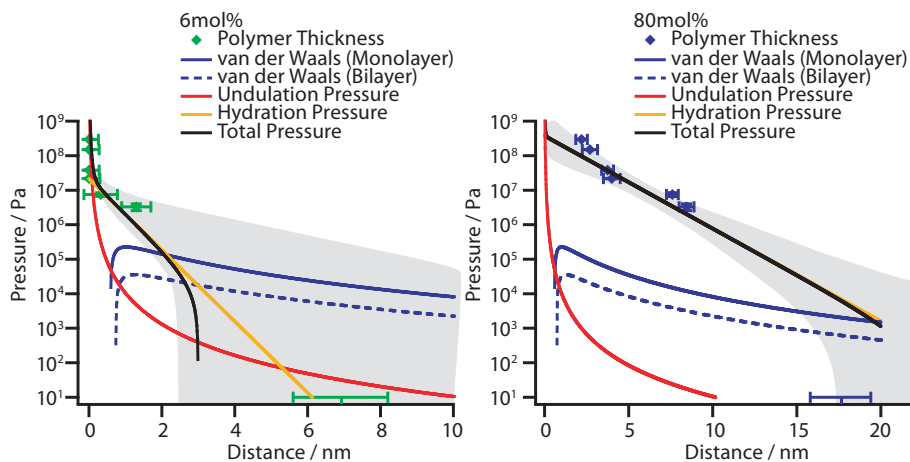


Figure 2.17 – Polymer layer thickness measured at different osmotic pressures for 0.5 mol % PMOx60 (left panel) and 80 mol % PMOx60 (right panel). The contributions to the total pressure (black) are the attractive van der Waals pressure (blue), the undulation pressure (red) and the hydration pressure (yellow and shaded area). The van der Waals pressure is displayed with opposite sign to make a comparison possible. The polymer thickness for the bilayer under water is shown as a line above the ordinate axis.

on page 41). As presented in Figure 2.17, the scatter of the data points at higher humidity is more pronounced at the lipopolymer fraction of 80 mol %. The range of the equilibrium thickness calculated for the zero pressure condition is around 21 nm showing the experimentally determined equilibrium polymer thickness ($176 \text{ \AA} \pm 18 \text{ \AA}$) to be limited by the stretched polymer length ($\approx 180 \text{ \AA}$). Apart from this limit this calculation suggests that the equilibrium thickness of the membrane–substrate distance maintained by the polymer spacers can quantitatively be explained in terms of the interplay of the major interfacial forces presented here.

2.4.2 Polymer Volume

One of the advantages of the successive deposition of the monolayers into a membrane is the capability to precisely control the lateral density of lipopolymer tethers in asymmetric membranes. Here, the volume occupied by one polymer chain can be calculated from the lateral density of polymer chains and the experimentally determined polymer layer thickness. Since such a calculation becomes erroneous at lower lipopolymer fractions where the errors in the layer thickness are comparable to the absolute values, we focus in the discussion on the case of the highest lipopolymer content of 80 mol %. The area per polymer chain at a lateral pressure of $\Pi = 30 \text{ mN m}^{-1}$ can be obtained from the pressure–area isotherm in Figure 2.2 on page 25 to be $A_{\text{Polymer}} = 166 \text{ \AA}^2$. Taking the polymer layer thickness from X–ray reflectivity in an ambient atmosphere, $d_{\text{Refl}} = 32.9 \text{ \AA}$, the corresponding chain volume $V_{\text{Exp/Ell}} = 5461 \text{ \AA}^3$ can be calculated.

In order to estimate the volume fraction of hydrating water, the volumes obtained by experiments were compared to the volume predicted by the calculation method proposed by Connolly¹⁰⁵. Using a probe radius of 1.4 \AA for water, the excluded volume of one dry poly(2-methyl-2-oxazoline) chain with 60 monomers can be calculated to be $V_{\text{Connolly}} = 5140 \text{ \AA}^3$. Comparison with the experimental chain volume at 85 %RH suggests that the volume increases by 6 % due to the uptake of water. However, the calculation of polymer chain volume fails under dry conditions. For example, the chain volume calculated from the thickness measured by ellipsometry at 11.3 %RH, $V_{\text{Exp/Ell}} = 3652 \text{ \AA}^3$, is much smaller than V_{Connolly} . This discrepancy suggests that the polymer layer thickness is underestimated in the used slab model. One possible scenario would be that polymer chains are partially immersed into the layer representing the head groups of phospholipids. This actually seems reasonable since polymer chains are directly connected to the glycerol junction via ether bonds. In fact, if one assumes that approximately 80 % of the head group layer with a thickness of 11 \AA is filled with polymers, the expected volume of 1461 \AA^3 agrees very well with the difference $V_{\text{Connolly}} - V_{\text{Exp/Ell}} = 1488 \text{ \AA}^3$.

After the deposition of the distal monolayer, the polymer layer, now under bulk water, becomes thicker by a factor of 6 ($d_{\text{Exp/Ell}} = 176 \text{ \AA}$). This corresponds to $V_{\text{Exp/Ell}} =$

$29\,216 \text{ \AA}^3$. Here, the influence of the polymers immersed in the head group layer on the entire volume of polymer is merely 5 %, and we obtain the volume fraction of water, $\Phi_{\text{H}_2\text{O}/\text{EIL}} = 82 \%$ ($\frac{5140}{29216} \approx 0.18$). This value is larger than those reported for a supported membrane tethered with short hexa(ethyleneoxide) spacers using neutron reflectivity; $\Phi_{\text{H}_2\text{O}/\text{Neutron}} = 4 \%$ for membranes with 100 mol % tethers, and 50 %–60 % for 50 mol % tethers.³⁹ A distinct difference in the degrees of hydration suggests that longer poly(2-oxazoline) head groups can uptake more water than oligo(ethylene oxide) head groups possessing much less conformational degrees of freedom^{46,100}.

2.5 *IN SITU* CONTROL USING SWITCHABLE POLYMERS

The present membrane model can be further tailored by the choice of polymer. The living ionic ring-opening polymerization⁶⁷ allows many variations in the preparation of polymers. So far the side group of the polymers was methyl but larger side groups can be taken. Apart from polymers with identical monomer units, a statistical mixture of different monomers can be copolymerized by which an extreme fine tuning of the desired properties can be achieved. Making the polymer switchable from a loose state, in which it occupies a large volume to a compact state where the solvent is expelled, the thickness of the polymer layer can be actively switched. There are several properties in question which are interesting to trigger such a change in conformation. Among them are the pH of the surrounding, irradiation by light and temperature. In the following we will focus on a change induced by temperature. As a cause for the switching the presence of a lower critical solution temperature (LCST) in the polymer is utilized. Below the LCST, the polymer is mixed with the solvent occupying a volume larger than its molecular volume. Increasing the temperature above the LCST results in a demixing of polymer and solvent, as the mixture is in the spinodal regime. For the present lipopolymers this transition can be visualized in bulk solutions by measuring the cloud point with temperature¹⁰⁶. The transition in three dimensions occurs in a narrow temperature range justifying the view as a binary switch. In order to induce a variation in polymer layer thickness in a polymer-tethered membrane, this effect has to be present in the two dimensional geometry and has to be strong enough to overcome the the resistance of the other interfacial forces as discussed in Section 2.4.1 on page 43.

First the isotherms of a poly(2-isopropyl-2-oxazoline) lipopolymer, RIM-291 were recorded. The chemical structure is shown below the isotherms in Figure 2.18 on the facing page. Below the LCST the polymer should be hydrophilic and in the water phase. When heated above the LCST the compaction and removal of water is expected to drive the polymer towards the air-water interface. Along with this a significant increase in surface pressure is expected. Isotherms above and below the LCST of a monolayer of RIM-291 corrected for the change in surface tension of water show no major deviations from each other. In Figure 2.18 on the next page isotherms are only presented up to a

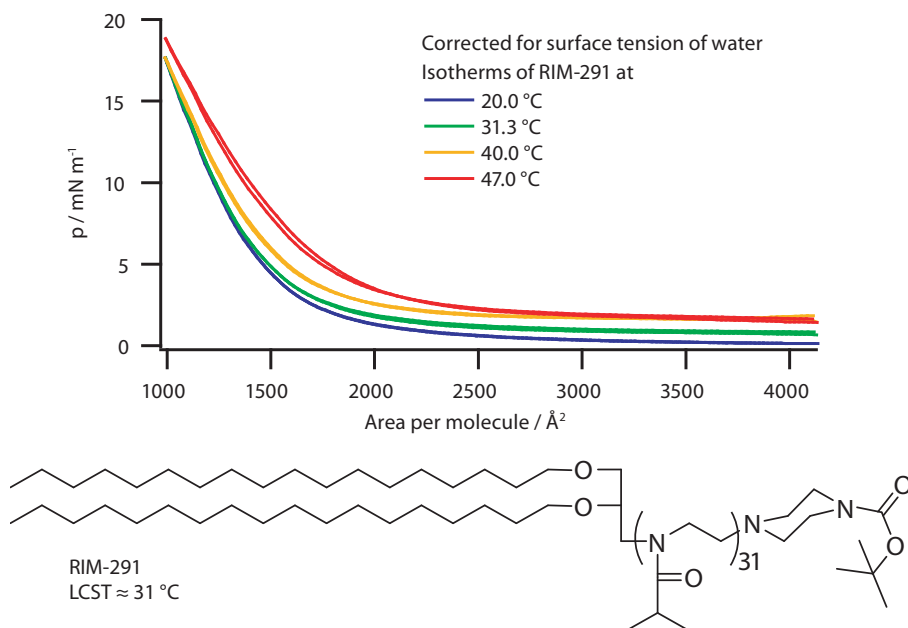


Figure 2.18 – Top: Isotherms of RIM-291 at temperatures below and above the LCST ≈ 31 °C. **Bottom:** Chemical structure of the lipopolymer RIM-291 with isopropyl side group.

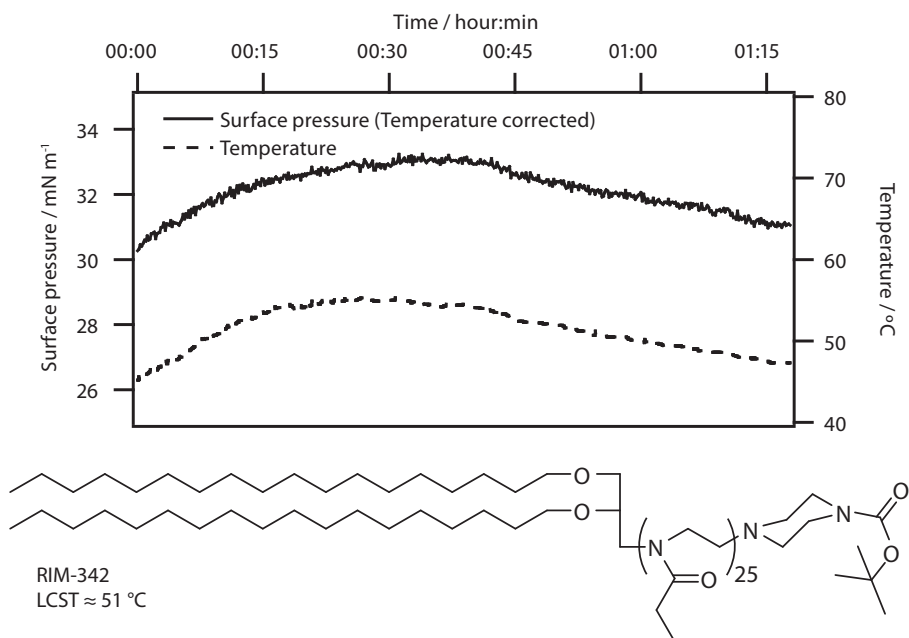


Figure 2.19 – Top: Isochore of RIM-342. The temperature is indicated by dashed red line scaled by the axis on the right side. The blue solid line shows the surface pressure. **Bottom:** Chemical structure of the lipopolymer RIM-342.

surface pressure of $\approx 18 \text{ mN m}^{-1}$ as above this pressure lipopolymers are lost irreversibly to the subphase. At pressures below 18 mN m^{-1} the area per molecule is more than one order of magnitude larger than expected for phospholipids. This indicates the presence of polymer at the air–water interface even below the LCST. Consequently, water is not a good solvent for the polymer with 2-isopropyl side group.

In order to get stable monolayers up to high surface pressures at the air–water interface which have a distinct layer of alkyl chains, a less hydrophobic polymer chain has to be used. To make the polymer more hydrophilic, the 2-isopropyl side group was replaced by an ethyl side group. This has the additional effect of a shift of the LCST to higher temperatures. With $n = 25$ monomer units the temperature rises to $T_{\text{LCST}} = 51 \text{ }^\circ\text{C}$. In Figure 2.19 a pressure isochore of a lipopolymer with ethyl side group is displayed. The pressure is corrected for the variation of water surface tension with temperature. The pressure changes continuously proportional to the temperature as expected for a fixed area per molecule. The clear effect of the LCST seen in a bulk solution of this lipopolymer could not be observed here. A more direct approach is the

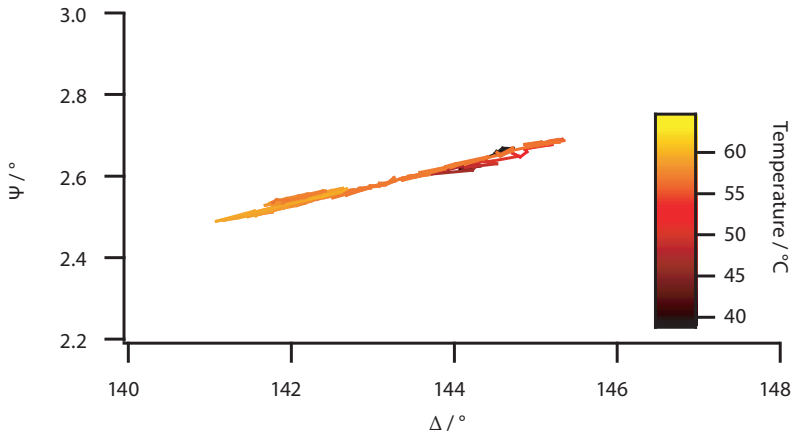


Figure 2.20 – Ψ vs. Δ plot measured on a bilayer under water. The proximal layer consists of 100 mol % RIM-342 transferred by LB, the distal layer is SOPC transferred by LS. The LCST is expected at 51 °C.

measurement of the polymer layer thickness below a lipid bilayer on a solid support. A monolayer consisting of RIM-342 transferred via LB transfer onto a silicon substrate was completed to a bilayer via LS transfer of a SOPC monolayer. This sample was measured using ellipsometry in a temperature range 20 °C–64 °C. Figure 2.20 shows the Ψ vs. Δ graph of the measurement with temperature encoded by color in the range 40 °C–64 °C. Only a small variation in ellipsometric angles can be observed with no clear trend regarding temperature. The analysis is complicated by the temperature dependent variation in refractive index of the bulk water covering the polymer–tethered bilayer. With a thinning of the polymer layer an increase in the refractive index is expected. These two effects counteract each other minimizing the contrast in ellipsometry. From the present data it is therefore not possible to discriminate between fluctuations occurring during the time required for measurement of about 1 h or an actual sudden change in polymer layer thickness. The reduction in contrast due to two counteracting effects applies likewise to X-ray reflectivity. As a resort to get information about the thickness change of the polymer layer a macroscopic probe can be used. Ishida & Kobayashi¹⁰⁷ used a colloidal probe coupled to an atomic force microscope to measure the force distance curves on a LCST polymer covered substrate. A simpler approach is the use of colloidal particles with reflection interference contrast microscopy where the interference pattern of the probe with the substrate will vary according to their separation. Depending on the analysis method a resolution down to ≈ 2 Å can be achieved¹⁰⁸.

2.6 CONCLUSION

In this chapter the transversal membrane structure and substrate–membrane interactions were investigated. This was done using lipopolymers forming a soft interlayer between solid support and membrane. The lipopolymers have a narrow size distribution making them suitable for accurately controlled spacing. The polymer–tethered membranes were prepared by LB transfer of lipid–lipopolymer mixtures from the air–water interface. Completion to a bilayer proceeded either by vesicle fusion or LS transfer. The combination of different reflectivity techniques presented here, X–ray reflectivity and ellipsometry as well as neutron reflectivity (in Appendix B), leads to a detailed picture of the polymer–tethered membranes.

The presence of a surface coupling group was shown to be vital to avoid a lateral rearrangement of the lipopolymers in the case of vesicle fusion. In the case of completion via LS transfer the physisorption of the lipopolymer to the surface is sufficient. For small concentrations the polymer layer cannot be resolved with the experimental techniques. For a monolayer with 70 mol % PMOx104 the polymer layer thickness reaches $46 \text{ \AA} \pm 1 \text{ \AA}$. It was shown that the thickness of the polymer interlayer increases with increasing polymer length and polymer concentration. This increase is non–linear due to an increase in area per molecule with increasing lipopolymer concentration. A clear dependency of the polymer layer thickness on the humidity was observed. From the combined data, the thickness to be expected can be estimated as a function of lipopolymer concentration, number of monomer units and surface pressure during LB transfer. Calculation of the van der Waals interaction from material parameters and the contribution of the undulation repulsion allowed the estimation of the hydration forces present in the polymer interlayer. The results obtained predict the equilibrium thickness of a complete bilayer under water with reasonable agreement. For 80 mol % PMOx60 the distance measured amounts to $176 \text{ \AA} \pm 18 \text{ \AA}$ which will be sufficient as a spacing even for large protein domains protruding from the membrane. Furthermore, the knowledge of the lateral density and thickness of the polymer interlayer allows the estimation of the volume fraction of hydrating water. For 80 mol % PMOx60 this yields a volume fraction of 82 % filled with hydrating water. This shows that the lipopolymers used are suitable for creating a soft interlayer with tunable properties.

CHAPTER 3

LATERAL STRUCTURE OF LIPOPOLYMER LAYERS

During the preparation of polymer-tethered membranes a phase separation can be observed. While the mixture of lipids and lipopolymers is homogeneously mixed at the air-water interface of the Langmuir trough, the LB transfer can induce a phase separation of the two constituents. The dissociation occurs steadily and results in stripes enriched in lipopolymer separated by stripes with an enrichment in lipid. In this chapter the main focus is on the quantitative control of this pattern formation. The dependencies on transfer speed, subphase viscosity as well as on dipping angle were determined experimentally. Furthermore a detailed picture of the three-phase contact line region has been obtained providing the frame for further theoretical considerations. A few qualitative effects of the structuring have already been studied. There, the chemical structure was varied to exclude condensation effects of the lipid anchor and to assess the influence of the polymer^{46,63}. By changing the lipid anchor from Di-stearyl ($2 \times C_{18:o}$) to Di-phytanyl ($2 \times 4ME C_{16:o}$) the phase separation of the alkyl chains can be excluded as the driving force for the pattern formation. Substitution of the trimethoxysilane coupling group by a piperidine termination did not alter the observed patterns. An increase in polymer length resulted in a lower contrast of the stripe patterns as well as an increase in the number of branches. However, the mean stripe distance remained unchanged. Substitution of the polymer backbone by ethylene glycol and the addition of a phosphoethanolamine group resulted in a still structured yet much less well defined pattern.

The preparation of monolayers using the LB transfer technique offers several unique advantages, especially the precise control of many relevant parameters opens the way

to study underlying phenomena. In the following chapter we will focus on the lateral structures formed by transferring a mixture of lipopolymers embedded in a lipid matrix. Using fluorescence microscopy the phase separation between lipopolymers and lipids on the transferred film can be observed as the fluorescent marker is preferentially embedded in one of the phases. Along the direction of transfer stripes with a characteristic mean distance are formed. The continuity of these stripes extends over the complete substrate length of several cm. Parameters influencing the stripe to stripe distance were found to be transfer speed and viscosity of the subphase. Their dependence is shown in detail in the following sections. The origin of the structure formation can be narrowed down to occur in the meniscus region as the mixture shows no sign of separation on the air–water interface of the Langmuir trough over the whole pressure range where a stable monolayer is formed.

3.1 QUANTITATIVE DEPENDENCE ON PREPARATION PARAMETERS

To quantify the impact on the separation process three well controllable parameters were varied over the experimentally accessible range. The three parameters are transfer speed v , subphase viscosity μ and the dipping angle Ω . The experimental geometry with the parameters indicated is shown in Figure 3.1 on the facing page. Stripe patterns were analyzed for all conditions and are presented in the following sections.

Determination of Stripe Distances To determine the average stripe to stripe distance from the fluorescence images, an intensity line profile perpendicular to the stripes was extracted. A profile length of approximately $140\ \mu\text{m}$ was used. The maxima on this profile were selected manually and their lateral position plotted against the peak number. A line was fitted to the lateral position data whose slope gives the average stripe to stripe distance. The deviation of the measured maxima from an equidistant pattern with this determined distance is shown as error bar in the graphs showing stripe distances. The contrast in the fluorescence micrographs was determined with respect to a background value taken at one corner of the micrograph outside of the illuminated area. The contrast ratio is defined as

$$\left(\frac{\text{MAX} - \text{BASE}}{\text{MIN} - \text{BASE}} \right) : \left(\frac{\text{MIN} - \text{BASE}}{\text{MIN} - \text{BASE}} \equiv 1 \right) \quad (3.1)$$

where BASE is the background intensity value and MAX is the intensity recorded at the center of a stripe whereas MIN is the minimum intensity between two stripes.

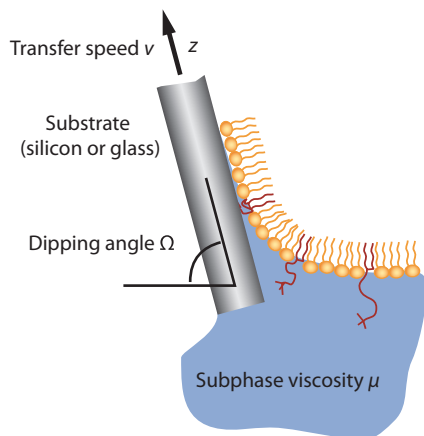


Figure 3.1 – Schematic view of the LB transfer indicating the parameters varied for stripe pattern formation. The lipid–lipopolymer mixture forms a homogeneous monolayer on the subphase–superphase interface and is transferred onto the substrate during slow removal with transfer speed v . The substrate is immersed at a dipping angle Ω into the subphase. The subphase viscosity μ is controlled via composition and/or temperature.

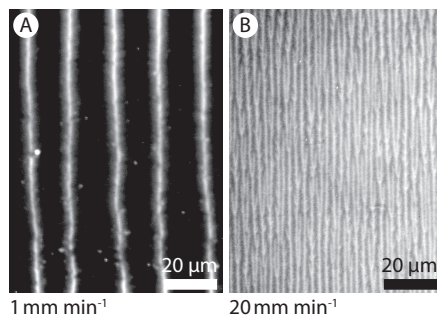


Figure 3.2 – Fluorescence images from transfers at different speeds. The transfer direction is to the top. **A)** A high contrast and widely spaced, equidistant stripes are observed for $v = 1 \text{ mm min}^{-1}$. **B)** A low contrast and small spaced stripes yet highly regular are observed for $v = 20 \text{ mm min}^{-1}$.

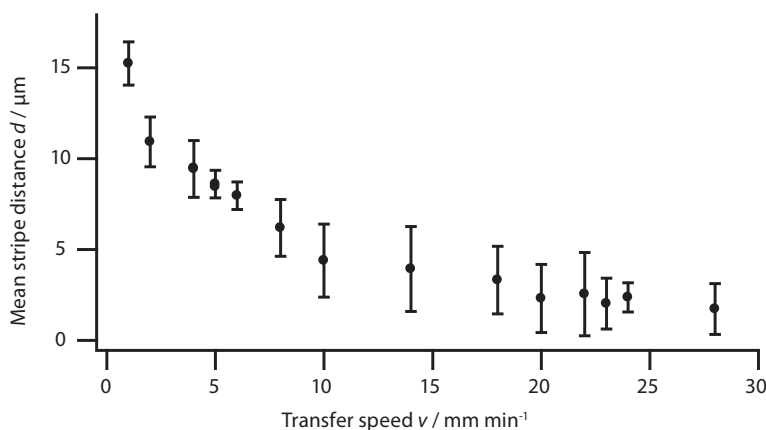


Figure 3.3 – Stripe to stripe distance d as a function of transfer speed v . Above $v = 30 \text{ mm min}^{-1}$ stripe patterns are not discernible by fluorescence microscopy as the contrast is too low. Error bars show the standard deviation from a regular pattern with stripe distance d .

3.1.1 Transfer Speed

Transfer speed v was varied from 1 mm min^{-1} to beyond 30 mm min^{-1} . As can be seen from the fluorescence micrographs taken from samples transferred at 1 mm min^{-1} and 20 mm min^{-1} , shown in Figure 3.2 on the previous page, not only the stripe distance diminishes with increasing speed but also the contrast. Along the direction of transfer the emergence of new stripes can be observed. To recover the equilibrium distance two stripes will merge shortly after. The frequency of the emergence and merging events increases with the increase of transfer speed. In Figure 3.3 data up to 28 mm min^{-1} is shown since for faster transfer speeds no pattern could be perceived in the fluorescence micrographs. As subphase purified water with a viscosity of approximately 1 mPa s was used. The dipping angle was $\Omega = 90^\circ$ which is the commonly used geometry for LB transfers. Below 5 mm min^{-1} stripe pattern formation appears to be sensible to vibrations which lead to stripe distances close to the value obtained for 5 mm min^{-1} . In Figure 3.3 only transfers not suffering from vibrations are shown.

3.1.2 Subphase Viscosity

Variation of subphase viscosity μ was accomplished by mixing purified water with glycerol¹⁰⁹. Starting from $\mu = 1.005 \text{ mPa s}$ for purified water at 20°C the subphase viscosity was increased up to $\mu = 3.72 \text{ mPa s}$ for a mixture with 40% weight glycerol. For high subphase viscosities above $\mu = 2.5 \text{ mPa s}$ the contrast was too low to recognize stripe

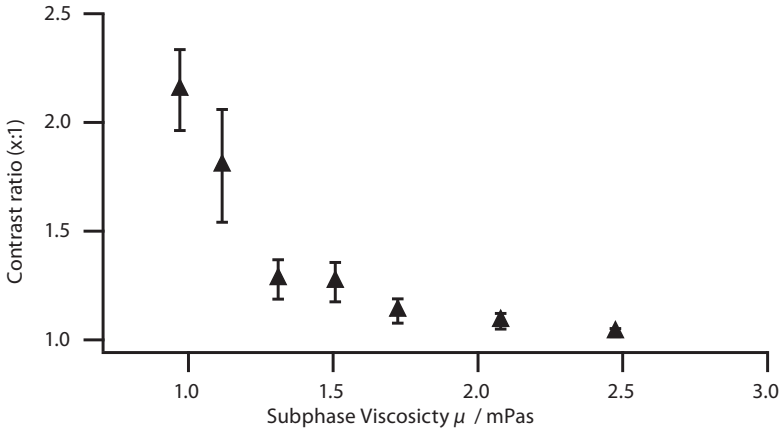


Figure 3.4 – Contrast ratio as a function of subphase viscosity μ . The contrast ratio is defined by Equation 3.1.

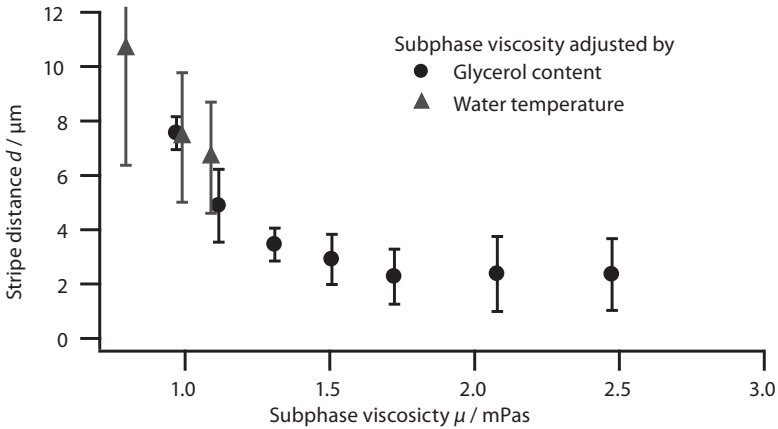


Figure 3.5 – Stripe to stripe distance d as a function of subphase viscosity μ . Above $\mu = 2.5$ mPa s microscopic images showed a homogeneous distribution making it impossible to determine a stripe to stripe distance. The subphase viscosity μ was varied by changing either the glycerol content (circles) or changing the subphase temperature (triangles).

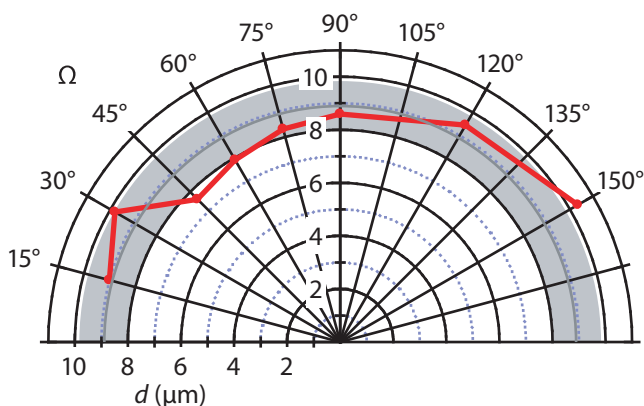


Figure 3.6 – Dependence of stripe to stripe distance d on the dipping angle Ω (see Figure 3.1 on page 55 for definition) between subphase and substrate. The transfer speed of 5 mm min^{-1} was applied in the plane of the substrate. The stripe distance is not significantly influenced by the dipping angle Ω .

patterns. The decrease of contrast as a function of subphase viscosity is displayed in Figure 3.4 on the preceding page. A second approach to vary the subphase viscosity is the variation of subphase temperature¹⁰⁹. This gives only access to a very limited range of subphase viscosities. On the other hand the chemical properties of the subphase remain unchanged and the range can be extended to below $\mu = 1 \text{ mPa s}$. The results from both variation methods are shown in Figure 3.5 on the previous page. In both cases the change in surface tension is neglected. The largest deviation of $72.8 \text{ mN m}^{-1} - 69.3 \text{ mN m}^{-1} = 3.5 \text{ mN m}^{-1}$ for 40 % weight glycerol is still small compared to the surface pressure during transfer (30 mN m^{-1}) and the surface tension of water.

3.1.3 Dipping Angle

The third parameter varied is the dipping angle Ω . The sample was moved out of the subphase at $v = 5 \text{ mm min}^{-1}$ in the direction given by the dipping angle Ω . Results are shown in Figure 3.6 for a variation of Ω from 15° to 150° . Within the experimental error no variation of the stripe to stripe distance with the dipping angle can be observed.

3.2 OBSERVATION OF THE THREE-PHASE CONTACT LINE

Observing the monolayer formed by the lipid lipopolymer mixture at the air–water interface using fluorescence microscopy, a homogeneous distribution of the fluorescent marker is detected indicative of a mixing of the two components. After the deposition of the monolayer by LB transfer a stripe pattern is clearly discernible. These two observations limit the transition to the demixed state to the meniscus region during the LB transfer. To further narrow down the location and cause of the phase separation two experimental setups were specifically prepared to allow the close observation of the meniscus region. Imaging ellipsometry allows the laterally resolved measurement of the height on the substrate with a resolution down to several Ångstrom, as discussed in Section 1.3.2 on page 19. Complementary to this, fluorescence microscopy shows the lateral distribution of the fluorescent marker which indicates the phase separation. Combining these two methods a detailed picture of the dynamic occurring during the transfer is gained. In the following sections the experimental setups will be outlined in detail followed by the measurements performed with these instruments.

3.2.1 Langmuir Trough Combined with Ellipsometer

Experimental Setup

In this section the combination of a preparational with an observational instrument is presented which has been specifically designed for the observation of stripe pattern formation. A schematic is shown in Figure 3.7 on the following page. A Multiskop (Optrel, Kleinmachnow, Germany) was used for ellipsometric imaging. The ellipsometer works in PCSA configuration and image forming capabilities are introduced by an objective (M-Plan APO 10×, Mitutoyo, Neuss, Germany) and a position sensitive detector (EHD[®]kamPro02, EHD imaging, Damme, Germany). The sample is illuminated by a HeNe–laser operating at 6328 Å as shown schematically in Figure 3.7 on the next page. The dipper holding the substrate was attached to the goniometer ring of the Multiskop. A modified mirror holder (KMS/M, Thorlabs, Dachau, Germany) attached to the dipper allowed precise adjustment of the substrate with respect to the ellipsometer frame. Due to geometric constraints the dipping angle Ω was set to 75°. The incident angle Θ was 40°. The Langmuir trough was adjusted in height to see the onset of the meniscus in the ellipsometric image on the substrate. The nulling conditions were set to be fulfilled on the bare substrate. Using off–null ellipsometry and the repeat length for successive fulfilling of the nulling condition, the ellipsometric period, a height profile can be reconstructed. This is limited to small contact angles below $\approx 10^\circ$ by the ratio between microscopic resolution and increase in height. The increase in film thickness has to be

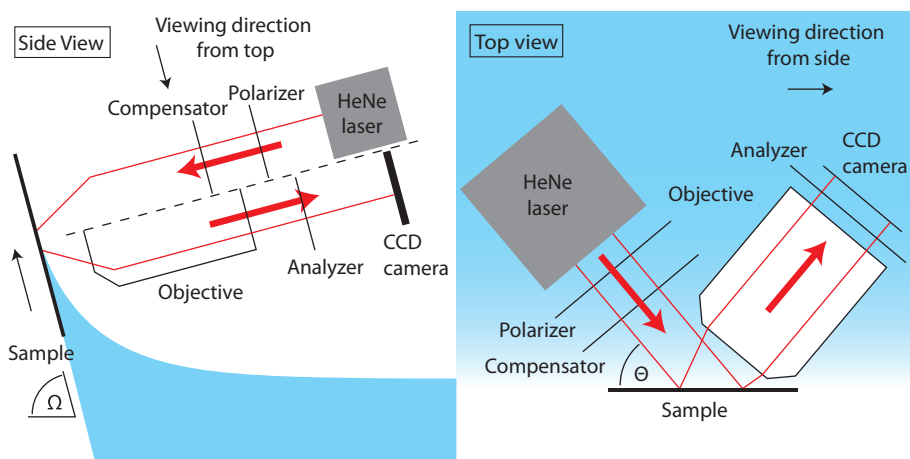


Figure 3.7 – Schematic illustration of the ellipsometer combined with the Langmuir trough used for LB transfers. Monochromatic light from a HeNe-laser passes through a polarizer and compensator before being reflected on the sample at an angle of incidence Θ . Reflected light is collected by an objective and after passing through the analyzer forms an image on the CCD-camera. The sample is immersed into the subphase as shown in the left panel at an angle Ω . The optical path is split showing the path of the incident light above the dashed line and the path of the reflected light below.

less than half of the ellipsometric period over the lateral distance of the microscopic resolution according to the Nyquist theorem.

Experiments are performed analogous to the monolayer deposition using LB transfer as explained in detail in Section 1.2.1 on page 9. The substrate attached to the modified dipper was adjusted in all three degrees of freedom to be normal to the plane of incidence of the ellipsometer and to reflect the incident beam into the center of the CCD-camera. The ellipsometer was set to fulfill the nulling condition on the bare substrate. The subphase fluid was poured into the Langmuir trough and the substrate immersed into the subphase. Spreading of the lipid lipopolymer mixture was followed by compression to 30 mN m^{-1} . Keeping the surface pressure constant the deposition on the substrate proceeded by slow removal of the substrate from the subphase. The position of the meniscus on the substrate was adjusted by adding or removing subphase fluid to the Langmuir trough behind the barrier confining the monolayer. Once the meniscus was adjusted to be visible in the field of view, images were taken while proceeding with the transfer.

Experiments

Pure Subphase Before spreading amphiphile mixtures on the subphase the contact line of the subphase with the substrate was observed. From this the contact angle can be calculated and the reliability of the measurement can be assessed. The ellipsometric image of water in contact with a cleaned silicon substrate is shown in panel A) of Figure 3.8 on the next page. In the top part of the image the substrate is uncoated. This appears black as the ellipsometer has been set to fulfill the nulling condition on the substrate. Going downwards, more than twenty interference stripes can clearly be distinguished. The distance between the interference becomes smaller as the angle of the meniscus with the substrate becomes larger. Between the red lines a line profile is taken which is plotted in panel B) of Figure 3.8 on the following page. The intensity minima indicated by blue dots require fulfillment of the ellipsometric nulling-condition which is repetitively fulfilled for an increase in height by the ellipsometric period (see Section 1.3.2 on page 19). For a water film ($n_{\text{H}_2\text{O}} = 1.333$) in air ($n_{\text{Air}} = 1.000$) the ellipsometric period becomes $D = 2900 \text{ \AA}$. From this we can reconstruct the form of the meniscus which is shown in panel C) of Figure 3.8 on the following page. To check the reliability of the measurement, the analytical description for the shape of the meniscus given by Equation (3.4) has been fitted to the experimental data with only the contact angle as a parameter. The capillary constant for water is $a = 3.9 \text{ mm}$ with which the fit results in a contact angle of $\alpha_r = 2.34^\circ \pm 0.02^\circ$.

Monolayer Covered Subphase A transfer of 94.8 mol % SOPC with 5 mol % PMO_{x14} and 0.2 mol % TRITC-DHPE at $\Pi = 30 \text{ mN m}^{-1}$ and $v = 5 \text{ mm min}^{-1}$ was observed using imaging ellipsometry. A single image taken during the transfer is shown in panel A) of

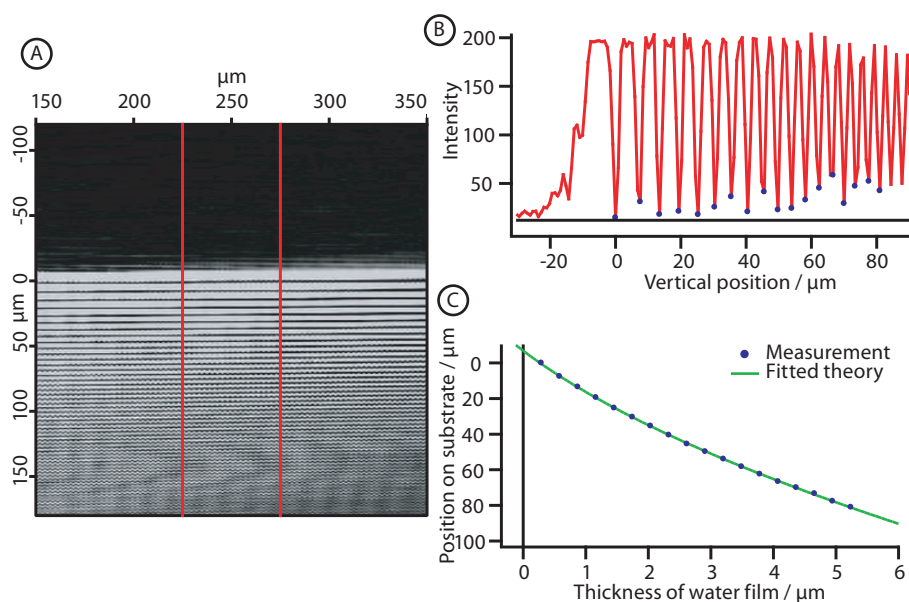


Figure 3.8 – A) Ellipsometric image around the three-phase contact line of pure water with a silicon substrate in air. B) Intensity profile along z around the three-phase contact line. The intensity profile is taken between the two red lines in panel A). Eighteen clear minima, where the ellipsometric conditions are repetitively fulfilled, are marked with blue circles. C) Vertical position on the substrate plotted against the reconstructed water film thickness (blue circles). The green solid line is a fit to the data of the analytical description of the meniscus form with the contact angle as parameter. The contact angle with the substrate is $\alpha_r = 2.34^\circ \pm 0.02^\circ$.

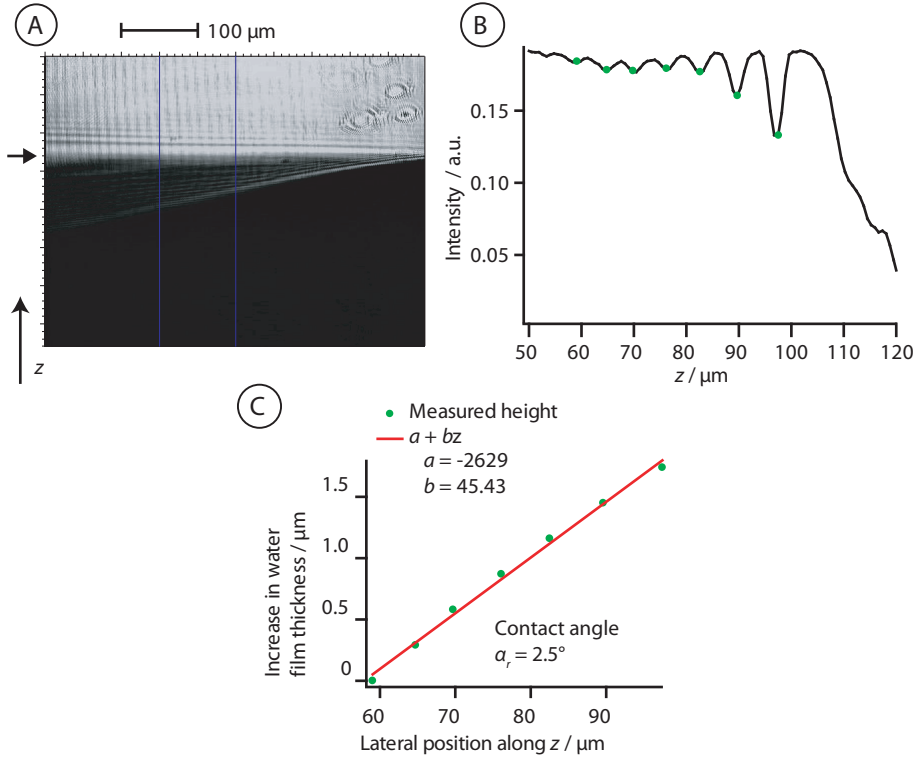


Figure 3.9 – A) Ellipsometric image around the three-phase contact line during LB transfer. The transfer direction is along z . Horizontal stripe patterns in the upper part are not due to the separation of the components in the monolayer but are an optical artifact. B) Intensity profile along z around the three-phase contact line. The intensity profile is taken between the two blue lines in panel A). Seven clear minima, where the ellipsometric conditions are repetitively fulfilled, are marked with green circles. C) Thickness of the water film calculated from the interference minima in panel B) plotted against the position along z . The height profile in this region can be approximated by a line. The contact angle with the substrate is $\alpha_r = 2.5^\circ$ in this region.

Figure 3.9 on the previous page. The ellipsometric image shows the coated substrate. Starting at the bottom, the substrate is covered by a thick subphase film (meniscus). Going upwards along z , the film becomes thinner. At the position indicated by the arrow the film is thin and the angle with the substrate is sufficiently small to result in interference stripes. The intensity minima in the region above the arrow are indicated by green circles in panel B) of Figure 3.9 on the preceding page. From the ellipsometric period of a water film in air ($D = 2900 \text{ \AA}$) a height profile in this region can be reconstructed as plotted in panel C) of Figure 3.9 on the previous page. This height profile is approximated by a line. The slope of the line corresponds to a contact angle of $\alpha_r = 2.5^\circ$ between the substrate and the subphase. The vertical parallel lines are not the stripe patterns due to lipid–lipopolymer demixing but are an optical artifact.

3.2.2 Langmuir Trough Combined with Fluorescence Microscope

Experimental Setup

A self-built fluorescence microscope attached to the Multiskop analogous to the setup for imaging ellipsometry was used to study the lateral rearrangement of lipopolymers during transfer. The setup is shown schematically in Figure 3.10 on the facing page. The same objective (M-Plan APO 10 \times , Mitutoyo, Neuss, Germany) as for imaging ellipsometry was used but correctly positioned with respect to the sample to create parallel light in the back focal plane of the objective. Therefore the effective numerical aperture was $NA = 0.28$ with a diffraction limited resolution of $1.4 \mu\text{m}$. The image is formed on a CCD-camera (Orca 285, Hamamatsu Photonics, Herrsching, Germany) by focusing through a tube lens ($f = 150 \text{ mm}$). The optical components were mounted in a cage system (Linos Photonics, Göttingen, Germany) which was attached to the detector arm of the Multiskop via an adapter built in the local mechanical workshop. A mercury vapor arc lamp (EXFO X-cite 120, Mississauga, Ontario, Canada) illuminated the sample. Köhler illumination is achieved by focusing through a condenser lens. After passing through an excitation filter (531 nm, width: 40 nm) and being reflected by a dichroic mirror (562 nm) the light reaches the sample. Emitted fluorescent light passes through the dichroic mirror and is filtered by an emission filter (593 nm, width: 40 nm) before reaching the CCD-camera. The filterset is from AHF Analysentechnik (Tübingen, Germany).

Experiments

Analogous to imaging ellipsometry a closer look at the dynamics of the pattern formation was taken using fluorescence microscopy. Figure 3.11 on page 66 shows the meniscus in the lower part with the subphase thickness on the substrate becoming increasingly thinner until reaching the three-phase contact line. No demixing of the lipid-

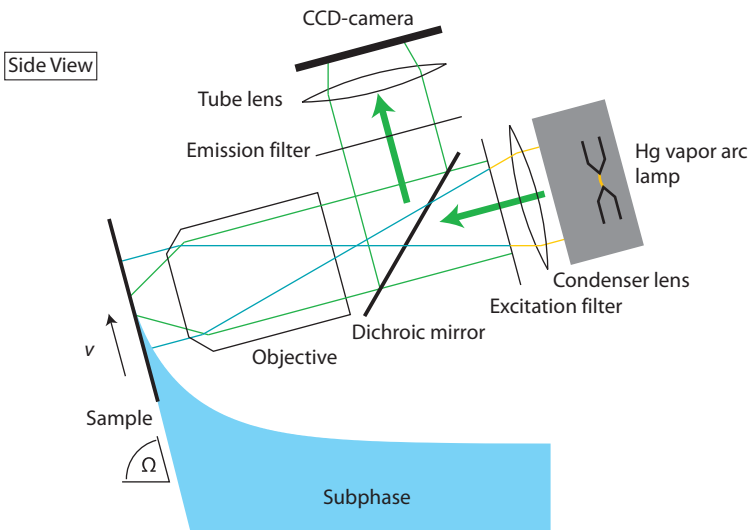


Figure 3.10 – Schematic illustration of the fluorescence microscope combined with the Langmuir trough. Light is generated by a mercury vapor arc lamp. A narrow band of wavelength passes through the excitation filter and the dichroic mirror. The light is focused into the back focal plane of the objective to achieve Köhler illumination. The fluorescently emitted light from the sample is collected by the objective and reflected from the dichroic mirror. After passing through an emission filter the image is formed by a tube lens on the CCD-camera.

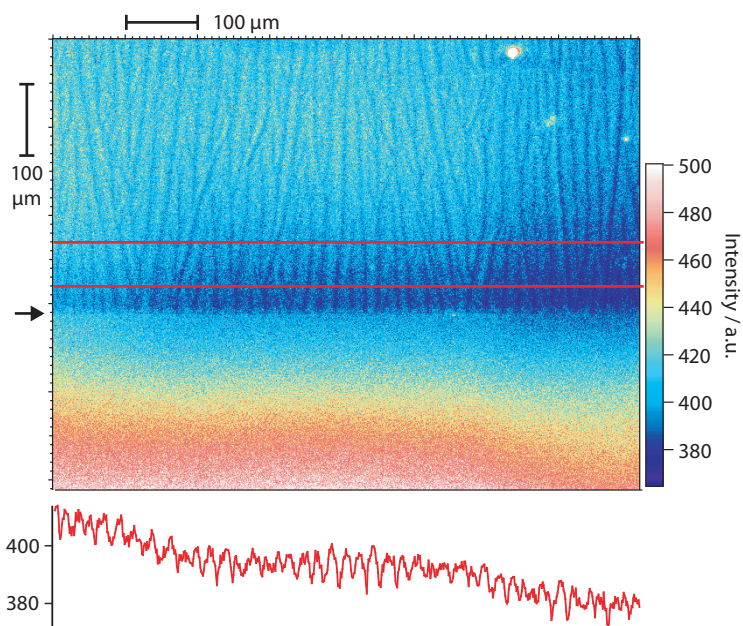


Figure 3.11 – **Top:** A snapshot fluorescence micrograph near the three-phase contact line of a lipid-lipopolymer mixture during transfer. No separation of the two components can be observed below the arrow while above, close to the substrate, a clear stripe pattern is visible. **Bottom:** Integrated intensity line profile taken between the two red lines in the micrograph above. Periodic maxima correspond to an increased concentration of fluorescently labeled lipids.

lipopolymer film can be observed while the subphase layer is thick. The top part of the image shows the fluorescently labeled monolayer with lateral structure. Within the resolution of the instrument the transition region from a homogeneous lipid–lipopolymer mixture to a stripe pattern can be restricted to be less than 5 μm .

At the onset of the meniscus with a larger contact angle an increased fluorescence intensity is expected due to the tilt of the lipid monolayer with respect to the observation plane. The positions coinciding based on this premise are marked with an arrow in panel A) of Figure 3.9 on page 63 and Figure 3.11 on the preceding page.

3.3 THEORETICAL MODELING OF STRIPE PATTERN FORMATION

3.3.1 General Considerations

For the physical origin of the stripe formation through LB transfer several possible scenarios have been identified.

1. The separation is driven by the underlying subphase which exhibits a pattern on the same length scale as observed on the transferred monolayer along the contact line.
2. By the transfer the conformal space of the polymers is changed leading to a variation in entropy which drives them towards each other as being solved in water is less preferential.
3. There exists a difference in wetting towards the surface between the lipopolymers and the lipids. This leads to an instability of the contact line with the observed spatial pattern.

The last scenario can already be excluded from the experiments presented in Section 3.2 on page 59 as the contact line was found to be homogeneous. This however does not exclude a difference in wetting. In the following sections a route of explanation is taken which does not start from a rigorous physical basis but uses a more phenomenological approach. The explanation is based on a mathematical description of a phase separation. This equation—the Cahn–Hilliard equation—is derived in Appendix C. Turning back to the experiments in Section 3.3.2 on the next page a relation is established between the experiments and the parameters encountered in the Cahn–Hilliard equation. With these considerations the Cahn–Hilliard equation is solved and the results are compared to the experiments in Section 3.3.3 on page 71.

3.3.2 Relationships Between Experiment and Theory

Before using the Cahn–Hilliard equation to account for the observations, the physical processes taking place during the transfer are considered. Furthermore the parameters controlled in the experiments are related to the parameters found in the Cahn–Hilliard equation. Apart from the focus on the direct applicability on the Cahn–Hilliard equation the following considerations will be valid and requisite for any theoretical description of the stripe pattern formation.

Diffusion at the Air–Water Interface

Diffusion constants of lipids at the air–water interface were measured by Peters & Beck on the order of $D = 50 \mu\text{m}^2 \text{s}^{-1}$ for a C16 chain in fluid state¹¹⁰. The results could be accounted for by a free volume model. The influence of the subphase viscosity on the viscosity of a monolayer at the interface was studied by Sacchetti *et al.*¹¹¹. They found that up to a 2.5 fold increase in subphase viscosity the surface viscosity of the monolayer was unchanged. As in this study the area per molecule was constant in this regime one can conclude that the diffusion constant according to the free volume model stays also constant. Further, Kang & Majda¹¹² studied the effect of immersion depth on the diffusivity of a diffusant in the monolayer and extended the Saffman–Delbrück theory¹¹³ to account for a cylinder that protrudes from the monolayer. This results in a strong dependency of the diffusion constant D on the subphase viscosity μ . The viscosity of air (0.017 mPa s) can be neglected since it is two orders of magnitude smaller than the subphase viscosity (water at 20 °C: 1 mPa s). Since this model is only a minor variation to the model by Saffman–Delbrück, it has the same limitation of being valid only for the dimensionless particle radius $\epsilon \ll 1$. Therefore the lipopolymers extending into the subphase are assumed to feel the increased viscosity while the lipid matrix is not influenced. The diffusion coefficient according to Kang & Majda is given by

$$D = \frac{kT}{4\pi(\eta h_1 + \mu h_2)} \left[\ln \frac{2}{\epsilon} - \gamma + \frac{4\epsilon}{\pi} - \left(\frac{\epsilon^2}{2} \right) \ln \frac{2}{\epsilon} \right] \quad (3.2)$$

with the dimensionless particle radius $\epsilon = \mu a / (\eta h_1 + \mu h_2)$. h_1 and h_2 are the immersion depth into the monolayer and the subphase and γ is Euler’s constant $\gamma = 0.57721 \dots$. From the experiment the subphase viscosity μ is well defined. The monolayer viscosity η can be estimated to be 40 mPa s¹¹⁴. Assuming $h_1 = 20 \text{ \AA}$ and $h_2 = 10 \text{ \AA}$ for PMOx14 the dependency on the subphase viscosity as shown in Figure 3.12 on the next page is obtained. This seems to agree with diffusion measurements on pure lipopolymer monolayers which can be expected to have a higher viscosity and were measured at higher areas per molecule⁹⁰. Based on this calculation a roughly inverse relationship between the polymer diffusion coefficient D and the subphase viscosity μ can be assumed.

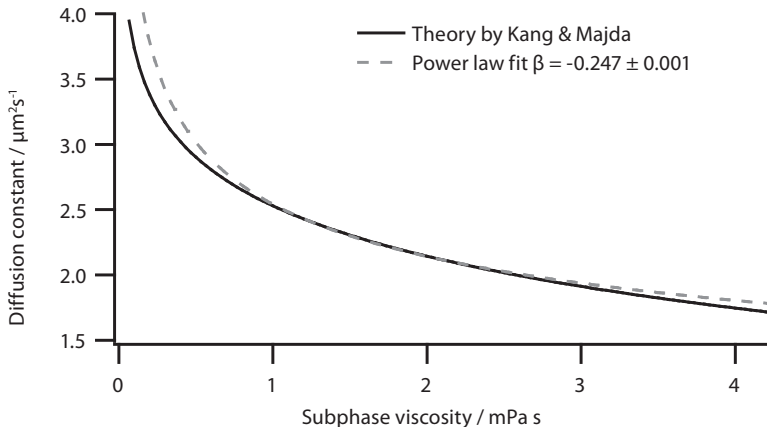


Figure 3.12 – Diffusion constant in dependence on the subphase viscosity according to Kang & Majda¹². Calculated using Equation (3.2). For parameters defining this dependency see text. A power law was fitted in the range from 1 mPa s to 2.5 mPa s yielding an exponent $\beta = -0.247(1)$.

Evolution of the Free Energy during Transfer

From the well mixed state on the air–water interface we can conclude that the free energy of the system has only a single minimum on energy scales well beyond the thermal energy. On the other side we have two separated minima for high and low concentrations of lipopolymer at some point during the transfer. The barrier separating the minima should not depend on the details of the transfer as long as the geometry is not changed significantly. This applies for example to the contact angle during the transfer. From a fixed form of the free energy at a certain point during transfer follows directly the reciprocal relation of the change in free energy to the transfer speed. The actual parametrization of the free energy with time cannot be derived and several options are considered in Section 3.3.3 on page 71.

Hydrodynamics in the Meniscus

A purely hydrodynamic origin, in the sense that the flow pattern of the subphase exhibits structures that lead to the observed stripe patterns, can be excluded from an experiment with a different lipopolymer. Furthermore it should have led to the observation of such stripe patterns in arbitrary binary mixtures much earlier. Since in experiments with poly(ethylene oxide) as a polymer of a lipopolymer no long range ordering is observed, no organized flow pattern along the three–phase contact line should be present⁴¹. To test whether the polymers enrich in the presence of a vortex flow, a sim-

pler geometry at the air–water interface can be used which allows *in situ* fluorescence microscopy observation.

In terms of hydrodynamics the geometry is similar to the problem considered by Landau & Lifshitz¹¹⁵. Their prediction of film thickness by dip–coating is important for industrial surface coating. Due to its widespread application a large body of literature related to this problem can be found^{116–120}. Even the effect of (unwanted) surfactants has been considered¹²¹ but the extrapolation to LB transfers as a high concentration impurity of insoluble surfactants and low speeds has so far only been marginally mentioned by de Gennes¹²². The characteristic form of a Landau–Levich film (cf. Figure 3 of Delon *et al.*¹²⁰) is observed for the longer of the here considered lipopolymers during LB transfer by eye. This might indicate a paradox situation. For a Landau–Levich film to appear, the transfer speed needs to be sufficiently high to prevent the subphase from dewetting the substrate. On the other hand to achieve a transfer ratio of unity for the Langmuir monolayer, the transfer speed needs to be considerably below this threshold.

Dimensional Analysis

A dimensional analysis was first done for the Landau–Levich problem, i.e., without surfactant present. This can be modeled using five dimensional parameters¹¹⁸: pulling speed v , acceleration due to gravity g , and to characterize the fluid, its density ρ , its viscosity μ and the surface tension γ . From these, two dimensionless constants can be formed: The capillary number $Ca = \mu v / \gamma$ and the Reynolds number $Re = \rho v a / \mu$ with the characteristic length scale, the capillary constant a , given by $a = \sqrt{\gamma / \rho g}$. While the study of Landau and Levich is concerned with the entrained film thickness by a fast transfer we consider here the stripe to stripe distance occurring at small transfer speeds. From the definition of the Reynolds number Re it is directly clear that it cannot be used as a universal constant for our problem since speed and viscosity enter reciprocal to each other which is not consistent with the experimental data. The capillary number Ca does not lead to a collapse of the data onto a master curve. A much better agreement yet no collapse is found by plotting the data against $\frac{\mu^3 v}{\gamma}$. If this holds some meaning an additional factor making this expression nondimensional is required.

To account for the quasi two dimensionality of the film, we can replace the viscosity by the 2D viscosity of the monolayer and replace the surface tension by a line tension. The capillary number stays a dimensionless constant with these replacements. But the 2D viscosity of the monolayer is not dependent on the subphase viscosity in the range the experiments were performed as demonstrated by Sacchetti *et al.*¹¹¹. So the influence of the viscosity is only on the protruding lipopolymers or has a hydrodynamic effect during the transfer. This already renders the attempt to define a 2D analogon to the capillary number useless for our purpose.

Starting from the physical parameters studied and known to play a role in the pro-

Table 3.1 – Physical quantities entering into a description of the LB transfer with the medium defining the quantity and the dimension.

Quantity		Defining medium	Dimension
Density		Subphase	$M L^{-3}$
Viscosity	μ	Subphase	$M L^{-1} T^{-1}$
Surface tension		Subphase	$M T^{-2}$
Surface viscosity		Monolayer	$M T^{-1}$
Surface pressure		Monolayer	$M T^{-2}$
Gravitational acceleration			$L T^{-2}$
Transfer speed	v		$L T^{-1}$
Stripe distance	d		L

cess we can derive the following. We consider the stripe distance d , the transfer speed v , and the subphase viscosity μ . These have the dimensions:

$$d : [L] \quad v : [LT^{-1}] \quad \mu : [ML^{-1}T^{-1}]. \quad (3.3)$$

As only the viscosity involves mass, a further parameter involving mass is necessary. The two quantities v and μ define also the shear stress $\tau = v \frac{\partial \mu}{\partial y}$. This is not only relevant between substrate and subphase but also between subphase and monolayer respective superphase. An interfacial velocity proportional to the transfer speed has been observed by Fuentes & Cerro¹²³. Possible additional quantities involved in the process are shown in Table 3.1. Resulting in seven quantities for the whole system. As there are three physical quantities, four dimensionless variables for this system can be defined. This has not yet been studied systematically due to the large number of possible combinations and the unknown effect of some of the physical parameters. Furthermore the list given in Table 3.1 might be incomplete. For a similar geometry the analysis is performed by Naire *et al.*^{124, 125} with the focus on the fabrication of foams.

3.3.3 Comparison to Experiments

Linearized Cahn–Hilliard Equation

As a first step to assess whether the Cahn–Hilliard equation is a suitable description of the experimental observation we look at the linearized version given by Equation (C.14) in Appendix C. Since the linearized version exhibits not the same rich features as the full equation only an agreement of basic tendencies between experiment and theory can be expected. For the experiments we can safely assume that there is always a fluctuation present at the beginning which is required to drive the system out of the metastable state at $c = 0$. From Equation (C.14) we have to consider three parameters:

- ♦ the mobility L ,
- ♦ the gradient energy coefficient γ and
- ♦ the second derivative of the free energy with respect to concentration $f''(c_m)$.

Looking at Equation (C.17) we can easily see the effect of two of the parameters on the wavelength of the structure observed in experiments. The wavelength \bar{l} is proportional to the square root of the gradient energy coefficient $\bar{l} \propto \sqrt{\gamma}$. The proportionality to the second derivative of the free energy is just reciprocal $\bar{l} \propto (f''(c_m))^{-1/2}$. The mobility L is not directly related to the most unstable wavelength \bar{l} and has only an effect in the time domain. Equation (C.16) shows that upon an increase of L the amplitude of the corresponding wavevector is increased. From this one can expect a larger L to lead to a faster transition from a homogeneous to a patterned distribution. For the comparison to the experiment we consider only the parameters L and $f''(c_m)$. The gradient energy coefficient γ is not accessible from the experiments reported here and is therefore kept as a constant with time.

Mobility L As outlined in Section 3.3.2 on page 68, the mobility L is roughly inverse proportional to the subphase viscosity μ . Varying the subphase viscosity μ linearly from 1 mPa s–2.5 mPa s we observe an increase in wavelength. This is consistent with the expected tendency of an increasing structural size at higher mobilities.

Free Energy $f''(c_m)$ A more negative second derivative of the free energy with respect to concentration $f''(c_m)$ is the result of a more strongly curved free energy $f(c)$. This means a local change in composition is energetically more favorable. Therefore we can expect the separation to happen faster, and as this process is opposed by the mass transport, also on shorter length scales. As we saw on page 69, we cannot assume the free energy to be constant over the time of the transfer. Instead we start from a single minimum which in the course of the transfer is separated by an increasing energy barrier into two minima. The development of the free energy with respect to time reduced by the duration of the transfer is always the same. For faster transfer speeds v the rate of change in $f(c_m)$ and therefore also in $f''(c_m)$ is larger. The time average $\langle f''(c_m) \rangle$ increases with the transfer speed v and matches the experimental observation.

Numerical Simulations

To explore the rich behavior of the Cahn–Hilliard equation, numerical simulations were performed, since no analytical solution of this fourth order partial differential equation is known. The simulations used the FiPy framework¹²⁶ which is developed at the National Institute of Standards and Technology (NIST, Gaithersburg, MD, USA).

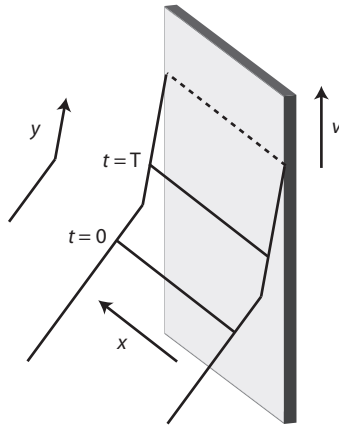


Figure 3.13 – Geometry of the LB transfer used in the numerical simulation. The substrate is moved upwards at a speed v . In the 1D simulation a line along x is followed by its traverse over the kink in the meniscus on the air–water interface. In the 2D simulations the conditions of the kink are moved over the simulation area.

FiPy contains a solver for partial differential equations based on a standard finite volume approach. The finite volume method (FVM) is a special case of the finite element method. The FVM dissects the simulation volume into discrete finite volumes. Using the divergence theorem parts of the equation containing a divergence term can be transformed into a surface integral. These surface integrals can then be evaluated as the fluxes at the volume boundaries. Introductions to the FVM can be found in Versteeg & Malalasekera¹²⁷ or Patankar¹²⁸.

Simulation Geometry The time evolution of the concentration of the lipopolymer was simulated in one or two dimensions. In one dimension this is analogous to a line on the air–water interface along the direction of the substrate. As time evolves, this line is moved upwards the meniscus and is eventually fixed on the substrate and moves upward with it. The position of the line at time $t = 0$ and $t = T$ is not known but an upper boundary to the length scale between the two timepoints can be given from the fluorescence microscope experiments on the three–phase contact line. From these experiments not more than $5 \mu\text{m}$ are between the homogeneous distribution on the air–water interphase and the separated structure. The geometry considered in the simulation is shown in Figure 3.13. For simulations in two dimensions an area of the air–water interface is considered which is moved over the conditions representing the kink in the meniscus. In the simulations we set $c_m = 0$ without loss of generality. To trigger the evolution of the instability we set the initial concentration of lipopolymer $c(x)$ to be

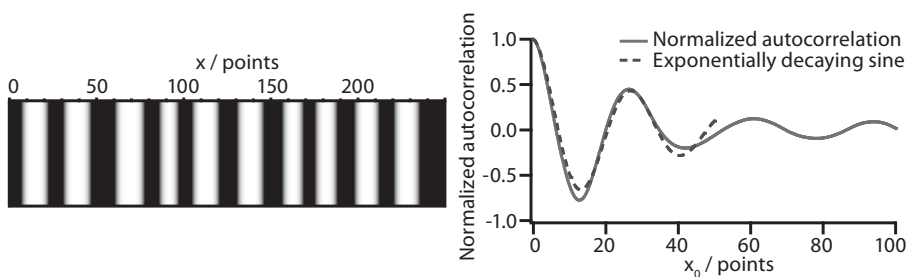


Figure 3.14 – **Left:** Result of the numerical simulation of the Cahn–Hilliard equation. Bright corresponds to a high concentration of lipopolymer whereas dark corresponds to a high concentration in lipid. Parameters used in this simulation are: $L = 0.2$, $\alpha = (t/T)$, $\gamma = 1$. **Right:** Normalized autocorrelation of a one dimensional concentration profile. An exponentially decaying sine is fitted to approximately the first two periods. The frequency of the sine relates to the spatial length scale observed in the pattern. Here approximately $l = 27$ points.

randomly distributed along x with the distribution being gaussian with a variance of $\sigma^2 = 0.01$.

Data Evaluation The one dimensional simulation results in a concentration profile $c(x, t)$ of the lipopolymer. We are only interested in the final state so only the profile at $t = T$, as shown left in Figure 3.14, is considered. We calculate the spatial autocorrelation of this final profile ($c(x, T)c(x + x_0, T)$). Onto the autocorrelation an exponentially decaying cosine is fitted starting at $x_0 = 0$ up to a position corresponding to approximately 2 phases of the cosine as shown right in Figure 3.14. From the frequency of the cosine (corresponding to x_0 of the first maximum) we get the average spatial separation of the pattern.

Transfer Speed As outlined in Section 3.3.2 on page 68, the free energy changes during the transfer process from a single minimum to a form with two minima. Since it is not possible to change an analytical function $c(\alpha)$ continuously from a single minimum at a fixed position c_m to a form with two minima located at two other fixed positions c_0 and c_1 , the free energy is modeled as given in Equation (C.11). The parameter α is set to $\alpha = 0$ at $t = 0$. As within the range of transfer speed the dynamic contact angle is almost unchanged we can assume a fixed characteristic length on which the transition takes place. The different transfer speeds are therefore linear proportional to the reciprocal time required to traverse this transition region. A fast transfer speed is simulated by a small T whereas a slow transfer speed requires simulation to a large T .

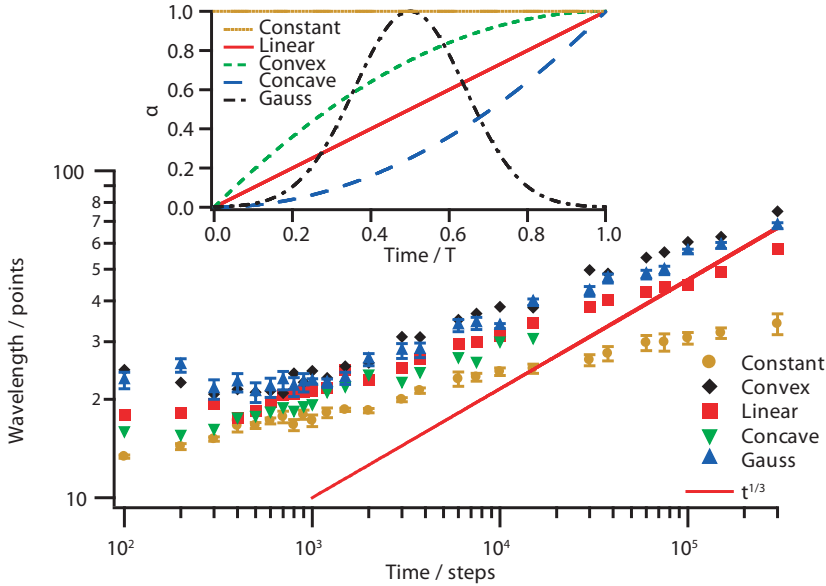


Figure 3.15 – Top: Variation of the free energy parameter α with time. **Bottom:** Wavelength of the stripe pattern in dependence on the simulation time T and the temporal evolution of the free energy parameter α as shown on the top. For comparison the late stage coarsening rate of $t^{1/3}$ is shown as a solid line.

For the simulations we set the parameters arbitrarily to

$$\gamma = 1, \quad L = 0.5.$$

The time evolution of α is displayed on the top in Figure 3.15. The resulting wavelength dependency on duration is shown on the bottom in Figure 3.15.

For long times the evolution with time is proportional to $t^{1/3}$ in accordance with Lifshitz & Slyozov¹²⁹. For shorter times different exponents in the transition to the late stage were found¹³⁰. Here, exponents of approximately 0.2 are found and the transition to the late stage is not completed in the simulations presented. For the initial stage differences in the minimal occurring wavelength can be observed. These differences can be explained by the linearized Cahn–Hilliard equation which predicts a wavelength as given by Equation (C.17). The effective value of the second derivative of the free energy $f''(c_m)$ depends on the temporal evolution of α for short times. Comparing the top and bottom graphs in Figure 3.15 this can be seen as for larger average α up to $0.1T$ the wavelength becomes smaller. The exponents found for the intermediate state increase in the same order as the initial minimal wavelength. As these results show,

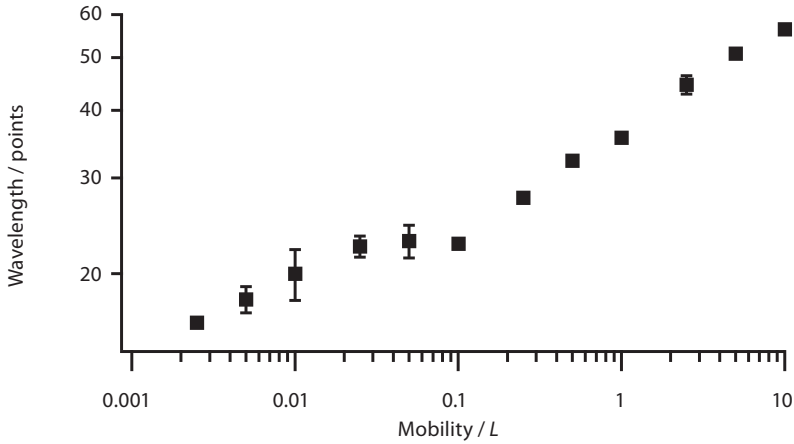


Figure 3.16 – Wavelength as a function of the mobility L .

only marginal differences upon a change in the time evolution of the free energy occur. Since the scale in time and space can be chosen arbitrarily no further information can be gained from the simulations regarding the experiments. Especially no discrimination of how the free energy evolves during the LB transfer can be made.

Subphase Viscosity The mobility L is closely related to the diffusion of the particles. The dependency of the wavelength on the mobility is shown in Figure 3.16. The parameters for the simulation were

$$\gamma = 1, \quad \alpha = (t/T)^2, \quad T = 6000$$

with $L \in [10, 0.005]$. Analogous to the increase in simulation time the effect of an increase in mobility is a larger wavelength. This can be understood as the particles can move faster and the same state of coarsening can be reached at an earlier timepoint. The functional dependence is well captured by a power law with an exponent 0.16(1) similar to the exponents found for the variation in T . Again this observation matches the experimental data qualitatively. A closer relationship cannot be established since the scaling can be chosen arbitrarily.

2D Simulations A narrow strip where demixing is favorable was moved over the simulation area. The strip is parametrized by a gaussian function of α with a width of approximately one tenth of the simulation length. Within the duration of the simulation the peak of the strip was moved from one end to the other of the simulation area. As the strip width where demixing can occur is narrow, the total simulation time required

to observe demixed structures increases. After the demixing the particles diffuse freely and start to mix, therefore the time until fixing them (attachment to the substrate) as well as their mobility are important parameters. A few configurations were simulated and representative results at $t = T$ are shown in Figure 3.17 on the next page. The demixing zone moved from top to bottom. Variation of the mobility was done in the range of $L \in \{0.1, 0.01, 0.001\}$ and $T \in [100, 30000]$. In the studied parameter space no significant demixing can be observed apart from a stripe pattern *parallel* to the transfer direction. This is most likely a simulation artifact due to the periodic boundary conditions and is not considered further. The coupling of one spatial dimension with the direction of moving the zone where demixing occurs introduces effectively a new parameter. If this parameter can lead to the merging events observed in the experiments is yet an open question. As it was found in the simulations in one dimension the late stage is not reached yet and requires even longer simulation times. Due to the high computational expenses further variations should therefore be based on a more detailed theoretical analysis decreasing the number of configurations needed to be simulated.

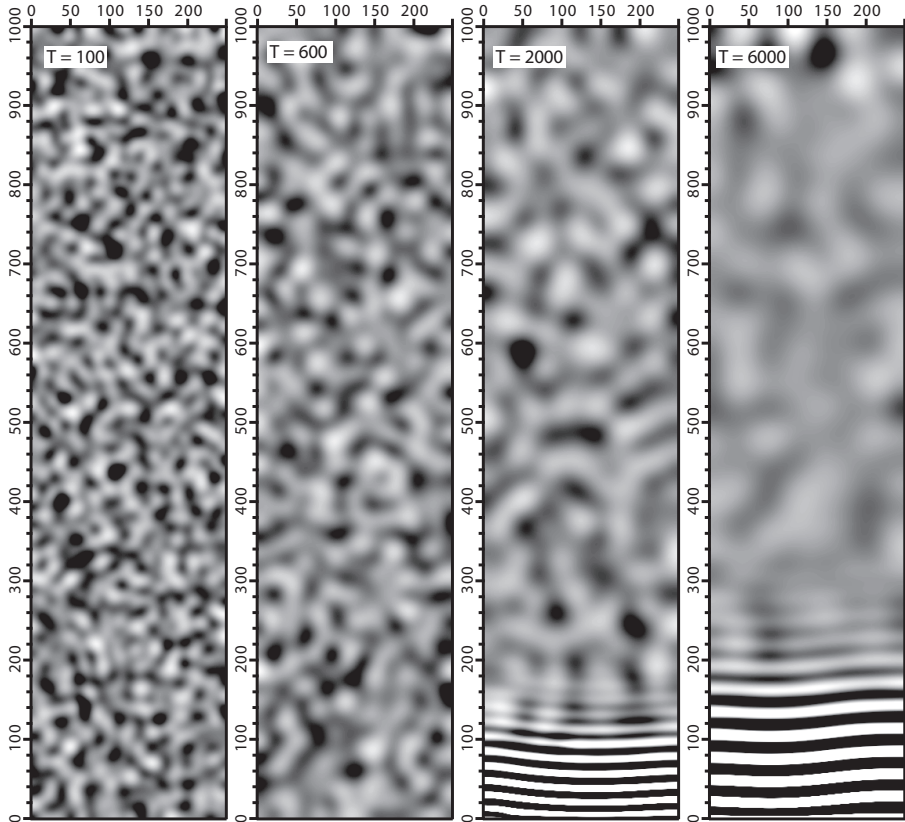


Figure 3.17 – 2D simulation of the Cahn–Hilliard equation for durations $T = 100, 600, 2000,$ and 6000 and $L = 0.01$. The free energy was varied with time and decomposition only favorable in a narrow strip which moved from top to bottom over the duration T of the entire simulation. After passing this strip the particles diffuse freely and mix again. The horizontal stripes towards the end of the simulation for long durations are artifacts of the chosen boundary conditions. The scaling in the figure is set for all simulations such that black corresponds to a fraction of 0.48 whereas white corresponds to 0.52 of one component.

3.4 DISCUSSION

The dependency of the stripe distance on transfer speed v and subphase viscosity μ suggests a hydrodynamic process underlying the pattern formation. More time given to the process, i.e., slower transfer speeds lead to larger separations of the stripes. Likewise the mobility of the particles is important and, if reduced, the particles can move only smaller distances in the same time. On the other hand no effect was found for the variation of the dipping angle Ω . While the change of dipping angle has an effect on the macroscopic geometry of the meniscus the microscopic contact angle is solely determined according to Young's law at a simple three-phase contact line. In the case of a pure subphase the increase in film thickness $h(z)$ on a substrate immersed at $\Omega = 90^\circ$ follows the analytical expression

$$h(z) = -\frac{a}{\sqrt{2}} \cosh^{-1} \frac{\sqrt{2}a}{z} + a \sqrt{\left(2 - \frac{z^2}{a^2}\right)} + x_0 \quad (3.4)$$

where a is the capillary constant and x_0 is set by the contact angle¹³¹. For purified water on silicon substrates contact angles on the order of 2° were measured by fitting Equation (3.4) to the thickness profile. Here, we have an additional amphiphilic monolayer which has yet another effect on the microscopic form of the meniscus. A large contact angle (approximately 30°) can be observed when looking at the substrate from the side. This is due to the presence of the monolayer at the air-water interface which reduces the surface tension. In the current experiments the surface tension was reduced to $\gamma = 72.7 \text{ mN m}^{-1} - 30.0 \text{ mN m}^{-1} = 42.7 \text{ mN m}^{-1}$. Close to the substrate an extremely small contact angle of 2.5° could be measured with high precision using imaging ellipsometry. When the subphase is covered with amphiphiles their presence seems to be non dominating in the uppermost part of the meniscus. At a water film thickness of $\approx 2 \mu\text{m}$ a change occurs. A kink in the meniscus leads to the much larger contact angle observed so far for successful LB transfers¹³². From observations using fluorescence microscopy one can conclude that this kink is the origin of the stripe pattern formation.

The drag from the moving substrate drives the molecules at the air-water interface through this kink. The passage through the kink plays the role of a quench into the ordered phase for the lipid-lipopolymer mixture. An obvious change occurs in the geometry while all other physical parameters (temperature, surface pressure, film velocity) are expected to be constant or change only slightly and steadily. From the orientation of the amphiphiles and the direction of the kink, a strong reduction of space in the alkyl chain region is apparent or equivalent an increase in area in the head group region. The average distance of the polymers in the experiments is about four times their lateral extent which allows us to exclude steric interactions of the polymers to dominate. If only curvature is responsible for a quench into the ordered phase, a phase separation between lipids and lipopolymers should also occur in vesicles below a threshold size at

the same conditions of temperature, surface pressure and composition.

Following an argumentation by de Gennes¹²², one can relate a contact angle to a maximum transfer velocity. Below this maximum transfer velocity a LB transfer is successful, i.e., resulting in a transfer ratio on the order of 1, and above which the substrate is dip coated, leaving a subphase film on the substrate according to Landau & Levich¹¹⁵. This relation is given by

$$v_{\text{Max}} = \frac{\gamma}{36\sqrt{3} \, 12\mu} \alpha^3. \quad (3.5)$$

When we calculate the maximum velocities for contact angles of $\alpha = 2.5^\circ$ and $\alpha = 30^\circ$ we find us well below the dip coating threshold for 30° at $v_{\text{Max}} \approx 2000 \text{ mm min}^{-1}$ whereas all presented experiments except one lie above $v_{\text{Max}} = 1.1 \text{ mm min}^{-1}$ for 2.5° . This paradox situation might hold the key to the observed phase separating phenomena.

Plotting the experimental data of the stripe pattern formation against the time required to cover a distance of $1 \mu\text{m}$ in a double logarithmic plot, two regimes can be identified as shown in Figure 3.18 on the facing page. For short times (fast transfer speeds) a stronger increase in stripe distance is found than for slower transfer speeds (long times). For long time scales the experimental findings can be explained by a power law with an exponent of $\beta = \frac{1}{3}$. This suggests that the stripe formation is due to a spinodal decomposition following the Cahn–Hilliard equation^{133,134}. For the Cahn–Hilliard equation Lifshitz & Slyozov¹²⁹ showed that the growth of the observed structure follows $t^{\frac{1}{3}}$ for long times. For short times (fast transfer speeds) a different exponent $\beta \approx 0.8 \pm 0.1$ was found. This requires another dominating mechanism for the separation of the constituents. Along with this change in growth rate an increase in merging events during the transfer is observed. In panel B) of Figure 3.2 on page 55 the emergence of new stripes can be seen which join with other stripes shortly after in the course of transfer to retain the equilibrium distance. An explanation for the merging events requires at least a second independent variable which describes the evolution in transfer direction, coinciding with the temporal axis.

Transitions in growth rates of phase separating systems were observed in different experiments and simulations¹³⁵. Experiments deal often with structures in three dimensions where binary or ternary mixtures in bulk are observed.^{136–138} A number of reports also investigated the structure formation in two dimensions which is normally driven by the dewetting of a thin film^{139,140}. In contrast, here experiments take place in a quasi one dimensional geometry. So far the effect of the shear exerted by the subphase on the monolayer during transfer was not considered. The shear is intrinsically coupled to the time in the experiments making a separate observation impossible. The increase of shear with decreasing time enhances the relevancy for the growth regime with $\beta \approx 0.8$. This may be a lead to an extension of the Cahn–Hilliard equation describing both, the short time regime as well as the accompanying variation in merging frequency.

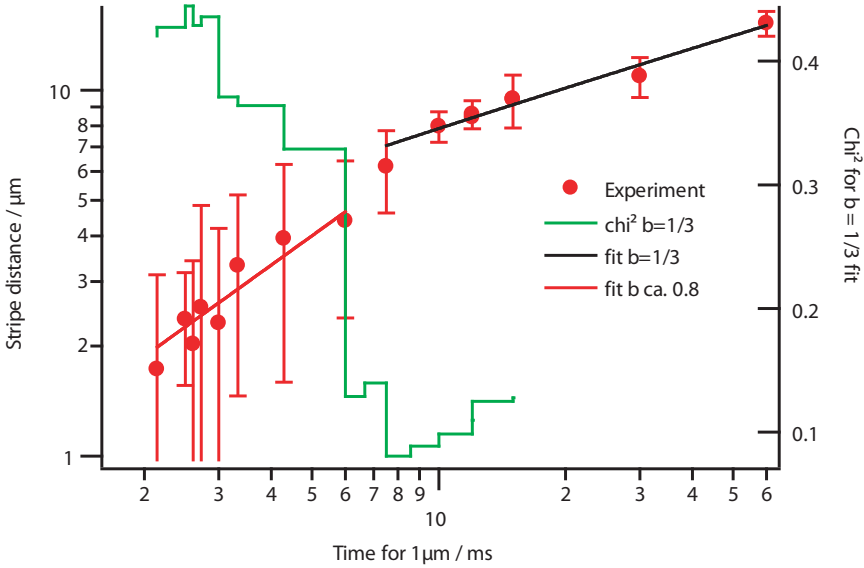


Figure 3.18 – Experimental stripe distance plotted against time required to cover 1 μm at the transfer speed v (red dots). From the χ^2 of a power law fit with exponent $\beta = \frac{1}{3}$ (green line) two regimes can be identified. For long times the data fits well to a power law with exponent $\beta = \frac{1}{3}$ (black line) while for short times an exponent of $\beta \approx 0.8$ is more suitable (red line).

3.5 CONCLUSION

A phase separation was observed during LB transfer of lipid-lipopolymer monolayers on a substrate. Parallel stripe patterns in the micrometer range are observed along the direction of transfer with long-range ordering continuous over the entire substrate length of several centimeters. The quantitative dependency between three preparational parameters and the characteristic length of stripe patterns was investigated. An increase in transfer speed is accompanied by a decrease in mean stripe distance. The variation of the subphase viscosity showed smaller stripe separations and less contrast for higher viscosities, clearly indicating a hydrodynamic origin of the patterning process. The stripe distance was found to be independent of the dipping angle which is understandable as the microscopic geometry is solely determined by the interfacial energies. This led to the design of two unique experimental setups with which a detailed view of the region where the phase separation takes place became possible.

A closer look at the dynamics of the separation process was taken with imaging ellipsometry and fluorescence microscopy combined to a Langmuir trough to observe the transfer process *in situ*. With imaging ellipsometry the height profile of the wetting film was reconstructed and small contact angles were measured with high accuracy. For lipid-lipopolymer mixtures on the air-water interface this revealed a region with an extremely small contact angle of 2.5° close to the substrate. At a water film thickness of about $2\ \mu\text{m}$ a sudden increase in contact angle is observed. In the region around this kink in the meniscus profile the phase separation occurs. Analysis of fluorescence microscopy images of the phase separating zone gives an upper estimate of $5\ \mu\text{m}$ for the length scale on which the separation takes place. These experiments give a clear picture of the geometry leading to the phase separation. An attempt was made to explain the observed phenomenon in the theoretical framework of phase separation. After a systematic assessment of the parameters it was found that for low transfer speeds the pattern formation can be understood as a spinodal decomposition described by the Cahn-Hilliard equation with a coarsening proportional to $t^{1/3}$.

CHAPTER 4

OUTLOOK

Based on the results of this work the usability of the studied membrane model was enhanced. Nevertheless several points can be identified which have to be addressed to facilitate the hassle free application as a plasma membrane model and deepen the physical understanding of membranes on solid supports.

Providing Surface Attachment

The currently available options of end functionalization of the polymer chain for attachment of the polymer to the substrate have been shown to have fundamental drawbacks. The use of piperidine provides only an adsorption to the surface which cannot withstand the harsh conditions present in vesicle fusion. Deposition of the distal leaflet by vesicle fusion on the other hand is a requirement for the incorporation of trans-membrane proteins as they can only be kept in vesicles in an aqueous environment. Replacing piperidine by trimethoxysilane binds the polymer covalently to the surface exposed hydroxyl groups. In the presence of water the binding is likely to occur between the polymers leading to polycondensation. This becomes especially problematic for high concentrations of lipopolymers which are required for large substrate membrane separations. As the polycondensated polymers are only adsorbed to the substrate the same problems observed with piperidine occur. A possible remedy is the use of a different surface coupling group where an activation is required to initiate the covalent coupling to the surface. The activation can take the form of a photon pulse or a change in chemical environment like pH.

Quantifying Membrane Substrate Interactions

The herein presented study of the interfacial forces between substrate and membrane modified by the polymer can only be an initial step highlighting the principal applicability. A systematic and detailed variation of polymer chain length and concentration will give a clearer picture of the forces present between membrane and substrate. The basic framework of measuring force–distance curves and attribution to three contributors can be extended to include smaller osmotic pressures. These can be attained by using solutes in water which cannot penetrate through the membrane and therefore exert an osmotic pressure¹⁴¹. Furthermore, adaption of the sample environments used for X–ray and neutron reflectivity to measure bilayers under water promise determination of substrate membrane distances with higher precision as available from ellipsometry.

Enhancing Anchoring in the Membrane

The stability of the Langmuir monolayers at the air–water interface has been seen to decrease with increasing number of monomer units. As the hydrophilic polymer becomes larger the molecule is easier to solvate in water. With the current lipid anchor ($2 \times C_{18:0}$) one hundred monomers seem to be the limit. To add a hydrophobic counterbalance to longer polymer chains, lipid anchors can be formed by transmembrane lipids. First steps towards this goal have already been taken. Michael Reif under supervision of Rainer Jordan (WACKER–Chair of Macromolecular Chemistry, TU Munich (now Professur für Makromolekulare Chemie, TU Dresden)) has purified caldarchaeol from the bacterial strain *Methanothermobacter thermautotrophicus* whose chemical structure is depicted in Figure 4.1 on the facing page. Also the asymmetric polymerization to transmembrane lipopolymers was successful. A first specimen with $n = 73$ monomer units (Ca-PMOx73) could therefore be already investigated at the air–water interface. For higher degrees of polymerization $n > 100$, the stability of the protection group (tert-butyl(methoxy)diphenylsilane) attached to the transmembrane lipid becomes an issue limiting the length of the synthesis. Isotherms of caldarchaeol and Ca-PMOx73 were recorded and are shown in Figure 4.2 on the next page and Figure 4.3 on page 86. Both form stable monolayers at the air–water interface. Caldarchaeol starts building up a surface pressure at an area of $\approx 110 \text{ \AA}^2$ per molecule, which is slightly higher than the onset observed for conventional lipids with a single hydrophilic group. This can be a sign of a ‘U’–shape bending where the two hydrophilic groups are exposed to the water while the hydrocarbon chain is bent and extends into the gas phase. Following the compression to lower areas per molecule a transition below $\approx 80 \text{ \AA}^2$ can be seen. This might be indicative of a switch from the ‘U’–shape to an ‘T’–shape of the molecules by which the area per molecule is halved whereas the monolayer thickness is doubled. This matches to the areas per molecule reported by Tomoiaia-Cotisel *et al.*¹⁴² who only observed ‘U’–bent membrane spanning lipids on the air–water interface. For a detailed

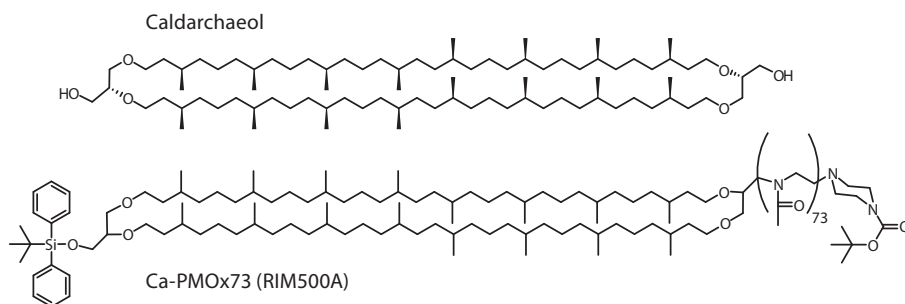


Figure 4.1 – Top: Chemical structure of caldarchaeol purified from *Methanothermobacter thermautotrophicus*. **Bottom:** Chemical structure of Ca-PMOx73 with BOC-piperazine end group.

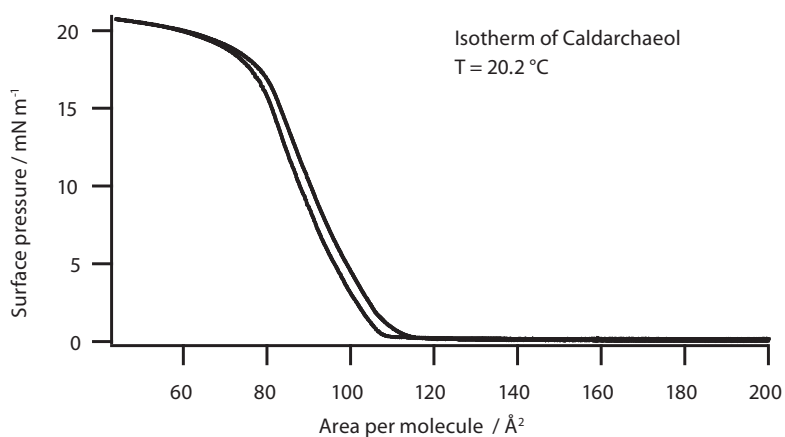


Figure 4.2 – Isotherm of caldarchaeol. The chemical structure is shown in Figure 4.1.

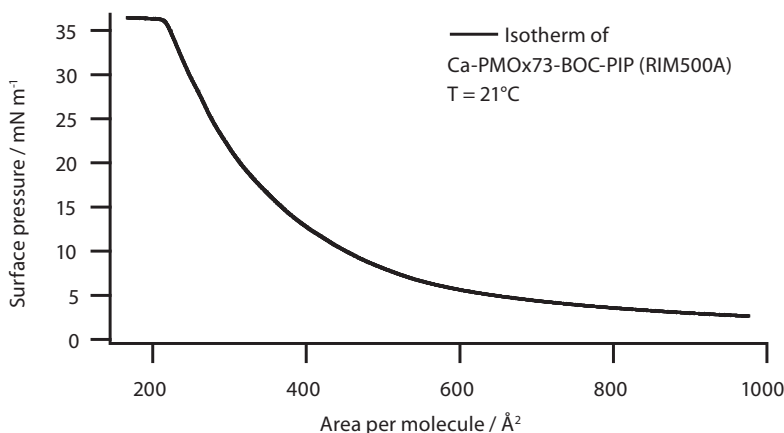


Figure 4.3 – Isotherm of the caldarchaeol based lipopolymer Ca-PMOx73 with BOC-piperazine end group. The polymer leads to an increase in surface pressure starting from areas per molecule in excess of 1000 Å². The film collapses at 36 mN m⁻¹. The chemical structure is shown in Figure 4.1 on the preceding page.

analysis the thickness of this monolayer has to be measured.

Application as Functional Membrane

To reach the ultimate goal of a membrane model, mimicking a living exemplar, functionality has to be included in the membrane. This means the incorporation of transmembrane proteins and/or the presentation of binding motifs in the form of carbohydrates. This is especially interesting in combination with the stripe patterns formed where two distinct environments are created. As shown before⁶³ and used thoroughly in this work, a third component (fluorescently labeled lipids, transmembrane protein integrin $\alpha_{\text{Ib}}\beta_3$) added to the membrane accumulates in the stripes formed during LB transfer. While components anchored only in one leaflet can be added using the LB-LS transfer method, membrane spanning molecules like integrin $\alpha_{\text{Ib}}\beta_3$ can only be added via vesicle fusion requiring first a suitable surface attachment of the polymer as discussed above.

Adding Functionality to the Polymer

As outlined in Section 2.5 on page 48 the use of thermoresponsive or chemoresponsive polymers will allow locally varying properties which can lead to induced or inhibited binding. So far the problem for thermoresponsive polymers exhibiting a LCST is the

observation in the confined geometry. The low contrast between water and polymer and the counteracting change in thickness make the observation of a change in polymer layer thickness using ellipsometry or X-ray reflectivity almost impossible. Here, methods which employ a macroscopic probe like reflection interference contrast microscopy with a bead of defined size offer a higher sensitivity. An alternative detection method is photonic force microscopy where the bead position can be traced with higher temporal and spatial resolution¹⁴³.

Understanding the Physical Origin of Stripe Pattern Formation

A basic agreement has been found between the experiments and the description via the Cahn–Hilliard equation. Though no quantitative description based on fundamental physical concepts is present. On the phenomenological level the Cahn–Hilliard equation has to be extended with the aim of providing the same initial growth stage with an exponent of $\beta \approx 0.8$. A possible addition is the consideration of the shear induced onto the monolayer by the LB transfer¹⁴⁴. A more fundamental approach is the consideration of the implications of the observed form of the meniscus including a kink. The expected change in conformal space of the polymers has to be considered on a more detailed level.

APPENDIX A

EII SOFTWARE

For the evaluation of ellipsometry measurements the software EII was written. It uses the Abelès matrix formalism as outlined in Chapter 1. On the following pages the manual accompanying the software is presented. The software itself is attached to this document although a more recent version might be available.

- ◆ Installer for Windows
- ◆ Disk Image for Mac OS

The definition of the optical quantities used in EII follows the Nebraska convention. This is notably different to the definition of the incident angle Θ_{in} used in this thesis where the reference is the substrate plane (cf. Equations (1.22) on page 19 and (A.3)).



Ell Manual

Peter C. Seitz

July 24, 2009

Version 0.25

Ell - Ellipsometry analysis software

Copyright ©2009 Peter C. Seitz

This program is free software: you can redistribute it and/or modify it under the terms of the GNU General Public License as published by the Free Software Foundation, either version 3 of the License, or (at your option) any later version.

This program is distributed in the hope that it will be useful, but WITHOUT ANY WARRANTY; without even the implied warranty of MERCHANTABILITY or FITNESS FOR A PARTICULAR PURPOSE. See the GNU General Public License for more details.

You should have received a copy of the GNU General Public License along with this program. If not, see <http://www.gnu.org/licenses/>.

A.1 WHAT ELL CAN BE USED FOR

Ell calculates the ellipsometric angles Ψ and Δ for given layer models using the Abelès matrix formalism. It can perform least square fitting for up to two model parameters and can calculate maps of a function of merit (χ^2 maps) for those parameters. Layer models can be saved for later use and loaded into Ell.

A.2 INSTALLATION

Ell comes as an executable installer for Microsoft® Windows and as a Disk Image for Mac OS™. A prerequisite is a Igor Pro 6 (or newer) installation which will be checked during the installation. Ell makes use of the XMLutils which can be obtained from <http://www.igorexchange.com/project/XMLutils>. Alternatively the user can choose to install XMLutils 5.04 during the installation process of Ell.

A.3 LOADING DATA

To load data measured with an ellipsometer from a file into Ell, select in the Menu (see Figure A.1) Ell→Load Ellipsometric Data... Further datasets can be loaded using the Load Data button in the Ellipsometry Panel (see Figure A.2) or again via the Ell menu. Upon loading you will be prompted for the wavelength used to measure the data. The default value is 6328 Å. The dataset will be assigned a name close to the name of the file it is loaded from. If the first character is a number an 'X' will be prefixed. The total length is limited to 27 characters. If a dataset name is already in use the data will not be loaded and the message "This file has already been loaded. It is stored in the datafolder: ..." appears.

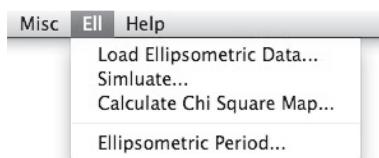


Figure A.1 – Ell Menu added to the Menu of Igor Pro.

Data saved from the Multiskop by Optrel can be loaded. If a kinetic measurement is detected, you will be asked for the angle of incidence used in this measurement since this information is not contained in the file written by the Multiskop control software.

In case an unsupported file is opened the loading process will be canceled with an error message.

If more than one dataset is loaded you can select the dataset to work with in the drop down menu in the Ellipsometry Panel. In the lower part of the Ellipsometry Panel the data will be shown in a graph Ψ versus Δ as shown in Figure A.2.

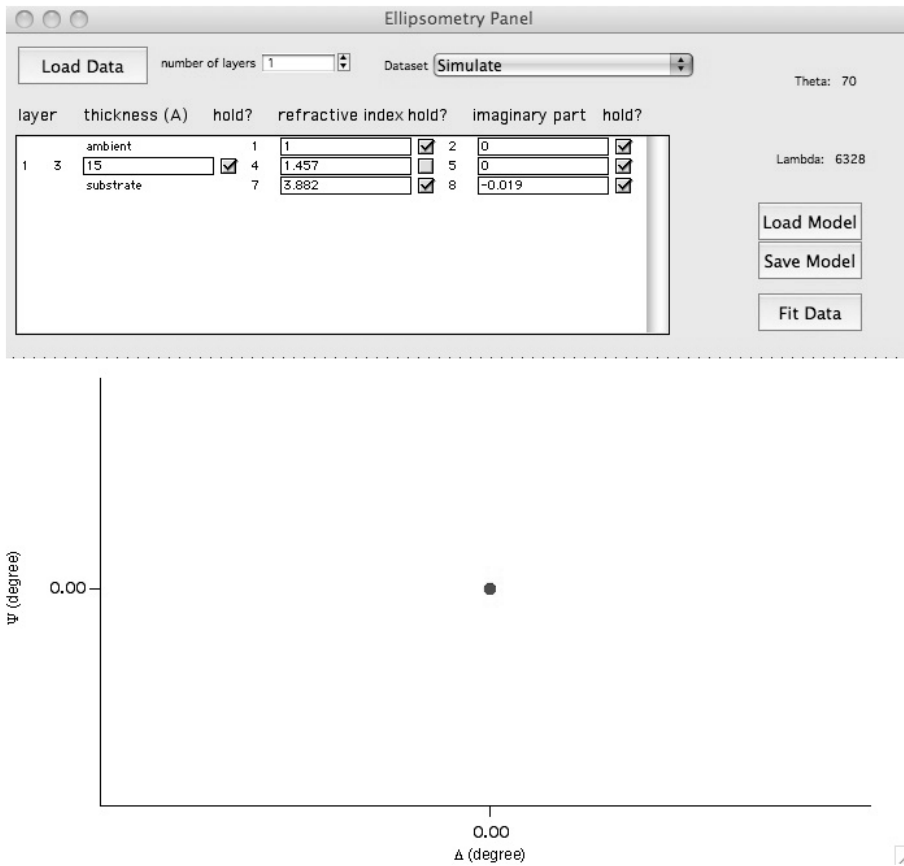


Figure A.2 – Ell Ellipsometry Panel with dataset named Simulate and corresponding layer model with one layer. Incident angle $\Theta = 70^\circ$ and wavelength $\lambda = 6328 \text{ \AA}$ are displayed in the right upper part.

A.4 LAYER MODELS

Layer models are displayed in the upper half of the Ellipsometry panel and are specific to the dataset selected. First the appropriate number of layers has to be set. Zero layers means only ambient medium and subphase are present. Each layer is characterized by a thickness d , real refractive index n and absorption coefficient k . The ambient medium and substrate fill the half space above and below the interfaces of the system and have no variable thickness.

Behind every entry a check box indicates whether this value should be kept fixed as a property of the system () or should be fitted as a parameter (). In Figure A.2 only the real refractive index of layer 1 is a parameter, all other values are fixed properties of the model.

Refractive indices are entered in the form $n + ik$, e.g. $3.882 - i0.019$ has to be entered as 3.882 and -0.019 . Thicknesses are all in Å. Every entry has to be filled. In case the value is expected to be zero, 0 has to be entered. Layer models can be saved using the Save Model button on the Ellipsometry Panel. Likewise a previously stored model can be loaded using the Load Model button.

A.5 FITTING DATA

To fit ellipsometric data, a dataset has to be selected and a layer model entered. When all entries are checked, the values of Ψ and Δ for this model are calculated upon pressing the Fit Data button and added as green squares to the Ψ versus Δ graph. Up to two entries can be unchecked to perform a minimization using the Levenberg–Marquardt algorithm on the function of merit

$$S(p_1, p_2) = (\Delta_{\text{Meas}} - \Delta_{\text{Model}})^2 + (\psi_{\text{Meas}} - \psi_{\text{Model}})^2. \quad (\text{A.1})$$

The values displayed in the Ellipsometry panel for the fitted parameters are the average over all data in the dataset. The values for each data point are stored in the wave fit_Coef in the datafolder named after the dataset.

A.6 SIMULATION

Calculation of ellipsometric angles without experimental data is possible by selecting Simulate... from the Ell menu. If no data has been loaded so far, the Ellipsometry panel will be displayed and you will be asked for the wavelength and incident angle to be used for the simulation. After entering these values a layer model can be entered. For the simulation any property or parameter of the layer model can be chosen and varied over

a user defined range. The values of Ψ and Δ for this variation using the displayed model are calculated and added as a black line to the Ψ versus Δ graph.

A.7 CALCULATING CHI SQUARE MAPS

A systematic variation of parameters and visualization of the effect on the ellipsometric angles can be done by calculating χ^2 maps. χ^2 is defined by the function of merit

$$\chi^2(p_1, p_2) = \frac{(\Delta_{\text{Meas}} - \Delta_{\text{Model}})^2}{\Delta_{\text{Model}}} + \frac{(\Psi_{\text{Meas}} - \Psi_{\text{Model}})^2}{\Psi_{\text{Model}}}. \quad (\text{A.2})$$

To calculate a χ^2 -square map use Ell→Calculate Chi Square Map.... A dialog asking for which parameters to use and start and stop values is presented. The calculation takes some time. A new image showing the result is displayed and updated during calculation. The scaling is set to show data from the minimum to twice the minimum value.

A.8 ELLIPSOMETRIC PERIOD

The measurement of Ψ and Δ is unambiguous up to an offset in layer thickness. Addition of a whole-number multiple of the thickness D to the film thickness results in the same values for Ψ and Δ . The thickness D is called the ellipsometric period and is given by

$$D = \frac{1}{2} \frac{\lambda}{\sqrt{n_j^2 - n_o^2 \sin^2 \Theta}} \quad (\text{A.3})$$

with the refractive index n_j of the film, the refractive index of the ambient medium n_o and the angle of incidence Θ of the light with wavelength λ . When choosing Ellipsometric Period... you will be asked for those four parameters. Upon providing them and pressing Continue the value for D will be printed to the history of the command window.

APPENDIX B

NEUTRON REFLECTIVITY AT THE GAS–SOLID INTERFACE

To complement X-ray reflectivity measurements, neutron reflectivity was used. The theoretical background and measurement technique are the same as in the case of X-ray reflectivity which is discussed in Section 1.3 on page 11. Instead of electromagnetic waves, neutrons with a certain kinetic energy are regarded as matter waves with a wavelength given by the de Broglie equation

$$\lambda = \frac{h}{p}. \quad (\text{B.1})$$

The wavelength λ is associated with the particle, $h = 6.626 \times 10^{-34} \text{ m}^2 \text{ kg s}^{-1}$ is the Planck constant and p the momentum of the particle.

The measurements were carried out at the D17 beamline of the Institut Laue–Langevin (ILL, Grenoble, France) in Time-of-Flight (TOF) mode. Due to the smaller flux available compared to X-ray reflectivity the sample size was much bigger. Silicon blocks with $5 \text{ cm} \times 8 \text{ cm}$ were used as substrates. The blocks were obtained with a polished surface and native oxide from Siliciumbearbeitung Andrea Holm (Tann, Germany). Prior to use they were cleaned using the same procedure as for all other solid substrates.

Samples with 0.5 mol % of PMOx₁₄ and PMOx₁₀₄ were measured. Analogous to the ellipsometry and X-ray measurements first the LB transferred monolayer was measured in air. The resulting reflectivity curve shown in Figure B.1 on the next page is free of features in the accessible range of q_z due to the small thickness of the collapsed polymers and the lipid monolayer.

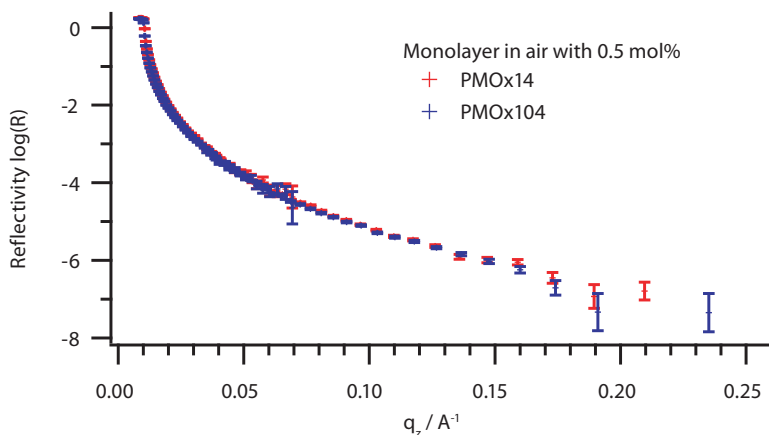


Figure B.1 – Neutron reflectivity curve of a monolayer doped with 0.5 mol % PMOx14 (red) or PMOx104 (blue) on silicon substrate. The reflectivities show no features and are almost identical.

After this measurement the completion to a bilayer was done by vesicle fusion with small unilamellar vesicles of SOPC prepared in D₂O. After incubating for one hour at room temperature the sample was rinsed with D₂O. The measurement geometry is reversed compared to X-ray reflectivity as shown in the inset of Figure B.2 on the facing page with the beam being reflected from the substrate side. The reflectivity curves are displayed in Figure B.2 on the next page. The data was analyzed using MOTOFIT⁸² running on Igor Pro. A three box model was sufficient to model the data. The oxide layer thickness and roughness was determined by previous ellipsometric and X-ray reflectivity measurement to be $d_{\text{SiO}_2} = 10.0 \text{ \AA}$ and $\sigma_{\text{PMOx14}} = 5.1 \text{ \AA}$, $\sigma_{\text{PMOx104}} = 5.7 \text{ \AA}$. The modeling of the membrane as a single layer leads to an underestimation of its thickness²⁷. Using a model with five layers a thickness of 46 Å is obtained for the SOPC lipid bilayer. The best fitting parameters are listed in Table B.1 on the facing page for a co-fitting of the datasets. Parameters except the ones defining the polymer layer and the roughnesses were linked and/or fixed during the fit. The independent parameters for the two samples are separated by a comma where the first value refers to PMOx14 and the second to PMOx104. No significant change due to the length of the polymer can be seen. Clearly a layer hydrated with D₂O between membrane and substrate is present. An accurate determination of its thickness on the contrary is not possible as the resolution of the data is limited. The neutron reflectivity measurements can therefore be taken as a support to the X-ray reflectivity measurements. It can however not be taken as an independent proof of a particular model since the almost featureless reflectivity curves support a multitude of models. A few scenarios can be excluded,

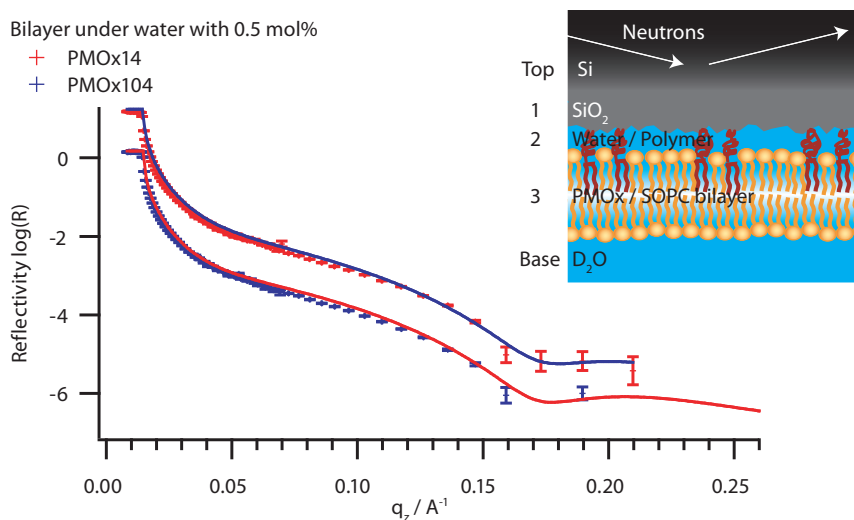


Figure B.2 – Neutron reflectometry of a SOPC bilayer doped with 0.5 mol % of PMOx14 (red, upper curve) or PMOx104 (blue, lower curve) in the proximal leaflet on silicon substrate. The best fitting model is overlaid as a solid line, parameters forming the model are compiled in Table B.1. The experimental geometry is sketched in the upper right. The neutrons impinge on the sample through the silicon substrate.

Table B.1 – Best fit results for bilayers under water with 0.5 mol % of PMOx14 or PMOx104. Entries with two values indicate the value for PMOx14 before the comma and the value for PMOx104 after the comma.

Layer	$d / \text{Å}$	$\rho / 10^{-6} \text{Å}^{-2}$	Solvent penetration / %	$\sigma / \text{Å}$
D ₂ O	∞	6.36	0	
Lipid Bilayer	40.0	0.12	0	9.0, 9.5
Polymer	6.4, 8.8	2.50, 2.40	95, 83	5.0, 1.0
SiO ₂	10.0	3.47	0	5.1, 5.7
Si	∞	2.07	0	9.5

most notably the presence of a thick hydrated polymer layer underneath a lipid bilayer membrane. This is in contradiction to the separation distances reported by fluorescent interference contrast (FLIC) microscopy¹⁴⁵ of several nanometers²⁴. Taking a closer look at the experimental method of FLIC, several problems become apparent. First, the expected uncertainties for the determination of distances in FLIC microscopy amount easily to several nanometres most notably entering through the aperture used for excitation and detection but also through the assumptions made for the refractive indices¹⁴⁶. Second, as presented by Kiessling & Tamm⁴⁸ the same result of a collapsed polymer layer as found in this thesis can be obtained by FLIC microscopy but has in this case been discarded in favor of a thick polymer layer found by a less reliable measurement based on four data points instead of sixteen data points used where the collapsed polymer layer was observed. The values reported by Purucker *et al.*²⁴ were obtained from measurements on a sixteen terraced support with the bilayer doped by 0.5 mol % 1,1'-dioctadecyl-3,3,3',3'-tetramethylindocarbocyanine (DiI)(unpublished results). The orientation of the transition dipole of the dye was assumed to be at 62° to the membrane normal whereas Axelrod¹⁴⁷ reported an orientation of 90° to the membrane normal. Putting these doubts of a sound analysis of the FLIC measurements against the body of evidence provided by the three herein presented measurement techniques, the strongly favored interpretation is that of a collapsed polymer layer underneath a supported bilayer for low polymer concentrations.

APPENDIX C

CAHN–HILLIARD EQUATION

The Cahn–Hilliard equation follows from the description of diffusive processes in a binary mixture. In contrast to the diffusion equation, the driving force for mass flux is not a different concentration of species but a different chemical potential which depends on the local concentration of the two components and the concentration gradient. The diffusion equation is obtained as a special case where the chemical potential depends only on the local concentration. In the following section we derive the Cahn–Hilliard equation and perform a linear stability analysis on it. The presentation follows Eck *et al.*¹⁴⁸ and Anthony & Jones¹⁴⁹.

C.1 DERIVATION

We assume a binary mixture with the concentrations of the components denoted by c_1 and c_2 . We require the system to be **isobar** and **isotherm** in an area $\Omega \subset \mathbb{R}^d$. Then the change in concentration over time is equal to the change in flux over space

$$\partial_t c_i + \nabla \cdot \mathbf{j}_i = 0, \quad i = 1, 2. \quad (\text{C.1})$$

We assume the amount of molecules of each species is conserved, i.e.,

$$\langle c_i \rangle = \frac{1}{\Omega} \int_{\Omega} c_i \, dx = \text{const.}, \quad i = 1, 2. \quad (\text{C.2})$$

As we consider a binary system we require the sum of the fluxes of the two components to result in no net flux ($\mathbf{j}_1 + \mathbf{j}_2 = 0$) to ensure the system is isobaric ($\partial_t(c_1 + c_2) = 0$).

Now we can reduce the system to the independent variables

$$c = c_1 - c_2 \text{ and } \mathbf{j} = \mathbf{j}_1 - \mathbf{j}_2. \quad (\text{C.3})$$

With c now ranging from -1 (pure component 2) to 1 (pure component 1). The free energy is of the form $\int_{\Omega} f(c) dx$, the integral over the energy density $f(c)$ in the considered space. Material is now driven by a gradient in the free energy density, given by the first derivative of the free energy density with respect to concentration $f'(c) \equiv \frac{\partial f}{\partial c}$. This gradient results in a flux \mathbf{j} proportional to it by a factor L , $\mathbf{j} = -L\nabla \frac{\partial f}{\partial c}$, where $L \geq 0$ is the mobility (Fick's first law). Inserting into Equation (C.1), we obtain

$$\partial_t c + \nabla(-L\nabla f'(c)) = 0. \quad (\text{C.4})$$

which is closely related to the diffusion equation (Fick's second law) with the difference of being driven by the free energy density gradient instead of composition. The mobility L is the Onsager coefficient. The behavior of Equation (C.4) depends on the form of the free energy density $f(c)$. For a convex ($f''(c) > 0$) free energy density, diffusion moves material from areas with high concentration to areas of low concentration. For a concave ($f''(c) < 0$) free energy density we obtain 'uphill' diffusion where mass moves from areas with low concentration to areas with high concentration. Solutions to this case do not depend continuously on the initial conditions and for non convex energy densities $f(c)$ the equation is in general not solvable. This counterintuitive case of diffusion can be explained by not looking at the concentration but at the free energy density gradient $f'(c)$ which needs to be minimized.

Separating the two molecular components gives rise to an additional contribution which is associated with the interface between the domains of the components. The energy depends on how sharp this interface is. This addition results in a dependency of the local free energy on the local concentration c and the local composition gradient ∇c . From a Taylor expansion series of the free energy per molecule in a solution of uniform composition c , Cahn & Hilliard¹³³ obtained as the lowest order the square of the gradient $|\nabla c|^2$. This can be also understood from the fact that the free energy density $f(c)$, which is scalar, must be invariant to the direction of the gradient. Therefore only even powers can occur of which the lowest is the second. This formulation of the free energy has been used by van der Waals for studying the liquid-gas interface, Landau and Ginzburg in the context of magnetic domain walls and by Cahn & Hilliard to describe interfaces in metals. The free energy is given by

$$\mathcal{F}(c) = \int_{\Omega} \left(f(c) + \frac{\gamma}{2} |\nabla c|^2 \right) dx \text{ with } \gamma > 0 \text{ constant.} \quad (\text{C.5})$$

The constant γ is denoted the gradient energy coefficient. First we look at the change

in free energy caused by an infinitesimal change in concentration δc

$$\begin{aligned}\delta\mathcal{F}(c) &= \int_{\Omega} \left(f(\delta c) + \frac{\gamma}{2} |\nabla(\delta c)|^2 \right) dx \\ &= \int_{\Omega} \left[\left(f'(c)\delta c + \frac{1}{2}f''(c)\delta c^2 \right) + \frac{\gamma}{2} \left((\nabla c)(\nabla\delta c) + (\nabla\delta c)(\nabla c) + (\nabla\delta c)^2 \right) \right] dx.\end{aligned}\quad (\text{C.6})$$

This corresponds to a Taylor expansion around a concentration c_o , with $c = c_o + \delta c$ and subtracting the contribution of the constant concentration c_o . Dropping orders higher than one in δc , we get

$$\delta\mathcal{F}(c) = \int_{\Omega} (f'(c)\delta c + \gamma((\nabla c)(\nabla\delta c))) dx. \quad (\text{C.7})$$

Integration by parts of the second term gives

$$\delta\mathcal{F}(c) = \int_{\Omega} (f'(c) - \gamma(\nabla^2 c)) (\delta c) dx \quad (\text{C.8})$$

from which we get the chemical potential μ

$$\mu = \frac{\delta\mathcal{F}(c)}{\delta c(\mathbf{r})} = -\gamma\nabla^2 c + f'(c). \quad (\text{C.9})$$

Using Equations (C.4, C.9) it follows the Cahn–Hilliard equation

$$\partial_t c = \nabla L \nabla (-\gamma\nabla^2 c + f'(c)). \quad (\text{C.10})$$

One can see that when dropping the gradient term $\gamma\nabla^2 c$, Equation (C.4) is recovered. An effective diffusion coefficient D_{eff} can be defined by $D_{\text{eff}} = Lf''(c)$.

C.2 LINEAR STABILITY ANALYSIS

In the following we consider $f(c)$ to be the non convex double well potential (see Figure C.1)

$$f(c) = \alpha(c^2 - 1)^2, \alpha \in \mathbb{R}_+ \quad (\text{C.11})$$

in the area $\Omega = [0, l]^d$, $l > 0$. We consider homogeneous stationary solutions

$$c \equiv c_m, c_m \in \mathbb{R} \quad (\text{C.12})$$

with

$$f''(c_m) < 0. \quad (\text{C.13})$$

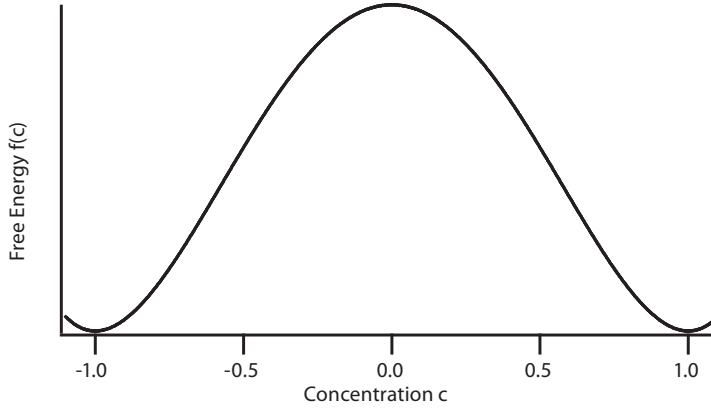


Figure C.1 – Free Energy $f(c)$ as given by Equation (C.11). c is defined in Equation (C.3), $c = -1$ corresponds to pure component 2 whereas $c = 1$ corresponds to pure component 1. An instability emerges for concentrations between the inflection points located at $c = \sqrt{1/3}$ and $c = -\sqrt{1/3}$.

Small fluctuations $c = c_m + u$ with $\int_{\Omega} u \, dx = 0$ to conserve the total mass can lead to development of spatial structures. Now we linearize Equation (C.10) around c_m and get the linearized Cahn–Hilliard equation

$$\partial_t u = -L(\nabla^2)(\gamma \nabla^2 u - f''(c_m)u). \quad (\text{C.14})$$

This can be solved by

$$u(t, \mathbf{x}) = \sum_{k \in \frac{2\pi}{L} \mathbb{Z}^d \setminus \{0\}} e^{\lambda_k t} e^{i\mathbf{k} \cdot \mathbf{x}} \quad (\text{C.15})$$

with the Eigenvalues

$$\lambda_k = L|k|^2(-\gamma|k|^2 - f''(c_m)), \quad (\text{C.16})$$

shown in Figure C.2. The maximum of Equation (C.16) is located at $k = \sqrt{\frac{-f''(c_m)}{\gamma}}$. This wave vector is most strongly amplified and dominates the observed spectrum. The most unstable wavelength $\bar{l} = 2\pi/|k|$ is for $f''(c_m) < 0$ given by

$$\bar{l} = 2\pi \sqrt{-\frac{2\gamma}{f''(c_m)}}. \quad (\text{C.17})$$

We expect to find spatial structures on this length scale. Of course the area Ω has to be large enough to support this wavenumber. Finally we summarize the dimensions of the parameters and variables occurring in the Cahn–Hilliard equation in Table C.1.

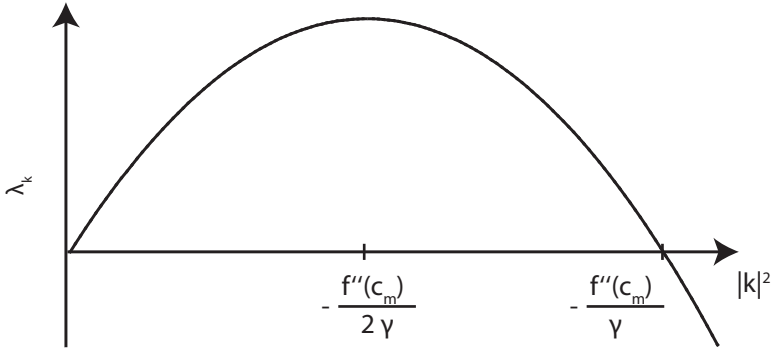


Figure C.2 – Eigenvalues λ_k as a function of the squared wavenumber $|k|^2$.

Table C.1 – Dimensions of the quantities involved in the Cahn–Hilliard equation and the linear stability analysis.

Quantity	Description	Dimension
x	Spatial coordinate	L
t	Time	T
c	Concentration	
L	Mobility (Onsager coefficient)	$M^{-1} T^1$
γ	Gradient energy coefficient	$M L^4 T^{-2}$
f	Free energy	$M L^2 T^{-2}$
f'	1 st derivative of the free energy	$M L^2 T^{-2}$
f''	2 nd derivative of the free energy	$M L^2 T^{-2}$
λ	Eigenvalues	T^{-1}
k	Wave vector	L^{-1}
α	Free energy parameter	$M L^2 T^{-2}$

REFERENCES

- [1] ERWIN SCHRÖDINGER. *Was ist Leben?* Piper, München, 1987. ISBN 978-3-492-03122-6. page 1.
- [2] BRUCE ALBERTS, ALEXANDER JOHNSON, JULIAN LEWIS, MARTIN RAFF, KEITH ROBERTS & PETER WALTER. *Molecular biology of the cell*. Garland, New York, 2002. ISBN 0-8153-3218-1. page 1.
- [3] JEREMY M. BERG, JOHN L. TYMOCZKO & LUBERT STRYER. *Biochemistry*. W. H. Freeman, sixth edition, 2006. ISBN 978-0716787242. page 1.
- [4] CHARLES TANFORD. *The hydrophobic effect and the organization of living matter*. *Science*, 200(4345), 1012–1018, 1978. doi:10.1126/science.653353. page 1.
- [5] MARIANA RUIZ VILLARREAL. *Cell membrane detailed diagram*. 2007. http://commons.wikimedia.org/wiki/File:Cell_membrane_detailed_diagram_en.svg Accessed 21. September 2009. page 2.
- [6] DETLEV DRENCKHAHN & WOLFGANG ZENKER, editors. *Benninghoff Anatomie*, volume 1. Urban & Schwarzenberg, 15th edition, 1994. ISBN 3-541-00245-X. page 2.
- [7] S. JONATHAN SINGER & GARTH L. NICOLSON. *The fluid mosaic model of the structure of cell membranes*. *Science*, 175(4023), 720–731, 1972. doi:10.1126/science.175.4023.720. page 2.
- [8] KEN JACOBSON, ERIN D. SHEETS & RUDOLF SIMSON. *Revisiting the fluid mosaic model of membranes*. *Science*, 268(5216), 1441–1442, 1995. doi:10.1126/science.7770769. page 2.
- [9] KEN JACOBSON, OLE G. MOURITSEN & RICHARD G. W. ANDERSON. *Lipid rafts: at a crossroad between cell biology and physics*. *Nature Cell Biology*, 9(1), 7–14, 2007. doi:10.1038/ncbo107-7. page 2.
- [10] FREDERICK R. MAXFIELD. *Plasma membrane microdomains*. *Current Opinion in Cell Biology*, 14(4), 483–487, 2002. doi:10.1016/S0955-0674(02)00351-4. page 2.
- [11] PAUL MUELLER, DONALD O. RUDIN, H. TI TIEN & WILLIAM C. WESCOTT. *Reconstitution of cell membrane structure in vitro and its transformation into an excitable system*. *Nature*, 194(4832), 979–980, 1962. doi:10.1038/194979a0. page 2.
- [12] RICHARD E. PAGANO & THOMAS E. THOMPSON. *Spherical lipid bilayer membranes*. *Biochimica et Biophysica Acta - Lipids and Lipid Metabolism*, 144(3), 666–669, 1967.

- doi:10.1016/0005-2760(67)90055-0. page 2.
- [13] IRVING LANGMUIR. *The constitution and fundamental properties of solids and liquids. II. liquids.* *Journal of the American Chemical Society*, 39(9), 1848–1906, 1917. doi:10.1021/ja02254a006. page 2.
- [14] BERT SAKMANN & ERWIN NEHER, editors. *Single-Channel Recording*. Springer, 2nd edition, 2007. ISBN 978-0306448706. page 2.
- [15] LUKAS K. TAMM & HARDEN M. MCCONNELL. *Supported phospholipid bilayers.* *Biophysical Journal*, 47(1), 105–113, 1985. doi:10.1016/S0006-3495(85)83882-0. page 2.
- [16] MARCEL BENZ, THOMAS GUTSMANN, NIANHUAN CHEN, RAFAEL TADMOR & JACOB N. ISRAELACHVILI. *Correlation of AFM and SFA measurements concerning the stability of supported lipid bilayers.* *Biophysical Journal*, 86(2), 870–879, 2004. doi:10.1016/S0006-3495(04)74162-4. page 2.
- [17] THOMAS M. BAYERL & MYER BLOOM. *Physical properties of single phospholipid bilayers adsorbed to micro glass beads. A new vesicular model system studied by 2H-nuclear magnetic resonance.* *Biophysical Journal*, 58(2), 357–362, 1990. doi:10.1016/S0006-3495(90)82382-1. page 2.
- [18] CHARLENE C. NG, YU-LING CHENG & PETER S. PENNEFATHER. *Properties of a self-assembled phospholipid membrane supported on lipobeads.* *Biophysical Journal*, 87(1), 323–331, 2004. doi:10.1529/biophysj.103.030627. page 2.
- [19] MICHAEL M. BAKSH, MICHAL JAROS & JAY T. GROVES. *Detection of molecular interactions at membrane surfaces through colloid phase transitions.* *Nature*, 427(6970), 139–141, 2004. doi:10.1038/nature02209. page 2.
- [20] ERICH SACKMANN. *Supported membranes: Scientific and practical applications.* *Science*, 271(5245), 43–48, 1996. doi:10.1126/science.271.5245.43. page 2.
- [21] BERND W. KÖNIG, S. KRUEGER, W. J. ORTS, CHARLES F. MAJKRZAK, NORM F. BERK, J. V. SILVERTON & KLAUS GAWRISCH. *Neutron reflectivity and atomic force microscopy studies of a lipid bilayer in water adsorbed to the surface of a silicon single crystal.* *Langmuir*, 12(5), 1343–1350, 1996. doi:10.1021/la950580r. pages 2 and 5.
- [22] ARASH GRAKOU, SHANNON K. BROMLEY, CENK SUMEN, MARK M. DAVIS, ANDREY S. SHAW, PAUL M. ALLEN & MICHAEL L. DUSTIN. *The immunological synapse: A molecular machine controlling T cell activation.* *Science*, 285(5425), 221–227, 1999. doi:10.1126/science.285.5425.221. page 2.
- [23] JEFFREY J. GRAY. *The interaction of proteins with solid surfaces.* *Current Opinion in Structural Biology*, 14(1), 110–115, 2004. doi:10.1016/j.sbi.2003.12.001. page 3.
- [24] OLIVER PURRUCKER, ANTON FÖRTIG, RAINER JORDAN, ERICH SACKMANN & MOTOMU TANAKA. *Control of frictional coupling of transmembrane cell receptors in model cell membranes with linear polymer spacers.* *Physical Review Letters*, 98, 078102, 2007. doi:10.1103/PhysRevLett.98.078102. pages 3 and 100.
- [25] STEFANIE GOENNENWEIN, MOTOMU TANAKA, BIN HU, LUIS MORODER & ERICH SACKMANN. *Functional incorporation of integrins into solid supported membranes on ultra-thin films of cellulose: Impact on adhesion.* *Biophysical Journal*, 85(1), 646–655, 2003.

- doi:10.1016/S0006-3495(03)74508-1. page 3.
- [26] MOTOMU TANAKA & ERICH SACKMANN. *Polymer-supported membranes as models of the cell surface*. *Nature*, 437(7059), 656–663, 2005. doi:10.1038/nature04164. page 3.
- [27] JOYCE Y. WONG, JAROSLAW MAJEWSKI, MARKUS SEITZ, CHAD K. PARK, JACOB N. ISRAELACHVILI & GREGORY S. SMITH. *Polymer-cushioned bilayers. I. A structural study of various preparation methods using neutron reflectometry*. *Biophysical Journal*, 77(3), 1445–1457, 1999. doi:10.1016/S0006-3495(99)76992-4. pages 3, 5, and 98.
- [28] GUNTER ELENDER, MARTIN KÜHNER & ERICH SACKMANN. *Functionalisation of Si/SiO₂ and glass surfaces with ultrathin dextran films and deposition of lipid bilayers*. *Biosensors and Bioelectronics*, 11(6-7), 565–577, 1996. doi:10.1016/0956-5663(96)83292-1. page 3.
- [29] MARTIN KÜHNER, ROBERT TAMPÉ & ERICH SACKMANN. *Lipid mono- and bilayer supported on polymer films: composite polymer-lipid films on solid substrates*. *Biophysical Journal*, 67(1), 217–226, 1994. doi:10.1016/S0006-3495(94)80472-2. page 3.
- [30] CHRISTIAN DIETRICH & ROBERT TAMPÉ. *Charge determination of membrane molecules in polymer-supported lipid layers*. *Biochimica et Biophysica Acta - Biomembranes*, 1238(2), 183–191, 1995. doi:10.1016/0005-2736(95)00129-Q. page 3.
- [31] HUBERT SIGL, GUNNAR BRINK, MICHAEL SEUFERT, M. SCHULZ, GERHARD WEGNER & ERICH SACKMANN. *Assembly of polymer/lipid composite films on solids based on hairy rod LB-films*. *European Biophysics Journal*, 25(4), 249–259, 1997. doi:10.1007/s002490050037. page 3.
- [32] HEIKO HILLEBRANDT, GERALD WIEGAND, MOTOMU TANAKA & ERICH SACKMANN. *High electric resistance polymer/lipid composite films on indium–tin–oxide electrodes*. *Langmuir*, 15(24), 8451–8459, 1999. doi:10.1021/la990341u. page 3.
- [33] MOTOMU TANAKA, AMY P. WONG, FLORIAN REHFELDT, MURAT TUTUS & STEFAN KAUFMANN. *Selective deposition of native cell membranes on biocompatible micropatterns*. *Journal of the American Chemical Society*, 126(10), 3257–3260, 2004. doi:10.1021/ja038981d. page 3.
- [34] MOTOMU TANAKA, STEFAN KAUFMANN, JULIA NISSEN & MARION HOCHREIN. *Orientation selective immobilization of human erythrocyte membranes on ultrathin cellulose films*. *Physical Chemistry Chemical Physics*, 3(18), 4091–4095, 2001. doi:10.1039/b105007a. page 3.
- [35] MOTOMU TANAKA. *Polymer-supported membranes: Physical models of cell surfaces*. *MRS Bulletin*, 31, 513–520, 2006. page 3.
- [36] N. BUNJES, E. K. SCHMIDT, A. JONCZYK, F. RIPPMANN, D. BEYER, HELMUT RINGSDORF, P. GRABER, WOLFGANG KNOLL. & RENATE NAUMANN. *Thiopeptide-supported lipid layers on solid substrates*. *Langmuir*, 13(23), 6188–6194, 1997. doi:10.1021/la970317l. page 4.
- [37] HOLGER LANG, CLAUS DUSCHL & HORST VOGEL. *A new class of thiolipids for the attachment of lipid bilayers on gold surfaces*. *Langmuir*, 10(1), 197–210, 1994. doi:10.1021/la00013a029. page 4.
- [38] B. A. CORNELL, V. L. B. BRAACH-MAKSVYTIS, L. G. KING, P. D. J. OSMAN, B. RAGUSE, L. WIECZOREK & R. J. PACE. *A biosensor that uses ion-channel switches*. *Nature*, 387(6633),

- 580–583, 1997. doi:10.1038/42432. page 4.
- [39] DUNCAN J. MCGILLIVRAY, GINTARAS VALINCIUS, DAVID J. VANDERAH, WILMA FEBOAYALA, JOHN T. WOODWARD, FRANK HEINRICH, JOHN J. KASIANOWICZ & MATHIAS LÖSCHE. *Molecular-scale structural and functional characterization of sparsely tethered bilayer lipid membranes*. *Biointerphases*, 2(1), 21–33, 2007. doi:10.1116/1.2709308. pages 4, 5, and 48.
- [40] MICHAEL L. WAGNER & LUKAS K. TAMM. *Reconstituted syntaxin1A/SNAP25 interacts with negatively charged lipids as measured by lateral diffusion in planar supported bilayers*. *Biophysical Journal*, 81(1), 266–275, 2001. doi:10.1016/S0006-3495(01)75697-4. page 4.
- [41] MICHAEL L. WAGNER & LUKAS K. TAMM. *Tethered polymer-supported planar lipid bilayers for reconstitution of integral membrane proteins: Silane-polyethyleneglycol-lipid as a cushion and covalent linker*. *Biophysical Journal*, 79(3), 1400–1414, 2000. doi:10.1016/S0006-3495(00)76392-2. pages 4 and 69.
- [42] LISA Y. HWANG, HEIDE GÖTZ, WOLFGANG KNOLL, CRAIG J. HAWKER & CURTIS W. FRANK. *Tethered lipid bilayers on benzophenone-modified substrates*. *Langmuir*, 24, 14088–14098, 2008. doi:10.1021/la8022997. pages 4 and 5.
- [43] WILLIAM W. SHEN, STEVEN G. BOXER, WOLFGANG KNOLL & CURTIS W. FRANK. *Polymer-supported lipid bilayers on benzophenone-modified substrates*. *Biomacromolecules*, 2(1), 70–79, 2001. doi:10.1021/bm005581z. page 4.
- [44] CHRISTOPH A. NAUMANN, O. PRUCKER, T. LEHMANN, J. RUHE, WOLFGANG KNOLL & CURTIS W. FRANK. *The polymer-supported phospholipid bilayer: Tethering as a new approach to substrate—membrane stabilization*. *Biomacromolecules*, 3(1), 27–35, 2002. doi:10.1021/bm0100211. page 4.
- [45] ANTON FÖRTIG, RAINER JORDAN, KARLHEINZ GRAF, GIOVANNI SCHIAVON, OLIVER PURRUCKER & MOTOMU TANAKA. *Solid-supported biomimetic membranes with tailored lipopolymer tethers*. *Macromolecular Symposia*, 210, 329–338, 2004. doi:10.1002/masy.200450637. pages 4, 5, and 8.
- [46] OLIVER PURRUCKER, ANTON FÖRTIG, RAINER JORDAN & MOTOMU TANAKA. *Supported membranes with well-defined polymer tethers — incorporation of cell receptors*. *ChemPhysChem*, 5, 327–335, 2004. doi:10.1002/cphc.200300863. pages 4, 8, 24, 25, 48, and 53.
- [47] C. H. CHEN, J. WILSON, W. CHEN, R. M. DAVIS & J. S. RIFFLE. *A light-scattering study of poly(2-alkyl-2-oxazoline)s: Effect of temperature and solvent type*. *Polymer*, 35(17), 3587–3591, 1994. doi:10.1016/0032-3861(94)90532-0. page 4.
- [48] VOLKER KIESSLING & LUKAS K. TAMM. *Measuring distances in supported bilayers by fluorescence interference-contrast microscopy: Polymer supports and SNARE proteins*. *Biophysical Journal*, 84(1), 408–418, 2003. doi:10.1016/S0006-3495(03)74861-9. pages 5 and 100.
- [49] CHRISTOPH STRIEBEL, ANDREAS BRECHT & GÜNTER GAUGLITZ. *Characterization of biomembranes by spectral ellipsometry, surface plasmon resonance and interferometry with regard to biosensor application*. *Biosensors and Bioelectronics*, 9(2), 139–146, 1994. doi:10.1016/0956-5663(94)80105-3. page 5.

- [50] GERTRUD PUU & INGA GUSTAFSON. *Planar lipid bilayers on solid supports from liposomes — factors of importance for kinetics and stability*. *Biochimica et Biophysica Acta - Biomembranes*, 1327(2), 149–161, 1997. doi:10.1016/S0005-2736(97)00052-7. page 5.
- [51] MICHAEL C. HOWLAND, ALAN W. SZMODIS, BABAK SANII & ATUL N. PARIKH. *Characterization of physical properties of supported phospholipid membranes using imaging ellipsometry at optical wavelengths*. *Biophysical Journal*, 92, 1306–1317, 2007. doi:10.1529/biophysj.106.097071. page 5.
- [52] JOHN KATSARAS & THOMAS GUTBERLET, editors. *Lipid bilayers: Structure and interactions*. Biological physics series. Springer, 2001. ISBN 978-3540675556. page 5.
- [53] CHAD E. MILLER, JAROSLAW MAJEWSKI, THOMAS GOG & TONYA L. KUHL. *Characterization of biological thin films at the solid-liquid interface by X-ray reflectivity*. *Physical Review Letters*, 94, 238104, 2005. doi:10.1103/PhysRevLett.94.238104. pages 5 and 16.
- [54] EVA NOVÁKOVÁ, KLAUS GIEWEKEMEYER & TIM SALDITT. *Structure of two-component lipid membranes on solid support: An X-ray reflectivity study*. *Physical Review E*, 74, 051911, 2006. doi:10.1103/PhysRevE.74.051911. pages 5 and 16.
- [55] MARION B. HOCHREIN, CHRISTIAN REICH, BÄRBEL KRAUSE, JOACHIM O. RÄDLER & BERT NICKEL. *Structure and mobility of lipid membranes on a thermoplastic substrate*. *Langmuir*, 22(2), 538–545, 2006. doi:10.1021/la051820y. page 5.
- [56] TONYA L. KUHL, JAROSLAW MAJEWSKI, JOYCE Y. WONG, S. STEINBERG, DEBORAH E. LECKBAND, JACOB N. ISRAELACHVILI & GREGORY S. SMITH. *A neutron reflectivity study of polymer-modified phospholipid monolayers at the solid-solution interface: Polyethylene glycol-lipids on silane-modified substrates*. *Biophysical Journal*, 75(5), 2352–2362, 1998. doi:10.1016/S0006-3495(98)77679-9. page 5.
- [57] HERMAN FRANCIS MARK, NORBERT M. BIKALES, CHARLES G. OVERBERGER, JACQUELINE I. KROCHWITZ & GEORG MENGES. *Encyclopedia of polymer science and engineering*, volume 1. Wiley, 2nd, revised, illustrated edition, 1989. ISBN 0471895407. page 5.
- [58] RAINER JORDAN, KARLHEINZ GRAF, HANS RIEGLER & KLAUS K. UNGER. *Polymer-supported alkyl monolayers on silica: Synthesis and self-assembly of terminal functionalized poly(N-propionylethylenimine)s*. *Chemical Communications*, (9), 1025–1026, 1996. doi:10.1039/CC9960001025. page 5.
- [59] RAINER JORDAN, KAI MARTIN, HANS JOACHIM RÄDER & KLAUS K. UNGER. *Lipopolymers for surface functionalizations. 1. Synthesis and characterization of terminal functionalized poly(N-propionylethylenimine)s*. *Macromolecules*, 34(26), 8858–8865, 2001. doi:10.1021/ma011573e. pages 5, 8, and 43.
- [60] PETER PERSIGHEHL, RAINER JORDAN & OSKAR NUYKEN. *Functionalization of amphiphilic poly(2-oxazoline) block copolymers: A novel class of macroligands for micellar catalysis*. *Macromolecules*, 33(19), 6977–6981, 2000. doi:10.1021/ma0007381. page 5.
- [61] STEPHEN WOLFRAM. *A New Kind of Science*. Wolfram Media, 2002. ISBN 1579550088. page 5.
- [62] SHAO-RAN R. REN & IAN W. HAMLEY. *Orientational correlations in stripe patterns*. *Physica B: Condensed Matter*, 322(1-2), 110–115, 2002. doi:10.1016/S0921-4526(02)00605-1. page 5.

- [63] OLIVER PURRUCKER, ANTON FÖRTIG, KARIN LÜDTKE, RAINER JORDAN & MOTOMU TANAKA. *Confinement of transmembrane cell receptors in tunable stripe micropatterns*. *Journal of the American Chemical Society*, 127, 1258–1264, 2005. doi:10.1021/ja045713m. page 5, 53, and 86.
- [64] REINHARD LIPOWSKY & ERICH SACKMANN, editors. *Structure and Dynamics of Membranes*, volume 1 of *Handbook of Biological Physics*. Elsevier Science Ltd, 1995. ISBN 978-0444819758. page 7.
- [65] RUMIANA KOYNOVA & MARTIN CAFFREY. *Phases and phase transitions of the phosphatidylcholines*. *Biochimica et Biophysica Acta - Reviews on Biomembranes*, 1376(1), 91–145, 1998. doi:10.1016/S0304-4157(98)00006-9. page 7.
- [66] H. LINDSEY, N. O. PETERSEN & SUNNEY I. CHAN. *Physicochemical characterization of 1,2-diphytanoyl-sn-glycero-3-phosphocholine in model membrane systems*. *Biochimica et Biophysica Acta - Biomembranes*, 555(1), 147–167, 1979. doi:10.1016/0005-2736(79)90079-8. page 7.
- [67] ALAN D. MCNAUGHT & ANDREW WILKINSON, editors. *IUPAC. Compendium of Chemical Terminology (the "Gold Book")*. Blackwell Scientific Publications, 2nd edition, 1997. doi:10.1351/goldbook. XML on-line corrected version: <http://goldbook.iupac.org> (2006-) created by M. Nic, J. Jirat, B. Kosata; updates compiled by A. Jenkins. pages 8 and 48.
- [68] WERNER KERN & DAVID A. PUOTINEN. *Cleaning solutions based on hydrogen peroxide for use in silicon semiconductor technology*. *RCA Review*, pp. 187–206, 1970. page 9.
- [69] IRVING LANGMUIR. *The mechanism of the surface phenomena of flotation*. *Transactions of the Faraday Society*, 15, 62–74, 1920. doi:10.1039/TF9201500062. page 9.
- [70] KATHARINE B. BLODGETT. *Films built by depositing successive monomolecular layers on a solid surface*. *Journal of the American Chemical Society*, 57(6), 1007–1022, 1935. doi:10.1021/ja01309a011. page 9.
- [71] EDWIN KALB, SAMMY FREY & LUKAS K. TAMM. *Formation of supported planar bilayers by fusion of vesicles to supported phospholipid monolayers*. *Biochimica et Biophysica Acta - Biomembranes*, 1103(2), 307–316, 1992. doi:10.1016/0005-2736(92)90101-Q. page 11.
- [72] ANNE L. PLANT. *Self-assembled phospholipid/alkanethiol biomimetic bilayers on gold*. *Langmuir*, 9(11), 2764–2767, 1993. doi:10.1021/la00035a004. page 11.
- [73] EUGENE HECHT. *Optics*. Addison Wesley, 4th edition, 2001. ISBN 978-0805385663. pages 11 and 18.
- [74] FLORIN ABELÈS. *La théorie générale des couches minces*. *Journal de Physique et le Radium*, 11(7), 307–309, 1950. doi:10.1051/jphysrad:01950001107030700. pages 12 and 13.
- [75] JAMES CLERK MAXWELL. *A treatise on electricity and magnetism*, volume 2. Oxford, Clarendon Press, 1st edition, 1873. doi:10.1184/OCLC/01540581. page 12.
- [76] RASHEED M. A. AZZAM & NICHOLAS M. BASHARA. *Ellipsometry and Polarized Light*. North Holland, 1st, corrected printing edition, 1987. ISBN 978-0444870162. page 13.
- [77] LYMAN G. PARRATT. *Surface studies of solids by total reflection of X-rays*. *Physical Review*, 95(2), 359–369, 1954. doi:10.1103/PhysRev.95.359. page 15.

- [78] P. CROCE & LOUIS NÉVOT. *Sur l'étude des couches superficielles monoatomiques par réflexion 'rasante' (spéculaire ou diffuse) de rayons X, par la méthode de l'empilement 'sandwich'*. *Journal of Applied Crystallography*, 8, 304–314, 1975. doi:10.1107/S0021889875010503. page 16.
- [79] R. D. DESLATTES, E. G. KESSLER JR., P. INDELICATO, L. DE BILLY, E. LINDROTH, J. ANTON, J. S. COURSEY, D. J. SCHWAB, C. CHANG, R. SUKUMAR, K. OLSEN & R. A. DRAGOSET. *X-ray transition energies (version 1.2)*. 2005. Available: <http://physics.nist.gov/XrayTrans> [2009, August 20]. National Institute of Standards and Technology, Gaithersburg, MD. Originally published as: R. D. Deslattes, E. G. Kessler, Jr., P. Indelicato, L. de Billy, E. Lindroth, and J. Anton, *X-ray transition energies: New approach to a comprehensive evaluation*. *Reviews of Modern Physics* 75, 35–99, 2003. page 16.
- [80] B. L. HENKE, E. M. GULLIKSON & J. C. DAVIS. *X-ray interactions: Photoabsorption, scattering, transmission, and reflection at $E = 50\text{--}30,000$ eV, $Z = 1\text{--}92$* . *Atomic Data and Nuclear Data Tables*, 54(2), 181–342, 1993. doi:10.1006/adnd.1993.1013. page 16.
- [81] THORSTEN HOHAGE, KLAUS GIEWEKEMEYER & TIM SALDITT. *Iterative reconstruction of a refractive-index profile from X-ray or neutron reflectivity measurements*. *Physical Review E*, 77(5), 051604, 2008. doi:10.1103/PhysRevE.77.051604. page 16.
- [82] ANDREW NELSON. *Co-refinement of multiple-contrast neutron/X-ray reflectivity data using motifit*. *Journal of Applied Crystallography*, 39(2), 273–276, 2006. doi:10.1107/S0021889806005073. pages 16 and 98.
- [83] PAUL DRUDE. *Ueber Oberflächenschichten*. *Nachrichten von der Königlichen Gesellschaft der Wissenschaften und der Georg-August-Universität zu Göttingen*, (11), 275–322, 1888. page 17.
- [84] M. HARKE, R. TEPPNER, O. SCHULZ, HUBERT MOTSCHMANN & HORST ORENDI. *Description of a single modular optical setup for ellipsometry, surface plasmons, waveguide modes, and their corresponding imaging techniques including brewster angle microscopy*. *Review of Scientific Instruments*, 68(8), 3130–3134, 1997. doi:10.1063/1.1148256. page 17.
- [85] R. CLARK JONES. *A new calculus for the treatment of optical systems*. *Journal of the Optical Society of America*, 31(7), 488–493, 1941. doi:10.1364/JOSA.31.000488. page 18.
- [86] KLAUS R. NEUMAIER, GUNTER ELENDRER, ERICH SACKMANN & RUDOLF MERKEL. *Ellipsometric microscopy*. *EPL (Europhysics Letters)*, 49(1), 14–19, 2000. doi:10.1209/epl/i2000-00113-x. page 20.
- [87] FELIX LINKE & RUDOLF MERKEL. *Ellipsometric microscopy: Developments towards biophysics*. *IEE Proceedings - Nanobiotechnology*, 151(3), 95–100, 2004. doi:10.1049/ip-nbt:20040777. page 20.
- [88] HANS ARWIN, STEFAN WELIN-KLINTSTRÖM & ROGER JANSSON. *Off-null ellipsometry revisited: Basic considerations for measuring surface concentrations at solid/liquid interfaces*. *Journal of Colloid and Interface Science*, 156, 377–382, 1993. doi:10.1006/jcis.1993.1125. page 20.
- [89] ANGELIKA WURLITZER, E. POLITSCH, STEFAN R. HUEBNER, P. KRÜGER, MARKUS J. WEYGAND, KRISTIAN KJAER, P. HOMMES, OSKAR NUYKEN, GREGOR CEVC & MATHIAS LÖSCHE.

- Conformation of polymer brushes at aqueous surfaces determined with X-ray and neutron reflectometry. 2. High-density phase transition of lipopolyoxazolines. Macromolecules*, 34(5), 1334–1342, 2001. doi:10.1021/ma000932n. pages 24, 26, and 43.
- [90] KARIN LÜDTKE, RAINER JORDAN, NATHAN FURR, SUMIT GARG, KELSEY FORSYTHE & CHRISTOPH A. NAUMANN. *Two-dimensional center-of-mass diffusion of lipid-tethered poly(2-methyl-2-oxazoline) at the air-water interface studied at the single molecule level. Langmuir*, 24(10), 5580–5584, 2008. doi:10.1021/la8001493. pages 24, 26, and 68.
- [91] JANICE M. SMABY, JEAN M. MUDERHWA & HOWARD L. BROCKMAN. *Is lateral phase separation required for fatty acid to stimulate lipases in a phosphatidylcholine interface? Biochemistry*, 33(7), 1915–1922, 1994. doi:10.1021/bio0173a039. page 25.
- [92] DEREK MARSH. *CRC handbook of lipid bilayers*. CRC Press, Baton Roca, Florida, 1990. ISBN 978-0-8493-3255-5. page 25.
- [93] EDWARD D. PALIK, editor. *Handbook of optical constants of solids*. Academic Press, New York, 1. pr edition, 1985. page 26.
- [94] DANIEL DUCHARME, JEAN-JOSEPH MAX, CHRISTIAN SALESSE & ROGER M. LEBLANC. *Ellipsometric study of the physical states of phosphatidylcholines at the air-water interface. Journal of Physical Chemistry*, 94(5), 1925–1932, 1990. doi:10.1021/j100368a038. page 26.
- [95] JOHN ALFRED JOHNSON & NICHOLAS M. BASHARA. *Multiple-angle-of-incidence ellipsometry of very thin films. Journal of the Optical Society of America*, 61(4), 457–462, 1971. doi:10.1364/JOSA.61.000457. pages 27 and 29.
- [96] FLORIAN REHFELDT, MOTOMU TANAKA, LORENA PAGNONI & RAINER JORDAN. *Static and dynamic swelling of grafted poly(2-alkyl-2-oxazoline)s. Langmuir*, 18(12), 4908–4914, 2002. doi:10.1021/la0112559. pages 27 and 29.
- [97] THOMAS J. MCINTOSH & SIDNEY A. SIMON. *Short-range pressures between liquid bilayer membranes. Colloids and Surfaces A: Physicochemical and Engineering Aspects*, 116(3), 251–268, 1996. doi:10.1016/0927-7757(96)03569-8. pages 27 and 44.
- [98] LEWIS GREENSPAN. *Humidity fixed points of binary saturated aqueous solutions. Journal of Research of the National Bureau of Standards – A. Physics and Chemistry*, 81A(1), 89–96, 1977. page 30.
- [99] FLORIAN C. GAERTNER, ROBERT LUXENHOFER, BIRGIT BLECHERT, RAINER JORDAN & MARKUS ESSLER. *Synthesis, biodistribution and excretion of radiolabeled poly(2-alkyl-2-oxazoline)s. Journal of Controlled Release*, 119(3), 291–300, 2007. doi:10.1016/j.jconrel.2007.02.015. page 43.
- [100] STEPHAN HUBER, NAIMA HUTTER & RAINER JORDAN. *Effect of end group polarity upon the lower critical solution temperature of poly(2-isopropyl-2-oxazoline). Colloid and Polymer Science*, 286(14), 1653–1661, 2008. doi:10.1007/s00396-008-1942-7. pages 43 and 48.
- [101] JACOB N. ISRAELACHVILI. *Intermolecular & Surface Forces*. Academic Press, San Diego, 2nd edition, 1991. ISBN 0-12-375181-0. page 44.
- [102] SERGEY LEIKIN, V. ADRIAN PARSESIAN, DONALD C. RAU & R. PETER RAND. *Hydration forces. Annual Review of Physical Chemistry*, 44, 369–395, 1993. doi:10.1146/annurev.pc.44.100193.002101. page 44.

- [103] MICHAEL BACHMANN, HAGEN KLEINERT & AXEL PELSTER. *Fluctuation pressure of a stack of membranes*. *Physical Review E*, 63(5), 051709, 2001. doi:10.1103/PhysRevE.63.051709. page 45.
- [104] JIANBEN SONG & RICHARD E. WAUGH. *Bending rigidity of SOPC membranes containing cholesterol*. *Biophysical Journal*, 64(6), 1967–1970, 1993. doi:10.1016/S0006-3495(93)81566-2. page 45.
- [105] MICHAEL L. CONNOLLY. *Analytical molecular surface calculation*. *Journal of Applied Crystallography*, 16(5), 548–558, 1983. doi:10.1107/S0021889883010985. page 47.
- [106] EUN SEOK GIL & SAMUEL M. HUDSON. *Stimuli-responsive polymers and their bioconjugates*. *Progress in Polymer Science*, 29(12), 1173–1222, 2004. doi:10.1016/j.progpolymsci.2004.08.003. page 48.
- [107] NAOYUKI ISHIDA & MIKIO KOBAYASHI. *Interaction forces measured between poly(*N*-isopropylacrylamide) grafted surface and hydrophobic particle*. *Journal of Colloid and Interface Science*, 297(2), 513–519, 2006. doi:10.1016/j.jcis.2005.10.068. page 51.
- [108] MARTIN KÜHNER & ERICH SACKMANN. *Ultrathin hydrated dextran films grafted on glass: Preparation and characterization of structural, viscous, and elastic properties by quantitative microinterferometry*. *Langmuir*, 12(20), 4866–4876, 1996. doi:10.1021/la960282+. page 51.
- [109] JOHN BARTLETT SEGUR & HELEN E. OBERSTAR. *Viscosity of glycerol and its aqueous solutions*. *Industrial & Engineering Chemistry*, 43(9), 2117–2120, 1951. doi:10.1021/ie50501a040. pages 56 and 58.
- [110] REINER PETERS & KONRAD BECK. *Translational diffusion in phospholipid monolayers measured by fluorescence microphotolysis*. *Proceedings of the National Academy of Sciences of the United States of America*, 80(23), 7183–7, 1983. doi:10.1073/pnas.80.23.7183. PMID: 6580635. page 68.
- [111] MARK SACCHETTI, HYUK YU & GEORGE ZOGRAFI. *Hydrodynamic coupling of monolayers with subphase*. *Journal of Chemical Physics*, 99(1), 563 – 566, 1993. doi:10.1063/1.465781. pages 68 and 70.
- [112] YOUNG SOO KANG & MARCIN MAJDA. *Headgroup immersion depth and its effect on the lateral diffusion of amphiphiles at the air/water interface*. *Journal of Physical Chemistry B*, 104(9), 2082 – 2089, 2000. doi:10.1021/jp993566m. pages 68 and 69.
- [113] PHILIP G. SAFFMAN & MAX DELBRÜCK. *Brownian motion in biological membranes*. *Proceedings of the National Academy of Sciences of the United States of America*, 72(8), 3111–3113, 1975. doi:10.1073/pnas.72.8.3111. page 68.
- [114] MOTOMU TANAKA, JOACHIM HERMANN, ILKA HAASE, MARKUS FISCHER & STEVEN G. BOXER. *Frictional drag and electrical manipulation of recombinant proteins in polymer-supported membranes*. *Langmuir*, 23(10), 5638–5644, 2007. doi:10.1021/la0628219. page 68.
- [115] LEV DAVIDOVICH LANDAU & EVGENY MIKHAILOVICH LIFSHITZ. *Dragging of a liquid by a moving plate*. *Acta Physicochimica U.R.S.S.*, 17(1–2), 42–54, 1942. pages 70 and 80.
- [116] SIMON D. R. WILSON. *The drag-out problem in film coating theory*. *Journal of Engineering Mathematics*, 16(3), 209–221, 1982. doi:10.1007/BF00042717. page 70.

- [117] C. JEFFREY BRINKER. *Sol-Gel Science: The Physics and Chemistry of Sol-Gel Processing: The Physics and Chemistry of Sol-gel Processing*. Academic Press Inc., 1990. ISBN 0121349705. page 70.
- [118] CLAUDE GODRÈCHE & PAUL MANNEVILLE. *Hydrodynamics and Nonlinear Instabilities*. Cambridge University Press, illustrated edition, 1998. ISBN 978-0521455039. page 70.
- [119] JIAXING HUANG, FRANKLIN KIM, ANDREA R. TAO, STEPHEN CONNOR & PEIDONG YANG. *Spontaneous formation of nanoparticle stripe patterns through dewetting*. *Nature Materials*, 4(12), 896–900, 2005. doi:10.1038/nmat1517. page 70.
- [120] GILES DELON, MARC FERMIGIER, JACCO H. SNOEIJER & BRUNO ANDREOTTI. *Relaxation of a dewetting contact line. part 2. Experiments*. *Journal of Fluid Mechanics*, 604, 55–75, 2008. doi:10.1017/S0022112008000979. page 70.
- [121] ROUSLAN KRECHETNIKOV & GEORGE M. HOMSY. *Surfactant effects in the Landau-Levich problem*. *Journal of Fluid Mechanics*, 559, 429–450, 2006. doi:10.1017/S0022112006000425. page 70.
- [122] PIERRE-GILLES DE GENNES. *Deposition of Langmuir-Blodgett layers*. *Colloid & Polymer Science*, 264, 463 – 465, 1986. doi:10.1007/BF01419552. pages 70 and 80.
- [123] JAVIER FUENTES & RAMON L. CERRO. *Flow patterns and interfacial velocities near a moving contact line*. *Experiments in Fluids*, 38, 503–510, 2005. doi:10.1007/s00348-005-0941-4. page 71.
- [124] SHAILESH NAIRE, RICHARD J. BRAUN & STEVE A. SNOW. *An insoluble surfactant model for a vertical draining free film*. *Journal of Colloid and Interface Science*, 230(1), 91–106, 2000. doi:10.1006/jcis.2000.7081. page 71.
- [125] SHAILESH NAIRE, RICHARD J. BRAUN & STEVE A. SNOW. *An insoluble surfactant model for a vertical draining free film with variable surface viscosity*. *Physics of Fluids*, 13(9), 2492–2502, 2001. doi:10.1063/1.1388540. page 71.
- [126] JONATHAN E. GUYER, DANIEL WHEELER & JAMES A. WARREN. *FiPy: Partial differential equations with python*. *Computing in Science and Engineering*, 11(3), 6–15, 2009. doi:10.1109/MCSE.2009.52. page 72.
- [127] HENK KAARLE VERSTEEG & WEERATUNGE MALALASEKERA. *An Introduction to Computational Fluid Dynamics: The Finite Volume Method Approach*. Longman Scientific and Technical, 1995. ISBN 978-0582218840. page 73.
- [128] SUHAS V. PATANKAR. *Numerical Heat Transfer and Fluid Flow*. Taylor and Francis, 1980. ISBN 978-0891165224. page 73.
- [129] ILYA MIKHAILOVICH LIFSHITZ & V. V. SLYOZOV. *The kinetics of precipitation from super-saturated solid solutions*. *Journal of Physics and Chemistry of Solids*, 19(1-2), 35–50, 1961. doi:10.1016/0022-3697(61)90054-3. pages 75 and 80.
- [130] HARALD GARCKE, BARBARA NIETHAMMER, MARTIN RUMPF & ULRICH WEIKARD. *Transient coarsening behaviour in the Cahn–Hilliard model*. *Acta Materialia*, 51(10), 2823–2830, 2003. doi:10.1016/S1359-6454(03)00087-9. page 75.
- [131] LEV DAVIDOVICH LANDAU & EVGENY MIKHAILOVICH LIFSHITZ. *Fluid Mechanics*, vol-

- ume 6 of *Course of Theoretical Physics*. Butterworth Heinemann, 2nd edition, 1987. ISBN 978-0750627672. page 79.
- [132] RAMON L. CERRO. *Moving contact lines and Langmuir–Blodgett film deposition*. *Journal of Colloid and Interface Science*, 257, 276–283, 2003. doi:10.1016/S0021-9797(02)00009-7. page 79.
- [133] JOHN W. CAHN & JOHN E. HILLIARD. *Free energy of a nonuniform system. I. Interfacial free energy*. *The Journal of Chemical Physics*, 28(2), 258–267, 1958. doi:10.1063/1.1744102. pages 80 and 102.
- [134] MICHAEL BESTEHORN. *Hydrodynamik und Strukturbildung*. Springer-Lehrbuch. Springer Berlin Heidelberg, 2006. ISBN 978-3-540-33796-6. doi:10.1007/3-540-33797-0. page 80.
- [135] ALAN J. BRAY. *Theory of phase-ordering kinetics*. *Advances in Physics*, 51(2), 481–587, 2002. doi:10.1080/00018730110117433. page 80.
- [136] HIROYUKI TAKENO & TAKEJI HASHIMOTO. *Crossover of domain-growth behavior from percolation to cluster regime in phase separation of an off-critical polymer mixture*. *Journal of Chemical Physics*, 107(5), 1634–1644, 1997. doi:10.1063/1.474515. page 80.
- [137] MICHAEL F. BUTLER & MARY HEPPENSTALL-BUTLER. *Phase separation in gelatin/maltodextrin and gelatin/maltodextrin/gum arabic mixtures studied using small-angle light scattering, turbidity, and microscopy*. *Biomacromolecules*, 2(3), 812–823, 2001. doi:10.1021/bm015503r. page 80.
- [138] JOÃO T. CABRAL, JULIA S. HIGGINS, NATALYA A. YERINA & SERGEI N. MAGONOV. *Topography of phase-separated critical and off-critical polymer mixtures*. *Macromolecules*, 35(5), 1941–1950, 2002. doi:10.1021/ma0114990. page 80.
- [139] PETER F. GREEN. *Wetting and dynamics of structured liquid films*. *Journal of Polymer Science Part B: Polymer Physics*, 41(19), 2219–2235, 2003. doi:10.1002/polb.10601. page 80.
- [140] HYUN-JOONG CHUNG & RUSSELL J. COMPOSTO. *Breakdown of dynamic scaling in thin film binary liquids undergoing phase separation*. *Physical Review Letters*, 92(18), 185704, 2004. doi:10.1103/PhysRevLett.92.185704. page 80.
- [141] D. M. LENEVEU, R. PETER RAND & V. ADRIAN PARSEGAN. *Measurement of forces between lecithin bilayers*. *Nature*, 259(5544), 601–603, 1976. doi:10.1038/259601a0. page 84.
- [142] MARIA TOMOAIÁ-COTISEL, EMIL CHIFU, JANOS ZSAKO, AURORA MOCANU, PETER J. QUINN & MORRIS KATES. *Monolayer properties of archaeol and caldarchaeol polar lipids of a methanogenic archaeobacterium, methanospirillum hungatei, at the air/water interface*. *Chemistry and Physics of Lipids*, 63(1-2), 131–138, 1992. doi:10.1016/0009-3084(92)90029-O. page 84.
- [143] ALEXANDER ROHRBACH, CHRISTIAN TISCHER, DIRK NEUMAYER, ERNST-LUDWIG FLORIN & ERNST H. K. STELZER. *Trapping and tracking a local probe with a photonic force microscope*. *Review of Scientific Instruments*, 75(6), 2197–2210, 2004. doi:10.1063/1.1753097. page 87.
- [144] TAKEJI HASHIMOTO, KATSUO MATSUZAKA, ELISHA MOSES & AKIRA ONUKI. *String phase in phase-separating fluids under shear flow*. *Physical Review Letters*, 74(1), 126–129, 1995. doi:10.1103/PhysRevLett.74.126. page 87.

- [145] ARMIN LAMBACHER & PETER FROMHERZ. *Fluorescence interference-contrast microscopy on oxidized silicon using a monomolecular dye layer*. *Applied Physics A*, 63, 207–216, 1996. doi:10.1007/BF01567871. page 100.
- [146] KAMIL GODULA, MARISSA L. UMBEL, DAVID RABUKA, ZSOFIA BOTYANSZKI, CAROLYN R. BERTOZZI & RAGHUVeer PARTHASARATHY. *Control of the molecular orientation of membrane-anchored biomimetic glycopolymers*. *Journal of the American Chemical Society*, 131(29), 10263–10268, 2009. doi:10.1021/ja903114g. page 100.
- [147] DANIEL AXELROD. *Carbocyanine dye orientation in red cell membrane studied by microscopic fluorescence polarization*. *Biophysical Journal*, 26(3), 557–573, 1979. doi:10.1016/S0006-3495(79)85271-6. page 100.
- [148] CHRISTOF ECK, HARALD GARCKE & PETER KNABNER. *Mathematische Modellierung*. Springer-Lehrbuch. Springer Berlin Heidelberg, 2008. doi:10.1007/978-3-540-74968-4. page 101.
- [149] RICHARD ANTHONY & LEWIS JONES. *Soft Condensed Matter*. Oxford University Press, illustrated, reprint edition, 2002. ISBN 978-0198505891. page 101.